Optimized Planning for a Multiple Space Debris Removal Mission

Author: Mikkel Kranker Jørgensen
Supervisor: Prof. Inna Sharf

Doctoral Thesis

Department of Mechanical Engineering
McGill University
Montréal, Québec, Canada

December 2020

A thesis submitted to McGill University in partial
fulfillment of the requirements for the degree of
Doctor of Philosophy in Mechanical Engineering

Abstract

Lower Earth orbits (LEO) have become the residence for a significant number of large space debris, most of which are defunct satellites and rocket upper stages. The said debris jeopardize regular spacecraft operations in LEO and act as sources of smaller debris as a result of collisions and degradation. To mitigate the adverse effects of space debris and to remediate the LEO region, active debris removal (ADR) missions have been proposed. In this thesis, a mission plan for de-orbiting multiple pieces of large space debris is formulated and evaluated. Within this mission plan, low thrust orbital manoeuvres are used to achieve the necessary orbital transfers by considering the trade-offs between fuel mass and mission time. For the proposed mission scenario, the debris re-enters Earth's atmosphere in an uncontrolled fashion and as such, strategies for minimizing casualty risk as a result of debris re-entry are proposed.

In the first part of the thesis, two approaches for multiple debris removal are considered: recursive and mothership. The latter involves the chaser travelling directly from debris to debris and is used for benchmarking the primary (recursive) mission scenario. The recursive scenario requires the chaser to capture and de-orbit the debris to a disposal orbit, after which it releases the first piece of debris and performs a rendezvous with the next debris, continuing until the end of the mission in a recursive fashion. Within each rendezvous phase, the orbital drift of both the chaser and the target are considered. To reduce the fuel cost of accurate rendezvous with multiple pieces of space debris, optimized drift orbits for chaser transfers with large changes in right ascension of the ascending node (RAAN) are introduced. Each orbital manoeuvre considered is defined as a minimum-time orbital

transfer, using low-thrust propulsion. The main contribution in the first part of the thesis is the formulation and solution for an accurate motion plan to execute the recursive strategy, by using the point-to-point transfers. The point-to-point transfer is posed as a constrained non-linear optimal control problem, implemented in GPOPS-II – a MATLAB software. As the chaser makes numerous revolutions around Earth until it reaches the debris target, we present a methodology for generating an accurate initial guess needed to find the optimal solution. The process of solving this problem for each rendezvous is iterated until the post-propagation (over the time of transfer) location of the debris matches the location of the chaser, following the high-accuracy transfer. To demonstrate the capabilities of the formulation and the feasibility of the solutions, several sets of debris are introduced with different features, in particular, a set of five pieces of debris with small inclination differences, a set of two debris with a large inclination difference, and a set of five debris with large RAAN differences. The outcomes are the transfer characteristics for the chaser to achieve the best possible trade-off between time and fuel for the multiple debris removal mission and the control input time histories required to achieve it.

The second contribution of this thesis involves the analysis of the debris re-entry stage of the ADR mission vis a vis the parameters of the disposal orbit. More specifically, the de-orbiting part of an ADR mission, can be designed such that the parameters of the disposal orbit minimize the casualty risk of large debris re-entry. To analyse re-entry, the Debris Risk Assessment and Mitigation Analysis (DRAMA) software suite, developed by the European Space Agency, is the primary model employed. With respect to release conditions, once the debris is in the disposal orbit, the effect of introducing a small-magnitude impulse onto the debris at the release is studied, consequently showing that the casualty risk factor can be lowered. It has previously been demonstrated that the orientation and surface area of the debris at the onset of re-entry have a significant impact on the characteristics of the re-entry. To this end, a high fidelity coupled orbital-attitude propagator is used to analyze the rotational state evolution of the debris between its release in the disposal orbit (at 200 km) and the onset of re-entry (assumed at 125 km altitude). The debris is released with various orientations, and the effects of the attitude state on the re-entry analysis are investigated. As a real-life application, the first Chinese space station, Tiangong-1, is used to analyze the influence of orientation on re-entry predictions, such as time and location of impact.

Résumé

Les orbites terrestres basses (OTB) sont devenues la résidence d'un nombre important de gros débris spatiaux, dont la plupart sont des satellites et des étages supérieurs de fusées. Lesdits débris mettent en péril les opérations régulières des engins spatiaux en OTB et agissent comme des sources de débris plus petits en raison de collisions et de dégradation. Pour atténuer les effets néfastes des débris spatiaux et pour remédier à la région OTB, des missions d'élimination active des débris (ADR) ont été proposées. Dans cette thèse, un plan de mission pour la désorbitation de plusieurs morceaux de gros débris spatiaux est formulé et évalué. Dans le cadre de ce plan de mission, des manœuvres orbitales à faibles poussées sont utilisées pour réaliser les transferts orbitaux nécessaires en tenant compte des compromis entre la masse de carburant et le temps de mission. Pour le scénario de mission proposé, les débris rentrent dans l'atmosphère de la Terre de manière incontrôlée et, à ce titre, des stratégies visant à minimiser le risque d'accident résultant de la rentrée des débris sont proposées.

Dans la première partie de cette thèse, deux approches pour l'enlèvement de plusieurs débris sont considérées : une approche récursive et une approche de navire-mère. Ce dernier implique le chasseur voyageant directement des débris aux débris et est utilisé comme comparatif pour le scénario de mission principal (récursif). Le scénario récursif nécessite que le chasseur capture et désorbite le débris sur une orbite d'élimination, après quoi il libère le premier morceau de débris et effectue un rendez-vous avec le morceau suivant, et ainsi de suite, jusqu'à la fin de la mission de manière récursive. Dans chaque phase de rendez-vous, la dérive orbitale du chasseur et de la cible est prise en compte. Pour réduire le coût du

carburant du rendez-vous précis avec plusieurs morceaux de débris spatiaux, les orbites de dérive optimisées pour les transferts de chasseur avec des grands changements de la longitude du nœud ascendant de l'orbite (RAAN) sont introduites. Chaque manœuvre orbitale considérée dans cette thèse est définie comme un transfert orbital à durée minimale, utilisant une propulsion à faible poussée. La principale contribution de la première partie de cette thèse est la formulation et la solution d'un plan de mouvement précis pour exécuter la stratégie récursive, en utilisant les transferts point à point. Le transfert point à point est posé comme un problème de contrôle optimal non linéaire à contraintes, implémenté dans GPOPS-II, un logiciel MATLAB. Alors que le chasseur effectue de nombreuses révolutions autour de la Terre jusqu'à ce qu'il atteigne sa cible, nous présentons une méthodologie pour générer une estimation initiale précise nécessaire pour trouver la solution optimale. Le processus de résolution de ce problème pour chaque rendez-vous est itéré jusqu'à ce que l'emplacement post-propagation (au cours du transfert) des débris corresponde à l'emplacement du chasseur, après le transfert de haute précision. Pour démontrer les capacités de la formulation et la faisabilité des solutions, plusieurs ensembles de débris sont introduits avec différentes caractéristiques, notamment un ensemble de cinq morceaux de débris avec de petites différences d'inclinaison, un ensemble de deux morceaux de débris avec une grande différence d'inclinaison, et un ensemble de cinq débris avec de grandes différences de longitude du nœud ascendant. Les résultats sont les caractéristiques de transfert pour que le chasseur atteigne le meilleur compromis possible entre le temps et le carburant pour la mission d'enlèvement de plusieurs débris et les historiques de temps d'entrée de contrôle nécessaires pour y parvenir.

La deuxième contribution de cette thèse concerne l'analyse de l'étape de rentrée des débris de la mission ADR vis-à-vis des paramètres de l'orbite d'élimination. Plus concrètement, la partie de désorbitation d'une mission ADR peut être conçue de telle sorte que les paramètres de l'orbite d'élimination minimisent le risque d'accident de la rentrée de gros débris. Pour analyser la rentré, la suite logicielle DRAMA (Debris Risk Assessment and Mitigation Analysis), développé par l'Agence spatiale européenne, est le principal modèle utilisé. En ce qui concerne les conditions de libération une fois que les débris sont sur l'orbite d'élimination, l'effet de l'introduction d'une impulsion de faible magnitude sur les débris au moment du rejet est étudié, montrant par conséquent que le facteur de

risque d'accident peut être abaissé. Il a été précédemment démontré que l'orientation et la superficie du morceau de débris au début de la rentrée ont un impact significatif sur les caractéristiques de la rentrée. A cet effet, un propagateur d'attitude orbitale couplé haute-fidélité est utilisé pour analyser l'évolution de l'état de rotation du débris entre sa libération dans l'orbite d'élimination (à 200 km) et le début de la rentrée (supposée être à 125 km d'altitude). Les débris sont libérés avec différentes orientations, et les effets de l'état d'attitude pendant la descente sur l'analyse de rentrée sont examinés. Comme application dans la vie réelle, la première station spatiale chinoise, Tiangong-1, est utilisée pour analyser l'influence de l'orientation sur les prédictions de rentrée, telles que l'heure et le lieu de l'impact.

Acknowledgements

The journey that is my doctoral studies at McGill University has been enlightening in a multitude of ways, and for that I have several people to thank. Each person mentioned here has contributed to an unforgettable and enriching experience that will stay with me forever.

Above all, I would like to show my appreciation for the support, mentorship, and guidance provided by Professor Inna Sharf throughout my studies and thank her for the opportunity she has given me to explore the field of space debris and pursue the research paths that I found most captivating. Not only has she challenged me to become a better critical thinker and academic writer, she has also provided ample amounts of her time to assist me during my research.

For their time and expertise, I would like to acknowledge my Ph.D. Supervisory Committee in addition to my internal and external examiners. I would also like to thank the anonymous article reviewers for their feedback that helped significantly improve the content of this work.

I would also like to thank my former supervisor, Laryssa Patten, for introducing me to the aerospace domain and the impact of satellites have on all our lives. Laryssa has always been happy to answer any of my space-related questions and provide insightful sources for information, for which I am very grateful.

It goes without saying that my research journey would not have been the same without all the amazing people in the Aerospace Mechatronics Lab. I would like to thank Eleonora and Luc for helping me out whenever I had any space debris-related questions and for their

Claims of Originality

The main contributions of this thesis to the field of aerospace engineering are as follows:

- Development of an optimal control formulation for a multi-debris removal mission employing a recursive strategy. The formulation allows to generate a comprehensive mission plan and has the following unique features:

  - The optimal control problem is solved to minimize the fuel and time cost of point-to-point rendezvous and de-orbiting of multiple pieces of space debris.

  - The formulation considers the true anomaly as a boundary condition for accurate point-to-point transfer.

  - Included within the formulation, is an approach to generate an initial guess, required to solve the orbital transfer problem for each debris, based on attributing different weights to those orbital parameters that are more costly to match for a specific piece of debris.

  - There is an iterative element addressing the fact that the long time taken for low-thrust transfers results in the debris location changing significantly between the transfer initiation and the arrival of the chaser in the desired orbit.

  - Drift orbits to match the RAAN of the chaser to that of the debris at the cost of time, as opposed to fuel, are introduced as part of this formulation.

- Analysis of multiple sets of debris for the planning of various types of multiple debris removal missions:

- This provides insights into the feasibility of recursive vs. mothership mission approaches.

- The analysis results in estimates for the fuel and time costs for multiple debris removal missions.

- It allows to compare approaches to multiple active debris removal missions and defining optimised solutions for debris with varying physical and orbital parameters.

- Definition and exploration of the notion of partially controlled re-entry for multiple debris removal missions.

  - This includes analysing the effect of disposal orbit parameters on uncontrolled re-entry for large space debris.

  - The design space for introducing a small impulse when releasing debris during a multiple debris removal mission is defined.

  - The effects of debris orientation on the re-entry risk as well as time and location of re-entry of large space debris as the debris re-enters Earth's atmosphere are identified and presented.

Outside of the code included as part of the software tools used in this thesis (see Section 2.3, all code for the purpose of analysis and problem formulation was written by Mikkel Jørgensen. Edelbaum's equations as well as the formulation for Lambert's theorem included in Chapter 3 are taken from [1] and [2] respectively and are used as part of the formulations presented in this thesis. The differential equations of motion presented in Section 2.2 are taken from [3]. The basis for defining a minimum-time optimal control problem for orbital transfers was included as part of the GPOPS-II software package [4] and has been used as premise for the optimal control formulation developed as part of this thesis. The long term propagation of Tiangong-1 presented in Section 5.4.4 was carried out by Luc Sagnières. This thesis was compiled in LaTeX using TEXMAKER. The work presented, particularly the analysis of simulations, was the result of numerous discussions between Mikkel Jørgensen and Inna Sharf. The final manuscript is revised in response

to suggestions and comments from Inna Sharf and multiple anonymous article reviewers. The abstract presented as part of this work has been translated into French by Elisabeth O'Regan. Inna Sharf has provided mentorship and guidance throughout the entire process of developing the work presented in this thesis.

Parts of this thesis have previously appeared in the following journal articles and conference papers:

- M. Jorgensen and I. Sharf, "Planning and optimization for a multiple space debris removal mission," 2018 IEEE Aerospace Conference, Big Sky, MT, 2018, pp. 1-10.

- M. Jorgensen and I. Sharf, "Optimal Drift Orbit Planning for a Multiple Space Debris Removal Mission using High-Accuracy Low-Thrust Transfers," 1st International Orbital Debris Conference, Sugar Land, TX, 2019.

- M. Jorgensen and I. Sharf, "Optimal planning for a multiple space debris removal mission using high-accuracy low-thrust transfers," *Acta Astronautica*, vol. 172, Jul., pp. 56-69, 2020.

- M. Jorgensen and I. Sharf, "Risk Assessment for Uncontrolled Re-entry of Large Space Debris," accepted in *Advances in Space Research*, Mar. 2021.

- L. Sagniéres, M. Jorgensen and I. Sharf, "Simulating the Rotational Dynamics of Tiangong-1 for Re-entry Analysis," accepted for the 8th European Conference on Space Debris, ESA, Apr. 2021.

Contents

List of Figures

List of Tables

Abbreviations

ADR	Active Debris Removal
ASAT	Anti-Satellite Weapon
CFRP	Carbon Fibre Reinforced Polymer
D-SPOSE	Debris SPin/Orbit Simulation Environment
DAS	Debris Assessment Software
DRAMA	Debris Risk Assessment and Mitigation Analysis
ECI	Earth-Centered Inertial
ECO	Earth-Centered Orbital
EDT	Electro-Dynamic Tether
EGM	Earth Gravitational Model
EO	Earth Observation
ESA	European Space Agency
GEO	Geostationary Orbit
GLONASS	Globalnaya Navigazionnaya Sputnikovaya Sistema
GNSS	Global Navigation Satellite System
GPS	Global Positioning System
IADC	Inter-Agency Space Debris Co-ordination Committee
IBS	Ion-Beam Shepherd
IPOPT	Interior Point OPTimizer
ISO	International Organization for Standardization
ISS	International Space Station
LARES	Laser Relativity Satellite

LAGEOS-2	Laser Geodynamics Satellite 2
LEO	Lower Earth Orbit
LGR	Legendre-Gauss-Radau
MASTER	Meteoroid and Space Debris Terrestrial Environment Reference
MEO	Medium-Earth Orbit
NASA	National Aeronautics and Space Administration
NLP	Non-Linear Programming
NORAD	North American Aerospace Defense Command
OOS	On-Orbit Servicing
PNT	Position, Navigation, and Timing
RAAN	Right Ascension of the Ascending Node
SARA	Survival and Risk Analysis
SCO	Satellite-Centered Orbital
SERAM	Spacecraft Entry Risk Analysis Module
SESAM	Spacecraft Entry Survival Analysis Module
SSA	Space Situational Awareness
TEME	True Equator Mean Equinox
TLE	Two-Line Element
TSS	Tethered Space System
UN	United Nations
UNCOPUOS	United Nations Committee on the Peaceful Uses of Outer Space
UNGA	United Nations General Assembly
UN GPW	United Nations Gridded Population of the World
UNWPP	United Nations World Population Prospects
USSTRATCOM	United States Strategic Command
UV	Ultra Violet

Physical Constants

Earth Equatorial Radius	$R_e = 6378.1363$ km
Earth Mean Reference Spherical Radius	$a_M = 6371.2$ km
Earth Gravitational Parameter	$\mu_e = 3986004.418 \times 10^8$ m^3 s^{-1}
Earth Oblateness Coefficients:	$J_2 = 1082.639 \times 10^{-6}$
	$J_3 = -2.565 \times 10^{-6}$
	$J_4 = -1.608 \times 10^{-6}$

Symbols

A_c	casualty area	m^2
A_h	vertical projected area of standing human	m^2
A_i	impact cross-section	m^2
a	semi-major axis	m
C	relating to chaser	
C_D	drag coefficient	
D	relating to debris	
Do	relating to de-orbit	
E	eccentric anomaly	
e	eccentricity	
f	equinoctial element related to eccentricity	
$f()$	function	
g	equinoctial element related to eccentricity	
g_i	vector field i	
$g_i()$	constraint i	
H	angular momentum	$kg \cdot m^2 \cdot s^{-1}$
H_L	hypergeometric function	
h	equinoctial element related to inclination	
I_{sp}	specific impulse	s
i	inclination	rad
i_n	north direction	
J	objective function	
k	equinoctial element related to inclination	

L	true longitude	rad
M	current mass	kg
M_0	mass at ignition	kg
M_d	dry mass	kg
M_E	power supply mass	kg
M_P	propellant mass	kg
M_S	structure mass	kg
m	chaser mass	kg
$\dot{m}_e$	mass flow rate	$kg \cdot s^{-1}$
$\mathcal{O}$	open set	
P	propagation	
P_c	risk factor	
P_E	electric power	W
P_i	impact probability	
p	semi-latus rectum	m
$\mathbb{R}$	set of real numbers	
R	relating to rendezvouos	
r	position	m
$\mathbf{r}$	position vector	m
$\mathbb{S}^n$	n-sphere	
S	aerodynamic reference area	m^2
T	thrust	N
t	time	s
$\mathbf{u}$	thrust direction vector	
v	velocity	$m \cdot s^{-1}$
$\mathbf{v}$	velocity vector	$m \cdot s^{-1}$
v_e	exhaust velocity	$m \cdot s^{-1}$
$\mathbf{Q}_r$	rotation matrix from rotating radial to Earth-centered inertial coordinates	
$\mathbf{w}$	weights	

α	state vector	
$\dot{\alpha}$	dynamics vector	
χ	heading angle	rad
Δ	represents a change	
$\boldsymbol{\Delta}$	chaser acceleration	$m \cdot s^{-2}$
$\boldsymbol{\Delta}_D$	drag acceleration	$m \cdot s^{-2}$
$\boldsymbol{\Delta}_g$	gravitational acceleration	$m \cdot s^{-2}$
$\boldsymbol{\Delta}_T$	thrust acceleration	$m \cdot s^{-2}$
ΔV	velocity change for orbital transfer	$m \cdot s^{-1}$
δg_n	Earth oblateness perturbation north direction	$m \cdot s^{-2}$
δg_r	Earth oblateness perturbation radial direction	$m \cdot s^{-2}$
ξ	the angle between the position vector of the	
	chaser and that of the debris relative to the focus	rad
γ	flight path angle	rad
η	power to mass ratio	$W \cdot kg^{-1}$
Λ	set of Lie brackets	
λ	mean longitude	rad
λ_{ra}	right ascension	rad
ν	thruster efficiency	
ρ	atmospheric density	$kg \cdot m^{-3}$
ρ_p	average population density	m^{-2}
Ω	right ascension of the ascending node	rad
ω	argument of perigee	rad
ϕ	spherical geocentric latitude	rad
τ	thrust acceleration	$m \cdot s^{-2}$
θ	true anomaly	rad
θ_{dec}	declination	rad

$\Delta_r, \Delta_\theta, \Delta_h$	chaser acceleration components in rotating radial frame
$\mathbf{i}_r, \mathbf{i}_\theta, \mathbf{i}_h$	Rotating Radial frame axes
u_r, u_θ, u_h	thrust direction components in rotating radial frame
$\mathbf{X}, \mathbf{Y}, \mathbf{Z}$	Earth-Centered Inertial frame axes
$\mathbf{x}_0, \mathbf{y}_0, \mathbf{z}_0$	Earth-Centered Orbital frame axes
$\mathbf{x}, \mathbf{y}, \mathbf{z}$	Body-Frame axes

1

Introduction

1.1 Background and Motivation

Unbeknownst to most, spacecraft primarily in the form of near-Earth satellites contribute to many key aspects of modern society. The vast majority of satellite purposes fall into one of the following categories: Earth observation (EO); position, navigation, and timing (PNT); meteorology; space situational awareness (SSA); communications; missile defence; and space science [6]. EO satellites not only include optical imaging satellites but also other kinds of electromagnetic imaging satellites for purposes such as environmental monitoring, spying, and surveying by taking images analogous to aerial photographs. Global navigation satellite systems (GNSS) fall within the category of PNT satellites, the most prominent of which is the American satellite constellation known as the global positioning system (GPS). Such satellite constellations are used for global satellite navigation and tracking; in addition, these satellites are also used for timing purposes crucial for the global financial industry and stock exchange as well as co-ordinated transactions using common credit cards. While meteorology and weather satellites are primarily used to monitor weather and climate, they are also used for natural disaster prediction and tracking. In order to keep track of various spacecraft orbiting Earth, SSA satellites monitor and track orbiting objects. Some SSA satellites provide space weather forecast and monitoring, as this can impact other satellite functionalities. Another use for SSA satellites is monitoring near-Earth objects such as meteorites and providing warnings in the event that such objects come into collision course with Earth. Satellite television and satellite phones op-

erate by utilizing communications satellites, which is one of the most reliable means of global communication. Missile defence satellites are entirely military owned and provide early warnings in the event that an intercontinental ballistic missile is launched on Earth. Finally, space science satellites contribute to the fields of astronomy and astrophysics, provide platforms for space exploration, and act as test beds for biological responses in a space environment.

Given the vast spectrum of influence possessed by near-Earth satellites, it would be detrimental if these systems were to fail. As such, billions of dollars are invested into research and development of said satellite systems [7] such that the chance of success of every launch and mission objective is as high as possible. In addition, the space environment is heavily monitored by ground- and space-based SSA such that collisions can be avoided [8]. Significant effort is put into satellite safety; however, since near-Earth space provides a tremendous environment for technological advances on top of all the utility previously mentioned, more and more objects are being launched into space [9]. These objects all have a finite lifetime in terms of operational functionality and are therefore left to orbit Earth in the form of space debris as and when their purpose is fulfilled, they run out of fuel, or breakdown. This space debris, defined as objects in near-Earth space that do not have an active purpose and are no longer under active control and/or have lost communication, now pose a collision threat to working satellites systems and thereby the utility and investments they represent.

1.1.1   The Space Debris Scenario

The launching of objects into space in order to take advantage of the data they can gather, and the utility spacecraft provide has progressed at an increasing rate since the launch of Sputnik 1 in 1957 [10]. As a consequence, the orbits around Earth contain a multitude of operational spacecraft such as satellites and the International Space Station (ISS), but also defunct satellites, spent rocket stages and other miscellaneous items related to space missions. Space debris was initially recognized as a problem by Kessler and Cour-Palais [11] in 1978 when they suggested that the growth of objects in space could lead to a chain reaction of collisions, commonly known as the Kessler Syndrome. In this scenario, all utility and functionality of satellites in near-Earth space would cease to exist. To assess whether

1.1 Background and Motivation

the Kessler Syndrome is already reality or some future possibility, is not straightforward. In theory, if satellites in orbit near Earth did not slowly decay towards Earth, only two defunct satellites orbiting forever would result in a collision. Furthermore, the fragments resulting from this collision, remain in orbit forever and collide with each other continuously. Now, with Earth's atmosphere present, satellites decay and re-enter which means collision are not inevitable; however, the object density in near-Earth orbits already suggests that the collision rate producing objects in the future would exceed the natural cleansing rate. This means certain altitude bands might already experience the onset of collisional cascading, but at varying rates. As such Kessler Syndrome is recognised as a real possibility with the growth in space activity and congestion over the last two decades [12], if not already a current concern.

There are multiple sources that contribute to the space debris problem; first, there is mission-related debris which consists of objects generated from deployment operations. Some examples of mission related debris include spent fuel and exhaust particles, satellite and launch vehicle separation residue, rocket bodies from various launch stages, disposed protective shields, and incidental hardware [13]. Of these examples, the largest contributors to the overall mass of debris orbiting Earth is the rocket bodies from various launch stages [12]. The final stage rocket bodies remain in similar orbits to working satellites for decades and can weigh over one tonne [12].

Another source of space debris is accidental debris. This type of debris ranges from objects dropped or lost during manned space operations, to paint chips separated from various spacecraft as a result of weathering by the harsh conditions in space [13]. A more serious source of accidental debris is explosions caused by leftover fuel remaining in liquid-fuel rocket stages. Exposure to solar heat often causes the pressure to increase within these fuel tanks to the point where the propellant tank explodes. Such explosions can also be caused by the large temperature fluctuations, resulting from oscillations of exposure to the sun [14]. Furthermore, a detrimental collision between intact satellites occurred on 10 February 2009, the inactive Russian Cosmos 2251 satellite and the operational American Iridium 33 satellite, predicted to encounter a close approach of 584 m, which impacted at an altitude of 770 km. This event lead to over 2,300 extra tracked fragments in orbit [15, 16]. To this date, this is the most severe collision in terms of debris generation, and the overall

negative impact of the space debris scenario; however, other debris generating collisions happen regularly albeit as a result of large objects being impacted by much smaller ones, only creating additional small pieces of debris [17].

The last major source of space debris is in space weapons testing. Historically, the United States and the Soviet Union conducted numerous tests of anti-satellite weapons (ASATs) in the period between 1968 and 1985 [18]. More recently, and with a much greater impact in terms of space debris generation, the Chinese conducted an ASAT test in 2007 where the Fengyun-1C satellite was blown up, causing the population near- or even in highly populated orbits to increase significantly [13].

The European space agency (ESA) has stated as of February 2020 that among more than 22,300 regularly tracked (larger than 10 cm) objects in near-Earth space, only about 2,300 are functional space systems, which means 90% are space debris [19]. Additionally, using space debris environment models, it has been predicted that over 900,000 objects in the size bracket 1 cm to 10 cm and more than 128 million in the bracket 1 mm to 1 cm exist in the various orbits around Earth [19]. Any of the objects orbiting Earth have the potential to damage operational satellites to various degrees. For example, debris larger than 10 cm can cause catastrophic fragmentation, objects larger than 1 cm can render a satellite defunct or even penetrate the shields of the ISS, and even debris with an order of magnitude of 1 mm can destroy subsystems aboard a spacecraft [20]. Space debris is a real problem, as functional satellites are exposed to an increasing risk of collision with an ever-increasing amount of debris [21, 22]. Given the increase in operational satellites sent into orbit from 39 launches in 2000 to 387 in 2019 [9], in combination with the existing objects orbiting Earth as well as the absence of standardized end-of-life procedures for satellites and other spacecraft until recently [23], it is unlikely that the probability of collision between operational satellites and space debris will remain low if no action is taken.

The orbits that are highly critical are those where most of the operational satellites are situated and these can be narrowed down into three categories: geostationary orbit (GEO 36,000 km altitude), medium-Earth orbit (MEO 20,000 km altitude), and lower-Earth orbit (LEO 200 km - 2,000 km altitude). Due to the much higher spatial density of debris in LEO [24], there is a higher likelihood of collision between objects orbiting in this region, and as such, research has been conducted by various authors to estimate the cost and effectiveness

of debris mitigation [25, 26]. There is a consensus that something needs to be done regarding the debris situation in LEO, and the sooner solutions are implemented, the higher the effectiveness, and the lower the cost incurred.

Moreover, a more specific look is taken at sun-synchronous orbits by Vance and Mense [27] as this is where many high-value satellites, as well as most of the debris, are situated. It is concluded that in order to be cost effective, larger objects should be the focus of debris mitigation and the value of removal of large objects increases with time. Although less critical, MEO and GEO are also cause for concern with respect to space debris. It is argued that, despite being less congested, it is important for debris in GEO to be dealt with as soon as possible, as this requires fewer technical advances and in addition, there are no natural measures of debris decay in GEO such as atmospheric drag [25, 28]. MEO has recently become a cause for concern as well, since all Global Navigation Satellite Systems (GNSS) are situated at this altitude. In addition, there has recently been a rise in the number of GNSS, as Europe (ESA) is nearing the completion of the Galileo programme and China is advancing their GNSS, Beidou. This adds to the already existing systems in MEO from the USA (GPS) and Russia (GLONASS), creating more congestion in MEO given that each GNSS contains around 30 satellites [29, 30]. However, in a recent study, Rossi et al. [29] conclude that there is and will be, for the foreseeable future, a very low spatial density of objects in the MEO region, which makes orbital crossings statistically rare events.

Ultimately, LEO is the most used and therefore most crowded region of near-Earth space. LEO is also the region with the highest collision risk [31] and the highest likelihood of contribution to the overall number of space debris. Furthermore, large debris act as continual sources of smaller pieces of space debris due to regular impacts [32] and are significantly easier to track. In summary, action will have to be taken regarding the current and future near-Earth space environment, and the seemingly most effective place to start is with large debris in LEO.

1.1.2 Responding to the Space Debris Phenomenon

Four responses to dealing with the space debris problem have been proposed by the international community [33]. The first response is to take no action with respect to the space

debris threat, as the cost-benefit analysis suggests that there is yet not enough value in dealing with space debris. This is supported by the research of Wiedemann et al. [33], suggesting that if the state of the space environment as of 2012 was maintained, removing debris would only be worthwhile for a few high priority targets. The second approach to dealing with space debris is to expend some fuel in order to manoeuvre the space system at risk outside of the collision course of the space debris. In fact, collision avoidance manoeuvres can be tied in with routine orbital correction manoeuvres such that minimal fuel is spent [34]. Deciding which satellite to manoeuvre and when to do so involves a high level of SSA which means tracking as much debris as possible at all times. The cost associated with satellite manoeuvring mainly lies in SSA, especially for commercial satellite owners and does not guarantee safety from small debris (less than 10 cm) [35]. SSA information is mainly provided by the US strategic command (USSTRATCOM), and the information is used to validate collision flux predictions made by local space environment models, such as ESA's MASTER model [36]. It should be noted that this approach requires additional fuel expenditure of the satellite and therefore reducing its lifetime, assuming that the systems are in place for the satellite to make the required manoeuvre in the first place. Third, stronger mitigation implementation and/or practices should be agreed upon internationally. This implies that space systems will have to have an end-of-life capability, in accordance with certain guidelines. This, in most cases, means new satellites will have to carry additional fuel allowing them to either move into a so-called graveyard orbit, or to de-orbit themselves entirely. Lastly, active debris removal (ADR) missions can be carried out in order to remove current high-threat space debris and thereby reduce collision risks and rate of debris generation.

It is currently difficult to decide on a response to dealing with space debris because methods for reliable cost-benefit analysis of all likely scenarios have yet to be developed. Carrying out such an analysis is a daunting task, as it may not actually be possible without enforcing inaccurate assumptions such as: the research and development cost of ADR methods, political costs and restrictions [37, 38], cost of operational downtime of satellites due to debris, SSA cost for collision avoidance and complete mission cost in terms of total amount of fuel and number of missions required in order to stabilise the near-Earth space environment. Another major factor associated with ADR is the risk involved in performing

such missions. The risk of ADR can be transferred into a cost factor via the probability of failure; however, this is highly dependent on the specific ADR approach chosen [27, 33]. A conclusion of many authors, however, is that space debris is causing problems which are only made worse if the current rate of space launches continues and no action is taken to reduce the number of objects in certain orbits [37, 38, 39]. As a result, there is a consensus that in order to preserve the long term use of near-Earth space, large space debris needs to be removed [27], and the sooner solutions are implemented, the higher the effectiveness, and the lower the cost incurred. Moreover, it is concluded that in order to be cost effective and sustainable in the long term, ADR missions should address at least 5 pieces of debris per year [26].

1.2   Literature Review

The literature review presented here is included to give relevant context to the research contribution detailed in this thesis. Based on the background and motivation for this research, a review of current ADR methods and how mission design and method selection is carried out is presented. Furthermore, relevant literature on efficiently carrying out ADR missions including low thrust manoeuvres and multiple debris removal missions is considered. Lastly, the importance of space policy and regulations and some of the challenges associated with this aspect of space missions is touched upon as it is a vital component of ADR missions.

1.2.1   Active Debris Removal

From the analysis on space debris outlined previously, it is likely that ADR is a concept that will become a reality and as such, research has been conducted in order to develop methods to implement ADR. To date, the most prominent ADR methods and concepts have been summarized by Johnson and Klinkrad [40], Shan et al. [41], and Mark and Kamath [42]. Shan et al. groups the ADR methods into two main categories referred to as "capturing" methods and "removal" methods. The main difference between these two groups is that capture methods require a capturing phase whereby the chaser spacecraft and the debris are joined, such that they can be considered as one system for the remainder of the full

de-orbiting mission. Removal methods generally affect the debris in some way, after which the chaser spacecraft leaves the debris to complete the de-orbit mission by itself. This way of classifying ADR methods is adopted by multiple authors and will therefore also be used in this review.

Removal Methods

The most prominent removal methods include drag augmentation systems, electro-dynamic tether (EDT), contactless removal systems, and contact removal systems. Drag augmentation systems include various passive methods of increasing the effect of aerodynamic drag on the debris so that the orbital altitude decays, making such methods viable only in LEO. One such method involves engulfing the space debris with expanding foam in order to increase its surface area. The foam method is researched at ESA by Adrenucci et al. [43], including a full mission scenario and intended targets, as well as types of foam appropriate for such missions. The advantages of foam-based drag augmentation system include the elimination of a capturing phase, in addition to no control required for de-orbiting. Furthermore, this approach can be applied to a multitude of sizes and shapes of debris. Some limitations of the foam approach include: the need to decide on appropriate distances between the chaser deploying the foam and the debris target, applying an appropriate amount of foam, and foam breaking off and becoming space debris. Moreover, shaping dispersion of foam around the target, uncertainty in re-entry behaviour, and applying the foam may introduce momentum to the debris and possibly increase its tumbling motion.

Another drag augmentation solution requires a drag sail to be implemented onto the space debris. The concept of a drag sail is a more thoroughly researched solution, as there is also an option for new satellites to be equipped with drag sails as an end-of-life de-orbiting solution. Again, the drag sail has benefits in terms of not requiring a control system during de-orbit; however, there are some limitations which include the instalment of the drag sail, and the risk of collision with other objects in space as the debris naturally decays with a larger surface area as a result of the drag sail [44]. A technology demonstration mission of the drag sail has been carried out by UTIAS in their CanX7 mission [45] and as part of the European Commission's QB50 programme [46]. Here, a CubeSat equipped with a 1 m long inflatable mast and a 10 m^2 deployable drag sail was placed in orbit, and the sail was

deployed to demonstrate safe initiation of the sail and to validate the effectiveness of using a drag sail in LEO through the rate of orbital altitude decay.

EDTs use the effect of Earth's magnetic fields, which interact with the currents driven, or passively induced in the tether [47]. This interaction acts as a retarding force or as a propulsive force, depending on the direction of the current flow. The dynamics of the system when considering a flexible tether under the control of Lorentz force have been analyzed by Yamaigiwa et. al. [48], highlighting that the system would need stabilization, and the success of the method is highly dependent on the eccentricity of the target orbit. Savioli et al. [49] suggest that the EDT method is most appropriate for debris of mass less than 4,000 kg, although it can be adapted for larger debris. Significant research has also been carried out with the aim of achieving optimized, controlled, and robust deployment of the EDT [50, 51], considering the possible external disturbances to which the system is exposed. Some limitations of EDTs include the large length of tether required, and thus the risk of it being cut by other debris and/or spacecraft. In addition, relatively low forces induced by the EDT result in long de-orbit times which means higher risks of collision during the de-orbit manoeuvre [47].

Contactless removal methods mainly consist of the ion beam shepherd (IBS) and laser systems. The principle idea behind IBS is to eject a highly collimated neutralized plasma beam onto a debris object, which results in lowering the debris altitude. Bombardelli and Pelaez [52] hypothesize that a 5,000 kg target in LEO can be de-orbited within 7 months using a space-based IBS. IBS is also a viable method for re-orbiting debris in GEO. In fact, for objects weighing 1,000 to 2,000 kg, a re-orbiter weighing 1,000 kg with ion engines producing 40 to 100 mN thrust levels can re-orbit GEO debris in 6 to 25 days and would take much less time to return to orbits where other critical debris are situated [53]. IBS is limited by the shape dependency between the plasma and the target interaction [41]. In addition, it is difficult to control the dynamics and the attitude of the target affected by the ion beam [52]. Laser based systems are proposed as a method of removing smaller pieces of debris (1-10 cm) in LEO without contact. These systems can be applied from the surface of Earth or from space directly. For example, Phipps [54] proposes a rapid, head-on interaction in 1040 s, using 2040 kW bursts of 100 picoseconds, 355 nm UV pulses from a space-based station in LEO, such that it can also deal with debris with a diameter of $\sim$100

cm and weighing $\sim 1,000$ kg. Furthermore, Schmitz et al. [55] show that a single laser could already reduce the debris density in low Earth orbit (LEO) by more than 20% in 10 years by targeting small debris (1-10 cm). Although laser systems seem promising and low-cost for debris removal, the impact of removing smaller sized debris is not as large as that of removing larger pieces of debris [26], and the political implications of a given nation or company having access to a laser in space or affecting satellites with a ground-based laser make this method unlikely to be implemented [37].

Finally, a prominent contact removal method is the slingshot approach. Tragesser et al. [56] show the feasibility of momentum exchange in the form of a tether sling via a laboratory demonstration. The tether sling has the potential to store energy and thereby allows removal of debris at relatively low fuel costs. The dynamics for such a system have also been studied [57], progressing to the design of controllers for the spinup and deployment of a tether sling. Such control is proposed in open-loop form [58] and leads to the conclusion that adjusting the tether length should occur at the slowest rate possible, with the main bulk of the energy added to the system after the tether length is correctly adjusted. A similar concept is applied in [59] by Missel and Mortari in order to propose a complete "slingsat" system for debris removal. The slingsat is intended to collect multiple pieces of debris via an optimized path [60] based on efficiency of travel between the debris, ejection velocities required, and sequence timing. The debris is then ejected in a controlled direction, at a controlled velocity to a higher or lower orbit depending on convenience and effectiveness. Some issues arise when considering the impact of the debris and the slingsat during collection. This impact occurs when the slingsat 'scoops' the debris in order to sling it [59]. In addition, correct spin-up and release are critical as the debris needs to be moved without colliding with other objects in space, as well as end up in the correct location.

Capture Methods

Capture methods can be broken down into two sub-groups, namely, contact capture and contactless capture. The contactless methods most relevant to ADR are the electrostatic tractor and the gravitational tractor. The electrostatic tractor is considered for moving defunct satellites in GEO to graveyard orbits [61]. Removal using an electrostatic tractor is achieved by engaging a controlled charge on the target, which results in a Coulomb force

1.2 Literature Review

used to control the relative motion between the chaser and the target. The Coulomb force is used as an electrostatic virtual tether to maintain a fixed separation distance between the chaser and the target, while the chaser uses fuel efficient electric (ion) propulsion to de-orbit the "tethered" system. As a result, little fuel is consumed during re-orbiting by an electrostatic tractor and it has the potential to remove 2-4 pieces of debris per annum [62]. It is important to note that the electrostatic force can vary significantly with the target orientation, especially if the target shape is not spherical. Moreover, in order to maximize the efficiency of an electrostatic tractor, the chaser should be at least the size of the debris that is targeted, which in the case of large GEO satellite can be impractical or even a show-stopper, as a large chaser is cumbersome and costly to launch [62]. Another contact-less capture method that has been proposed is the gravity tractor. This method was initially designed to deflect large asteroids heading towards Earth [63]. The idea behind a gravity tractor is to repeatedly orbit the asteroid and thereby exert a gravitational force on the asteroid in order to deflect it. A similar principle can be applied to large pieces of debris; however, this concept would require a large chaser in order to have the desired effect on the debris and thus equivalently high fuel costs.

The second group of capture methods, contact capture, can be further subdivided into two classes: stiff connection and flexible connection methods, both of which show promising results for ADR. Stiff connection capture methods consist of two main approaches: tentacle capture and robotic arm capture. The former concept has been proposed by Yoshida and Nakanishi [64], and their TAKO flyer concept includes a mothership which carries multiple flyers equipped with tentacles. The mothership is positioned in close proximity to the debris target and a flyer is ejected in order to grab hold of the debris using tentacles. Boosters situated on the flyer are then engaged in order to de-orbit the debris. Further research is conducted in [65] into the clamping mechanism of the tentacle approach. It is concluded that grabbing hold of debris is a sensitive manoeuvre and any damage to the chaser as well as any fragmentation of the debris needs to be avoided. Furthermore, the baseline concept arrived at by Meyer et al. [65] features two tentacles with two degrees of freedom each, as this design was found to provide the best combination of high performance at low risk and low cost. Another single debris mission concept (i.e., no mothership) using tentacle capture is proposed by Chiesa et al. [66], where a framework is outlined for mission de-

11

velopment using tentacle capture to de-orbit large debris situated in LEO. A recent study of the material from which tentacle grippers are made suggests that the chosen material affects the efficiency of the de-orbit mission, depending on the coefficient of friction between the gripper and the target [67]. This means that, if the coefficient of friction between the gripper and the debris is gradually increased, the mechanical efficiency of rigidization is increased, as less shear stress is generated on the external surface of the debris at a given point in time. Having a higher mechanical efficiency results in less time spent, in addition to a lower fuel cost of the rigidization phase.

Alternatively, contact capture using a stiff connector can be achieved using a robotic arm. Castronuovo [68] develops a preliminary mission concept for debris capture using a robotic arm and defines the key stages of such a mission as the follows: phasing with the target, followed by close range rendezvous where the chaser gets close enough to the target so that capture is possible. Next are the capture and docking operations, where the robotic arm is required to capture the debris and stabilize/rigidize the system such that a controlled de-orbit can be performed using the chaser propulsion system. Some considerations are made as to what happens to the chaser after the first piece of debris is removed. Options include servicing and refuelling for additional mission in space or a controlled descent and retrieval on Earth for servicing and relaunch. The most prominent of these solutions is a dual-use system for both ADR using a robotic arm and on-orbit servicing (OOS) of spacecraft (dual-use here refers to using the spacecraft for ADR and OOS within a given mission). This dual use approach can also be more readily justified in terms of funding and long-term technological development [69]. The most challenging stages of a de-orbit mission using robotic arms are identified as the capture phase and the following rigidization stage, which may include docking. Nishida and Kawamoto [48] outline a strategy for capturing of tumbling debris, as it so happens that most critical large debris in LEO are tumbling. Rigidization is achieved using active control as well as introducing a brush type contactor as an end-effector of the robotic arm to decrease the rotational rate of the debris. Gasbarri and Pusculli [70] devise a control strategy for successful deployment of the arm and for grasping the debris without damaging the arm or fragmenting the debris. In order to accommodate the potential tumbling of the debris target and the unknown nature of the tumbling motion, control schemes for adaptive reactionless motion of space manipulators

are proposed [71, 72]. These control schemes are introduced to ensure that the chaser-target system can be stabilized or rigidized after capture so that a controlled fuel-efficient de-orbit phase can be implemented. Preliminary design considerations have been outlined for the use of a robotic manipulator for ADR [73, 74], highlighting that such an approach is theoretically possible and supporting arguments towards a high practical success rate. It is worth noting that multi-arm approaches to ADR have been considered [75, 76, 77]; however, the benefits in terms of rigidization of the system are unlikely going to outweigh the added complexity incurred by relative control and path generation needed for multiple arms. In addition, with multiple arms there is a higher risk of collision between the arms and the debris itself. Some limitations also include the requirement of a graspable location on the debris itself, as well as the high likelihood of nudging the debris during capture and pushing it further away or out of reach of the chaser spacecraft. An ADR mission (ClearSpace, former e.Deorbit) using a tentacle capture method (four robotic arms) for a large piece of orbital debris in LEO is planned to be carried out by ESA in the 2021-2023 period [78]; however, the mission has been pushed back and is now expected to be carried out in 2025.

When considering flexible connection removal methods, both the nature of the flexible connection (the tether) and the method of connecting the tether to the debris are of great importance. There are two dominant methods of capture using a flexible connection as identified in [79], namely, net capture and harpoon capture. The harpoon capture method is considered a simple, lightweight and compact approach with limited complexity [80] as compared to other ADR capture methods. The difficulty associated with harpoons lies in the damaging nature of the attachment; here, the harpoon needs to penetrate the target with minimum damage and minimize any fragmentation. Furthermore, the harpoon needs to be sufficiently secure to avoid losing the connection once the tether is attached. Testing has demonstrated that using a harpoon as a capture method is viable for targets with no danger of explosion (left over fuel) and when the target material is such that additional debris created upon impact between the harpoon and the target is minimized [81]. Test results show that impacting common aerospace materials like aluminium results in very few debris fragments at sub 1 mm sizes whereas impact with carbon fibre reinforced polymer (CFRP) causes a much higher number of debris fragments to break off, some of which are

on the order of 10 mm in size [80]. Net capture differs from harpoons in that damaging the target is unlikely; however, this approach is more complicated in that the net will have to be deployed correctly and engulf the target in such a manner that it is not unravelled when tension is applied through the attached tether. Experiments in micro gravity environments [82] together with complex dynamics modelling of the net capture phase [83] have been carried out to ensure the debris is entangled correctly. In addition, the correct target to chaser distance is investigated for successful net capture [84] to minimize the risk of failure during the deployment phase. Liu et al. [85] explores the effects of net capture on the dynamics of a tethered net target-chaser system in GEO, showing that this method is applicable for ADR outside of LEO as well. Furthermore, the results show that the initial conditions and the thrust applied by the chaser have significant impact on the de-orbit phase of the ADR mission. A technology demonstration mission was carried out known as the RemoveDEBRIS mission in 2018 in which a net, a harpoon, vision-based navigation and a drag sail were utilized in a realistic space environment. During the mission, two Cube-Sats ware ejected and then used as targets instead of real space debris for demonstration purposes [86, 87].

The flexible connection chaser-debris system is a subset of the more general tethered space system, (TSS) which has been researched extensively in the past. The dynamics behaviour of a TSS is established for a target-chaser system connected by a flexible tether [88, 89], showing that the tether parameters such as length, diameter, and material properties (e.g., Young's modulus) affect the oscillatory behaviour of the tether once the chaser thrusters are engaged [90]. Dynamics analysis of TSS is taken further and applied to more specific scenarios such as the effect of debris appendages on the dynamics [90] and the existence of chaotic behaviour when de-orbiting a TSS using low thrust [91]. The oscillatory nature of a TSS has the potential to decrease the efficiency of the de-orbit phase or, in the worst-case, result in a collision between the chaser and the target [92]. Therefore, some control schemes would have to be implemented in order to maintain the chaser attitude, the optimum descent orbit, and a safe distance between the chaser and the target [92, 93, 94]. For example, one way of dealing with TSS oscillations is to shape the input thrust levels when de-orbiting space debris [95, 96]. In order to have optimal initial conditions for the de-orbit phase using a TSS, it is important to de-tumble the debris prior to the initiation of

the de-orbit manoeuvre. O'Connor et al. [97] as well as Linskens and Mooij [92] predict that this de-tumble will occur naturally as tension is applied to the tether. Furthermore, the de-tumble will occur more efficiently using a net rather than a harpoon, as there are multiple points of contact between the net and the debris, as opposed to just one with the harpoon.

1.2.2 Mission Design and Method selection

ADR mission design requires extensive planning, involving not only deciding which debris to remove but also which method to implement in order to maximize the gain with minimal cost and risk. The first step is to classify the debris according to selected criteria. Van der Pas et al. [98] suggest using the orbital characteristics of the debris i.e., the altitude, the inclination and the right ascension of the ascending node (RAAN) as well as the collision probability to create a list of priority targets. A similar approach is taken by Kawamoto et al. [99] where further considerations are made in terms of accurately calculating the collision risk in predefined altitude bins for an ever-evolving space debris environment. Jankovic and Kirchner [100] have developed a full taxonomy for categorizing space debris in LEO. The first level of the taxonomy categorizes debris using TLE information [12] to determine the orbital state of the debris. The ability of the debris to control its attitude is then assessed, followed by the shape, size and area-to-mass ratio of the debris. Such characterisations allow for different groupings of debris to be made depending on mission objectives/limitations. The second level of the taxonomy assesses the risk of explosion of a certain piece of debris based on remaining fuel, as well as risk of debris breakup. The latter is estimated using the ESA database of satellite material properties. Once such information is obtained, informed decisions can be made as to which methods are appropriate for individual pieces of debris.

Given the high cost of space missions, the financial and economic factors also need to be taken into account [36, 92]. The cost associated with an ADR mission is difficult to predict, as there are many contributing factors. Factors affecting cost include not only the method chosen for capture of the debris but also fuel requirements, the propulsion system used for de-orbit (high/low/none), and the predicted impact the mission will have on the overall near-Earth space environment. Yamamoto et al. [101] propose an extensive cost

analysis of ADR scenarios where factors such as the architecture of removal activity, the propulsion technology for de-orbit, the debris orbital parameters, and the debris mass are used as components for a quantitative trade-off study on ADR cost. Further research in the use of hybrid propulsion solutions has been conducted [102] and considered a promising alternative to conventional liquid propellant in-orbit propulsion systems. Hybrid propulsion systems are designed such that they can provide a range of specific impulses for different stages of a given mission. Improvements of using hybrid propulsion are evident in terms of reduced complexity and cost in addition to ease of operation, while allowing for the use of non-toxic propellants. Comparing the cost of the individual methods alone is no easy feat due to the vast differences between the methods.

ADR missions require multiple orbital transfers and other procedures such as capture that rely on thrust and therefore fuel expenditure. As such, low-thrust propulsion is a cost-effective solution not only for attitude and orbital correction procedures but for orbital transfers as well. Low-thrust orbital manoeuvres have been an integral part of deep space and interplanetary missions for a long time, and optimizing these manoeuvres has been a topic of extensive research including, among many others, work done by Edelbaum in the 1960s [1], as well as key contributions by Betts [103, 104], and more recent work by Hernandez and Akella [105]. Current electric propulsion systems can provide very high specific thrusts, resulting in a much lower propellant mass [106], compared to using other propulsion systems such as chemical or hybrid. Electric propulsion systems have made it possible to achieve optimized low-thrust rendezvous. Furthermore, low-thrust orbital transfers require a high number of revolutions and as such spacecraft trajectory optimization for the many-revolution orbital transfer problem has a high number of problem variables. This, combined with the increased influence of perturbing accelerations over time, prevent or complicate accurate analytical solutions to achieving optimized low-thrust orbital transfers. To solve such optimization problems, in-depth research has been conducted into suitable algorithms for solving optimized low thrust transfers in space [103, 107].

Another key aspect of the ADR mission design is the potential collision risks during the ADR mission itself. A study by Lidtke et al. [108] examines the probability of an on-orbit collision between an ADR target being de-orbited and other space debris in that region. This analysis is particularly appropriate for LEO, where key ADR targets are situated in

densely populated orbits. Due to the emergence of mega constellation concepts, there is a need to assess the impact these constellations will have on the space debris environment [109]. As a result, these constellations will increase the collision risk in LEO, especially if ADR missions target satellites within the constellations themselves.

If priority is placed on removing large debris in LEO, several prominent methods emerge. These are identified by analyzing the cost efficiency and risk of using a given method for specified pieces of debris [39, 110] and by utilizing data from previous space missions using similar technology to that required for certain ADR approaches. For example, the use of robotic manipulators in space is not a novel concept for ADR and has been proven to work for on-orbit servicing [111]. This implies that spacecraft such as the "Dream Chaser" [111] can be adapted for ADR missions to save on development cost and to avoid the risk arising from the use of novel technology. Other prominent ADR technologies that are further developed and have, to some extent, been tested include TSS and tentacle capture [100]. Furthermore, Anselmo and Pardini have specifically ranked large (> 3,000 kg) ADR targets in LEO through a normalized and dimensionless ranking index using a nearly 1-tonne object placed into an 800 km sun-synchronous orbit as a benchmark [112]. The ranking system is based on the probability of catastrophic breakup due to a collision with a piece of orbital debris and the number of new "projectiles" resulting from the breakup, coupled with the long-term impact on the environment as a function of the lifetime of the cloud of fragments generated, the volume of space involved, and the interaction with the pre-existing debris distribution. A similar approach is taken by the same authors to rank rocket upper stages in LEO as well [113]. ADR methods for removing large debris which appear more promising at this point in time are the stiff connector and flexible connector capture methods. The main difficulties lie in the complex nature of the rendezvous, capture, and rigidization phase associated with stiff connector methods [70, 71], whereas the complexity of flexible connector methods arise in the de-orbit stage [92, 114]. Therefore, in order to compare the cost of these methods, the costs associated with the fuel use in each phase of ADR as well as development costs, weight of the system (hence launch cost) and other factors such as multi-debris capabilities would need to be taken into account.

1.2.3 Multiple Debris Removal Missions

An emerging consideration for ADR missions is the possibility of removing multiple pieces of debris in a single mission and the benefits, if any, of doing so [115, 116, 117]. Multiple debris missions are important from a financial perspective but also from a timing perspective, especially if five pieces of debris are to be removed per year [26, 98]. In fact, for this to be a realistic goal on a consistent basis, the implementation of multi-debris removal missions is a necessity, not an option.

Multi-debris missions can be broadly categorized as those where a mothership travels from one debris to the next, deploying packets which attach to and de-orbit the debris. The other category involves a chaser de-orbiting the targeted debris and then returning to another orbit in order to de-orbit another piece of debris [118]. There is a direct mapping between these two categories of multi-debris missions, and whether a removal or capture method is chosen. For the scenario involving a mothership, removal methods are more suitable as these methods are amenable to having a mothership equipped for multiple debris removal. In this case, path optimization is a key factor, since the trajectory that the mothership needs to take between pieces of debris would need to be optimized such that fuel is minimized. This is partially achieved through target selection [98], but there is also a dependency on the orbital positions of the debris at a given time [118, 119].

The time-dependent positions of the debris mean target sequencing also plays an important role in multi-debris removal missions [120]. To minimize mission cost, a variant of the travelling salesman problem has been solved to find the best possible sequence of removal for a given set of debris [116, 117]. This idea is taken further by Bang and Ahn [121] by addressing the optimal multitarget rendezvous problem in a scenario where multiple chaser spacecraft are used. As for the second multi-debris removal scenario where the chaser removes each debris recursively, the chaser and the debris de-orbiting collectively making it a more suitable approach for capture methods since the chaser and the target move as a single system during the de-orbit phase. Although little research is available on this scenario at the present, a viable approach for this type of multi-debris removal would be capture methods such as tethered net capture in which tugging is required, or robotic arm capture in which a rigid connection is formed between the chaser and the debris. Fi-

nally, as nets are relatively light and compact, one chaser could carry multiple net packets to remove multiple debris in one mission. Previously mentioned ADR methods that have been explicitly suggested for multi-debris missions are the "slingsat" [59], an electrostatic tractor [62], and the "TAKO flyer" [64].

1.2.4   Space Policy and Regulations

Within the aerospace community, it is accepted that on an international scale, the U.N. space treaties do not address the issue of space debris directly, mainly due to the fact that at the time the treaties were adopted, space debris was not a primary concern. As such, there is regular debate as to who is responsible for problems and concerns with space debris. Some concerns expressed by Froehlich et al. [122] in a compressive study on the legal aspects of ADR include cooperation and dispute resolution at an international level to solve problems related to space debris using ADR; jurisdiction and maintaining control in the space debris environment; distinctions between ADR solutions and potential spaced based weapons; the extent to which there is a lack of regulation for the space debris environment; and how to proceed in terms of policy and guidelines implementation. As such, numerous barriers to and challenges of ADR missions exist that are completely unrelated to engineering solutions and technological development. To address some of these issues, policy tools and legal frameworks have been proposed [123, 124]. One suggestion for resolving legal problems relevant to space debris is to establish an international regulatory framework as well as an intergovernmental organization that will conduct ADR and OOS activities. Furthermore, guidelines are being implemented and adhered to on a national level [124, 125]. These guidelines, as mentioned previously, not only limit the time in orbit of spacecraft after the end of a mission, but also regulate, among other things, spacecraft end-of-life procedures, risk of re-entry, SSA requirements, and ADR requirements in terms of objects being removed to alleviate the probability of collision. Efforts to provide universal guidelines and standards relating to space debris were pioneered by the Inter-Agency Space Debris Coordination Committee (IADC) and are supported by the UN General Assembly (UNGA) and The Scientific and Technical Subcommittee of the United Nations Committee on the Peaceful Uses of Outer Space (UNCOPUOS).

Promising solutions for ADR of large debris in LEO all result in debris re-entry either

controlled, where the re-entry is ensured to occur over a predetermined area within which the debris impacts Earth, or uncontrolled, where the debris is left to re-enter without any external influence. It is important to bear in mind the hazard to people and property due to randomly re-entering satellites, rocket bodies, and other man-made hardware [126]. Therefore, ADR missions are not only a matter of reducing the orbital lifetime of debris, but the debris re-entry issues must also be considered as part of the ADR mission. Furthermore, for debris with a large mass, the entirety of the hardware will not burn up in the atmosphere during re-entry. In order to guarantee the location of surviving debris impact with Earth, controlled re-entry is required. In the event that controlled re-entry is not an option, the debris will re-enter uncontrollably, and any remaining mass will impact Earth. Such events have occurred and will happen in the future [127]. The probability of impact with either human property or the population itself is small, albeit not negligible. Therefore, for ADR missions in which large debris is considered, uncontrolled re-entry would pose a human casualty risk. It is thus suggested that, controlled re-entry is difficult and costly to achieve; however, the uncontrolled re-entry of large debris may pose high casualty risk factors [128], which do not comply with internationally recognized space debris guidelines. These guidelines stem from the IADC space debris mitigation guidelines [129], which have been adapted by the UN and released as UN space debris mitigation guidelines [130]. A nominal risk factor used for categorizing re-entry is 1:10,000 chance of human collision [128], i.e., the risk of human casualty from a spacecraft component re-entry should be no more than 1 in 10,000 or 10e-4.

1.3   Thesis Outline

Given the current state of space debris orbiting Earth and specifically the development of ADR for large space debris in LEO, the research presented in this thesis is motivated by achieving efficient and cost-effective remediation of the space debris environment. As such, the research focuses on the fundamental analysis required to carry out much needed multiple debris removal missions by taking advantage of low-thrust propulsion efficiency to perform LEO transfers. More specifically, the focus is on large debris rendezvous and de-orbit manoeuvres using low thrust orbital dynamics to achieve multiple ADR in a cost-efficient manner, within a specified time frame. The analysis includes appropriate debris

target selection and the use of so-called 'drift orbits', such that the mission is fuel efficient while maintaining as high a collision risk reduction as possible. In addition, a detailed analysis of factors affecting uncontrolled re-entry is conducted, and how these can be manipulated to minimize casualty risk. As such, the format of this thesis is as follows: First, definitions, equations, and software tools used as part of the research carried out for this thesis, will be outlined in Chapter 2. This includes a summary of reference frames used as part of the orbital dynamics, definitions of orbital elements used, and the resultant equations of motion. The key software tools used, apart from MATLAB, are GPOPS-II, D-SPOSE, DRAMA and DAS. In Chapter 3, the motion planning problem for multiple debris removal is described based on whether impulsive or low continuous thrust is assumed, for both rendezvous and de-orbit, highlighting relevant aspects unique to multiple debris removal. Methods for solving the multiple debris removal motion planning problem are presented in Chapter 3 and applied to several case studies in Chapter 4, each containing multiple pieces of debris with different relevant characteristics in terms of orbital parameters. Specific considerations made in terms of the release and re-entry phase of a multiple debris removal mission are presented in Chapter 5. Here, the release orbit criteria are defined, and the release orbit selection process is outlined. Moreover, the effects of releasing the debris with impulses of varying magnitude and direction are described, in addition to the effects of attitude motion on the re-entry characteristics of the debris. Finally, Chapter 6 summarizes the contributions of this thesis and provides suggestions for future work within this domain of space debris research.

2

Definitions, Equations, and Software Tools

Before analysing an active debris removal mission, it is important to clearly define the spacecraft dynamics and thereby any relevant reference frames and equations of motion relating to the problem at hand. In this light, the relevant reference frames used for the work presented in this thesis are defined in Section 2.1, and the equations of motion used to propagate the chaser spacecraft as part of the ADR mission optimization are defined in Section 2.2. To aid aspects of the analysis, certain specialized software tools have been utilized and these are described in some detail in Section 2.3

2.1 Reference Frames

Various reference frames and coordinate systems are used throughout this thesis to describe the effects of different external torques and accelerations. Within this section, each reference frame used is described to highlight their specific utility and the importance of keeping track of which reference frame is required for a particular scenario, such that the results are interpreted correctly.

2.1.1 Earth-Centered Inertial Frame

Among various existing inertial frames in astrodynamics, Earth-centered inertial (ECI) frames are commonly used when studying satellites orbiting Earth [131]. The ECI frame primarily used for the work presented here is J2000, which is defined by Earth's mean

equator and mean equinox on January 1, 2000 at noon. Although not directly applicable to the contributions of this thesis, it is worth noting that the D-SPOSE software described in Section 2.3.2 uses a quasi-inertial frame, named the True-Equator Mean-Equinox (TEME) frame. This frame corresponds to the reference frame of Two-Line Element (TLE) sets describing the position of space objects at a given point in time; TLEs are maintained by the North American Aerospace Defense Command (NORAD) [12]. These TLEs are used throughout this work and are described in detail in Section 2.1.2.

Figure 2.1 illustrates the ECI frame represented by the $\mathbf{X}$-$\mathbf{Y}$-$\mathbf{Z}$ axes. In addition, for the purpose of describing the evolution of a space debris spin axis, it can be useful to describe the orientation of a vector in terms of two angles in the ECI frame. The two angles are defined for a vector $\mathbf{r}$ in Figure 2.1, as the declination θ_{dec} and the right ascension λ_{ra}.
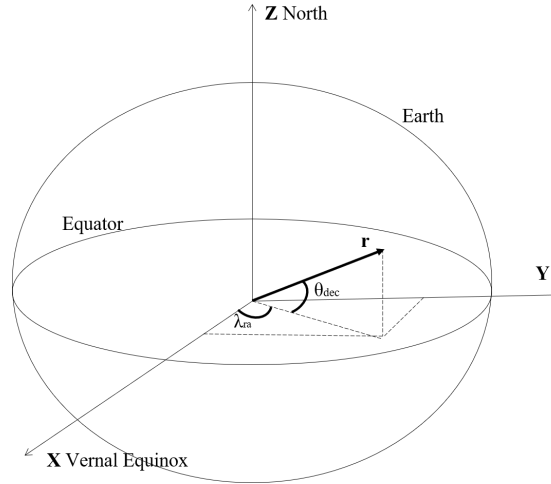
Figure 2.1: Earth centered inertial frame (X,Y,Z), declination angle θ_{dec}, and right ascension angle λ_{ra}

2.1.2 Earth-Centered Orbital Frame

For a given satellite orbit, the Earth-centered orbital (ECO) frame can be defined. The ECO frame rotates with said orbit and is defined by $\mathbf{x}_0$ pointing towards the ascending node and $\mathbf{z}_0$ pointing along the orbit normal. Now, in order to define the ECO for a specific orbit, the orbit must be defined in terms of shape, size, and orientation, with respect to Earth. To

2.1 Reference Frames

define the shape and size of a satellite's orbit as well as the position of the satellite within that orbit, six parameters known as orbital elements are most commonly used. Figure 2.2 shows the ECO frame with respect to the ECI frame as a function of orbital inclination and right ascension of the ascending node.
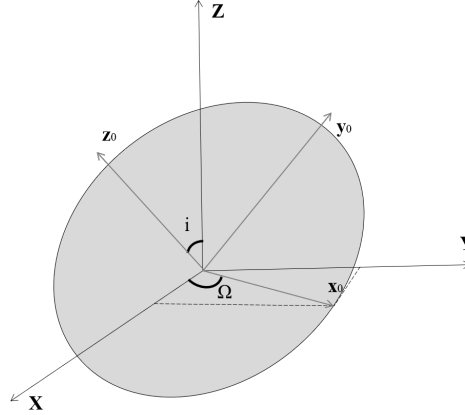
Figure 2.2: Earth centered orbital frame ($\mathbf{x}_0$, $\mathbf{y}_0$, $\mathbf{z}_0$), orbital inclination angle i, and right ascension of the ascending node Ω

Classical Orbital Elements

The classical set of orbital elements are defined as semi-major axis (a, km), eccentricity (e), inclination (i, rad), right-ascension-of-the-ascending-node (RAAN, Ω, rad), argument of perigee (ω, rad), and true anomaly (θ, rad). The semi-major axis defines the size of the orbit, the eccentricity its shape, the triplet of angles—inclination, RAAN, and argument of perigee—define the orientation of the orbit in the inertial frame, and the true anomaly locates the position of the satellite along the orbit path. These elements are illustrated and defined in Figure 2.3.

The before mentioned TLE data sets, shown in Figure 2.4, have a legacy format which was defined in the 1960s. These TLEs are frequently published to this day and contain information related to the epoch and orbital elements of the orbiting object being monitored, as defined in Figure 2.4.
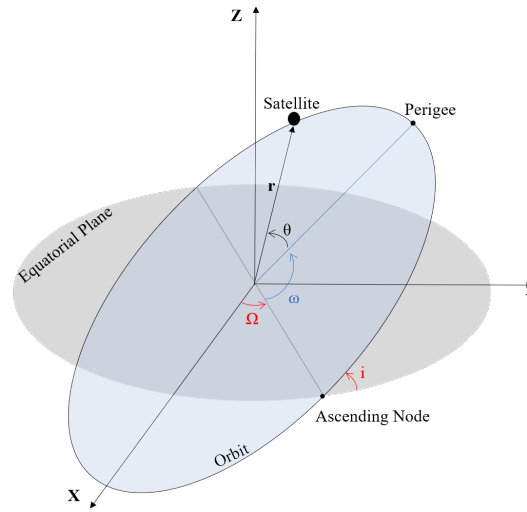
Figure 2.3: The classical orbital elements

Figure 2.4: Two-line-element set example and content

Equinoctial Elements

An alternative to the classical orbital elements are the modified equinoctial orbital elements: (p, f, g, h, k, L) where p is the semi-latus rectum, f and g are elements that describe the eccentricity, h and k are elements that describe the inclination, and L is the true longitude. Modified equinoctial elements are used as opposed to classical orbital elements to avoid numerical singularities associated with zero eccentricity and/or 90° inclination [104]. Singularities associated with zero eccentricity arise when optimizing orbital transfers between circular and near circular orbits and orbits with near 90° inclination. A significant proportion of high risk space debris in LEO exist in near circular orbits, many of which are

25

high utility sun-synchronous orbits, i.e., near 90° inclination. As such, to avoid numerical errors when using actual debris data for case studies, the modified equinoctial elements are used to define the minimum-time low-thrust optimal control problem in Section 3.6. The modified equinoctial elements can be found from the orbital elements using the following standard equations:

$$p = a(1 - e^2) \tag{2.1}$$
$$f = e\cos(\omega + \Omega) \tag{2.2}$$
$$g = e\sin(\omega + \Omega) \tag{2.3}$$
$$h = \tan(0.5i)\sin(\Omega) \tag{2.4}$$
$$k = \tan(0.5i)\cos(\Omega) \tag{2.5}$$
$$L = \Omega + \omega + \theta \tag{2.6}$$

The equinoctial elements presented here are modified from the original set [3] by replacing the semi-major axis a with the semi-latus rectum p in order to make the formulation viable for all types of orbits, specifically highly eccentric and hyperbolic orbits. Furthermore, the mean longitude λ is replaced with the true longitude L such that perturbations can be tracked on the true anomaly θ, as it is a fast variable.

2.1.3 Satellite-Centered Orbital Frame

Satellite-centered orbital (SCO) frames are defined such that they are fixed with the motion of the satellite in orbit, meaning the frame is oriented based on the direction of motion of the satellite. These frames are convenient when satellite perturbations which are dependent on the satellite direction of motion are analyzed. The SCO frame is related to the ECI frame by the position vector **r** and velocity vector **v** in the ECI frame. However, unlike the ECO frame, the SCO frame is centered at the satellite center of mass as opposed to the Earth's center of mass. Illustrated in Figure 2.5 is the SCO frame **x**-**y**-**z** used to define a change in velocity ΔV, the directions of which are defined in terms of the satellite flight path angle γ and the satellite heading angle χ. Here, the **x**-axis is in the spacecraft velocity direction, the **z**-axis points towards Earth in the orbital plane, and the **y**-axis completes the right hand rule.
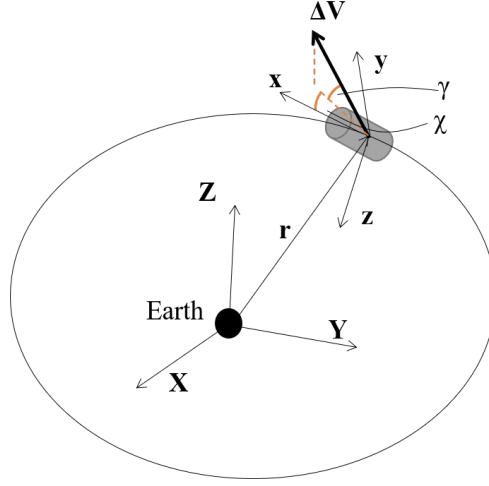
Figure 2.5: Satellite-centered orbital frame ($\mathbf{x}$, $\mathbf{y}$, $\mathbf{z}$), flight path angle γ, and heading angle χ

Another SCO frame known as the rotating radial frame ($\mathbf{i}_r$-$\mathbf{i}_\theta$-$\mathbf{i}_h$), illustrated in Figure 2.6, is used to define spacecraft acceleration contributions due to gravity and thrust. It should be noted that, for circular orbits, the rotating radial frame and frame $\mathbf{x} - \mathbf{y} - \mathbf{z}$ are identical with the exception that the r-axis points away from Earth where the z-axis points towards it and the y- and h- axes are defined by the right hand rule accordingly. Each unit vector used to construct the rotating radial frame is defined as

$$\mathbf{i}_r = \frac{\mathbf{r}}{\|\mathbf{r}\|}, \quad \mathbf{i}_\theta = \mathbf{i}_h \times \mathbf{i}_r, \quad \mathbf{i}_h = \frac{\mathbf{r} \times \mathbf{v}}{\|\mathbf{r} \times \mathbf{v}\|} \tag{2.7}$$

where $\mathbf{r}$ and $\mathbf{v}$ are the chaser position and velocity vectors, respectively, in the ECI frame. This frame will be used in Section 2.2 to define the equations of motion of the chaser spacecraft which, in turn, are used in Section 3.6.2 to solve the minimum-time low-thrust optimal control problem. The rotation matrix from rotating radial coordinates to Earth-centered inertial coordinates $\mathbf{Q}_r$ is defined as

$$\mathbf{Q}_r = \begin{bmatrix} \mathbf{i}_r & \mathbf{i}_\theta & \mathbf{i}_h \end{bmatrix} \tag{2.8}$$
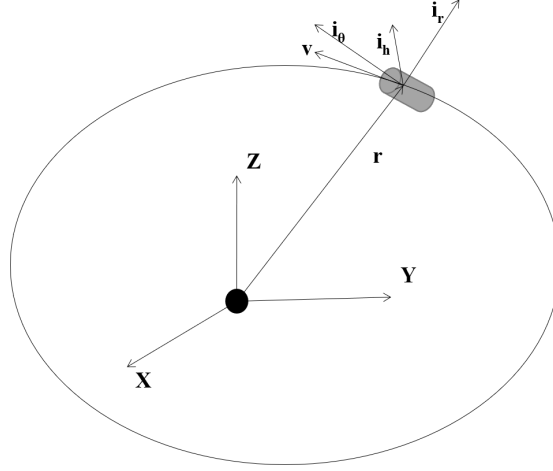
Figure 2.6: Rotating radial frame ($\mathbf{i}_r$, $\mathbf{i}_\theta$, $\mathbf{i}_h$)

2.1.4 Body-Fixed Frame

The body-fixed frame is defined for each individual spacecraft or debris and is fixed with the rigid body of said object. The body-fixed reference frame is primarily used to define debris orientation and attitude dynamics, as well as its surface geometry. A simplified surface geometry model for an SL-8 rocket body in the body-fixed frame is presented in Figure 2.7.

2.2 Equations of Motion

Providing active debris removal in LEO requires an accurate rendezvous between the chaser spacecraft and the debris. In order to achieve such a rendezvous, the optimal thrust directions, described as components in the SCO rotating radial frame as (u_r, u_θ, u_h), which minimize the time taken for a spacecraft to move from one point in space (defined by orbital elements) to another must be identified, as depicted in Figure 2.8. In order to design any orbital transfer in space, the equations of motion of the chaser need to be defined along with the initial and desired chaser locations, otherwise referred to as the boundary conditions. Initially, the orbits used as boundary conditions are defined using standard orbital elements, as they provide a more intuitive understanding of the orbits than the Cartesian position and velocity. Moreover, we will need the orbital elements to define the low-thrust
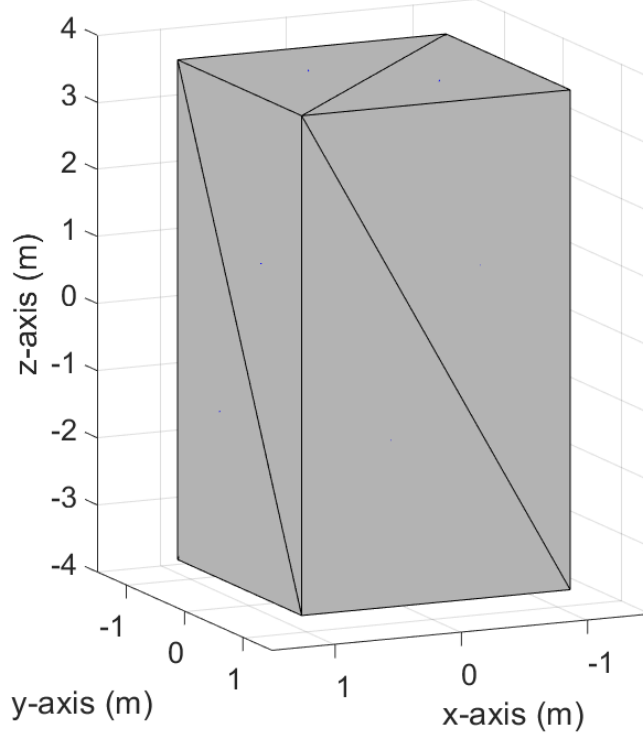
Figure 2.7: SL-8 debris geometry for simulation with the body-fixed x-axis, y-axis, and z-axis

chaser dynamics. Specifically for low-thrust accurate rendezvous, the debris dynamics also need to be propagated such that the chaser is transferred to the actual debris location after a given transfer time.

In this work, the dynamics of the chaser spacecraft are propagated using the modified equinoctial elements (p, f, g, h, k, L) [3, 132] as defined in Section 2.1.2. The propagation dynamics of the debris are described in Section 2.2.2. The differential equations of motion of the chaser in terms of equinoctial elements are then given as [132]:
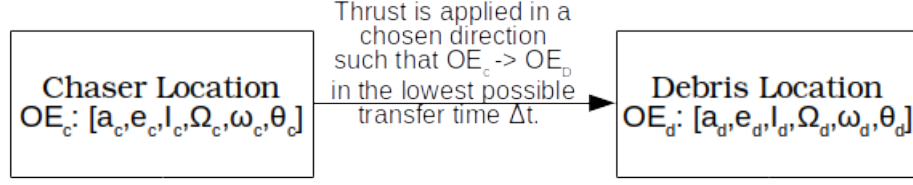
Figure 2.8: Point-to-point transfer concept

$$\frac{dp}{dt} = \sqrt{\frac{p}{\mu_e}} \frac{2p}{q} \Delta_\theta \tag{2.9}$$

$$\frac{df}{dt} = \sqrt{\frac{p}{\mu_e}} \left(\sin L \Delta_r + \frac{1}{q}((q+1)\cos L + f)\Delta_\theta - \frac{g}{q}(h\sin L - k\cos L)\Delta_h \right) \tag{2.10}$$

$$\frac{dg}{dt} = \sqrt{\frac{p}{\mu_e}} \left(-\cos L \Delta_r + \frac{1}{q}((q+1)\sin L + g)\Delta_\theta - \frac{f}{q}(h\sin L - k\cos L)\Delta_h \right) \tag{2.11}$$

$$\frac{dh}{dt} = \sqrt{\frac{p}{\mu_e}} \frac{s^2 \cos L}{2q} \Delta_h \tag{2.12}$$

$$\frac{dk}{dt} = \sqrt{\frac{p}{\mu_e}} \frac{s^2 \sin L}{2q} \Delta_h \tag{2.13}$$

$$\frac{dL}{dt} = \sqrt{\frac{p}{\mu_e}}(h\sin L - k\cos L)\Delta_h + \sqrt{\mu_e p}(\frac{q}{p})^2 \tag{2.14}$$

where

$$q = 1 + f\cos L + g\sin L$$
$$s^2 = 1 + \sqrt{h^2 + k^2} \tag{2.15}$$

and μ_e is the gravitational constant for the Earth, and g_e is the acceleration due to gravity at the surface of the Earth. In order to keep track of fuel expenditure for a given transfer, the rate of change of mass m of the spacecraft is given as:

$$\frac{dm}{dt} = -\frac{T}{g_e I_{sp}} \tag{2.16}$$

where T is the constant thrust of the propulsion system, and I_{sp} is the specific impulse of the propulsion system. The chaser acceleration components described in the rotating radial

2.2 Equations of Motion

frame as Δ_r, Δ_θ, and Δ_h arise due to the thrust accelerating the chaser itself as well as the perturbations affecting the spacecraft, all of which are defined in Section 2.2.1. The values used for the physical constants needed to evaluate Eqs. (2.9-2.16) can be found in the top half of Table 2.1. For the simulations in this research, time is replaced by true longitude L as the independent variable, using the method described in [133], as the transfers require a large number of revolutions around the Earth. The relationship between t and L is given by Eq. (2.14) and the equations of motion in terms of L are found by taking the inverse of Eq. (2.14) and multiplying Eqs. (2.9-2.13), and (2.16) by said inverse, the result of which is given as:

$$\frac{dt}{dL} = \frac{1}{\sqrt{\frac{p}{\mu_e}}(h\sin L - k\cos L)\Delta_h + \sqrt{\mu_e p}(\frac{q}{p})^2} \tag{2.17}$$

$$\frac{dp}{dL} = \frac{\sqrt{\frac{p}{\mu_e}}\frac{2p}{q}\Delta_\theta}{\sqrt{\frac{p}{\mu_e}}(h\sin L - k\cos L)\Delta_h + \sqrt{\mu_e p}(\frac{q}{p})^2} \tag{2.18}$$

$$\frac{df}{dL} = \frac{\sqrt{\frac{p}{\mu_e}}(\sin L\Delta_r + \frac{1}{q}((q+1)\cos L + f)\Delta_\theta - \frac{g}{q}(h\sin L - k\cos L)\Delta_h)}{\sqrt{\frac{p}{\mu_e}}(h\sin L - k\cos L)\Delta_h + \sqrt{\mu_e p}(\frac{q}{p})^2} \tag{2.19}$$

$$\frac{dg}{dL} = \frac{\sqrt{\frac{p}{\mu_e}}(-\cos L\Delta_r + \frac{1}{q}((q+1)\sin L + g)\Delta_\theta - \frac{f}{q}(h\sin L - k\cos L)\Delta_h)}{\sqrt{\frac{p}{\mu_e}}(h\sin L - k\cos L)\Delta_h + \sqrt{\mu_e p}(\frac{q}{p})^2} \tag{2.20}$$

$$\frac{dh}{dL} = \frac{\sqrt{\frac{p}{\mu_e}}\frac{s^2\cos L}{2q}\Delta_h}{\sqrt{\frac{p}{\mu_e}}(h\sin L - k\cos L)\Delta_h + \sqrt{\mu_e p}(\frac{q}{p})^2} \tag{2.21}$$

$$\frac{dk}{dL} = \frac{\sqrt{\frac{p}{\mu_e}}\frac{s^2\sin L}{2q}\Delta_h}{\sqrt{\frac{p}{\mu_e}}(h\sin L - k\cos L)\Delta_h + \sqrt{\mu_e p}(\frac{q}{p})^2} \tag{2.22}$$

31

Constant	Value
g_e	$9.807 \times 10^{-3} \; kms^{-1}$
R_e	$6378.1363 \; km$
μ_e	$398600.442 \; km^3 s^{-2}$
J_2	1082.639×10^{-6}
J_3	-2.565×10^{-6}
J_4	-1.608×10^{-6}

Table 2.1: Physical properties (from the geopotential model EGM 2008 [5])

2.2.1 Chaser Acceleration

The chaser acceleration expressed in the radial chaser frame, $\boldsymbol{\Delta} = (\Delta_r, \Delta_\theta, \Delta_h)$, is modelled as

$$\boldsymbol{\Delta} = \boldsymbol{\Delta}_g + \boldsymbol{\Delta}_T \tag{2.23}$$

where $\boldsymbol{\Delta}_g$ is the gravitational acceleration due to the oblateness of the Earth and $\boldsymbol{\Delta}_T$ is the thrust specific force [1]. The acceleration due to Earth oblateness is expressed in rotating radial coordinates as

$$\boldsymbol{\Delta}_g = \mathbf{Q}_r^T \delta \mathbf{g} \tag{2.24}$$

where $\mathbf{Q}_r = [\mathbf{i}_r \; \mathbf{i}_\theta \; \mathbf{i}_h]$ is the rotation matrix from rotating radial coordinates to Earth-centered inertial coordinates defined in Section 2.1.3. Furthermore, the vector $\delta \mathbf{g}$ is defined as

$$\delta \mathbf{g} = \delta g_n \mathbf{i}_n - \delta g_r \mathbf{i}_r \tag{2.25}$$

where $\mathbf{i}_n$ is the local North direction, defined in the ECI frame as

$$\mathbf{i}_n = \frac{\mathbf{e}_Z - (\mathbf{e}_Z^T \mathbf{i}_r)\mathbf{i}_r}{||\mathbf{e}_Z - (\mathbf{e}_Z^T \mathbf{i}_r)\mathbf{i}_r||} \tag{2.26}$$

---

[1]Although aerodynamic drag is significant, especially during the lower altitude segments of the transfers, it is not included in the formulation for chaser acceleration. Attempts to include aerodynamic drag increased the computational time prohibitively and did not result in a converged solution.

with $\mathbf{e}_Z = (0, 0, 1)$ representing the unit vector in the Z-direction in the ECI frame. The oblate Earth perturbations are then expressed as

$$\delta g_r = -\frac{\mu_e}{l^2} \sum_{k=2}^{4} (k+1) \left(\frac{R_e}{l}\right)^k P_k(\sin \phi) J_k \tag{2.27}$$

$$\delta g_n = -\frac{\mu_e \cos \phi}{l^2} \sum_{k=2}^{4} \left(\frac{R_e}{l}\right)^k P_k'(\sin \phi) J_k \tag{2.28}$$

where $l = p/q$, R_e is the equatorial radius of the Earth, P_k is the kth-degree Legendre polynomial, P_k' is the derivative of P_k with respect to $\sin \phi$, and J_k represents the zonal harmonic coefficients for $k = (2, 3, 4)$, stated in Table 2.1. Beyond the fourth term, the effects are considered negligible for the purpose of this research.

The thrust specific force is given as

$$\mathbf{\Delta}_T = \frac{T}{m}\mathbf{u} \tag{2.29}$$

where

$$\mathbf{u} = \left(u_r, u_\theta, u_h\right) \tag{2.30}$$

represents the thrust direction and is a unit vector. Additional perturbations can be added to the chaser acceleration analysis; however, this increases the computational cost significantly for the given procedure.

2.2.2 Debris Propagation

The propagation equations of debris used for rendezvous include the same gravitational effects as for the chaser (defined by the gravitational acceleration $\mathbf{\Delta}_g$) and by definition, there is no thrust contribution to the debris motion. In addition, the propagation of debris accounts for the atmospheric drag effect. This is done because the atmospheric drag may have a noticeable effect on the debris motion when the debris are propagated over long periods of time. Furthermore, unlike the chaser, the pieces of debris are under no form of control and the drag effects cannot be actively mitigated. The perturbations due to atmospheric drag are broken down into radial, tangential, and normal components as follows

[134]:

$$\mathbf{\Delta}_D = (\Delta_{D_r}, \Delta_{D_\theta}, \Delta_{D_h}) \tag{2.31}$$

where

$$\Delta_{D_r} = -\frac{1}{2}\rho S C_D \nu \nu_r \tag{2.32}$$

$$\Delta_{D_\theta} = -\frac{1}{2}\rho S C_D \nu \nu_\theta \tag{2.33}$$

$$\Delta_{D_h} = 0 \tag{2.34}$$

and ρ is the atmospheric density, S is the aerodynamic reference area, C_D is the drag coefficient, and ν is the velocity magnitude. The latter can be computed from equinoctial elements as follows:

$$\nu_r = \sqrt{\frac{\mu}{p}}(f\sin L - g\cos L) \tag{2.35}$$

$$\nu_\theta = \sqrt{\frac{\mu}{p}}(1 + f\cos L + g\sin L) \tag{2.36}$$

$$\nu = \sqrt{\nu_r^2 + \nu_\theta^2} \tag{2.37}$$

The atmospheric density is difficult to predict, and existing models will be used to generate estimates for future missions [135, 136, 137]. For the purpose of this research, the D-SPOSE tool [138], described in further detail in Section 2.3.2, is used to propagate the debris. Other perturbations affecting the debris during re-entry (for analysis in Chapter 4) are also described in Section 2.3.2.

2.2.3 Low-thrust Orbital Transfer Accessibility Using Equinoctial Elements

Presented in this section is a control theoretic analysis of low thrust orbital transfers using equinoctial elements. This work is carried out to support the notion that a specific destination of an orbital transfer is accessible from a given initial condition, and therefore avoid carrying out optimization procedures in vain. The analysis is based on the equations of mo-

tion presented in the beginning of Section 2.2. This work builds on that presented by Gurfil in [139], where accessibility, a weaker notion of controllability, is proven for low-thrust orbital transfers using classical osculating orbital elements.

For the purpose of this analysis, the equinoctial orbital elements are combined into:

$$\boldsymbol{\alpha} = [p, f, g, h, k, L] \in \mathcal{O} \times \mathbb{S}^4 \tag{2.38}$$

where each element in $\boldsymbol{\alpha}$ is defined as in Section 2.1.2, $\mathcal{O} \subset \mathbb{R}^2$ is an open set in $\mathbb{R}^2$, and $\mathbb{S}^4$ is the 4-sphere. As such, the dynamics defined in Sections 2.2 and 2.2.1 can be written as

$$\dot{\boldsymbol{\alpha}} = \mathbf{g}_0(\boldsymbol{\alpha}) + \mathbf{G}(\boldsymbol{\alpha})\mathbf{u} \tag{2.39}$$

where

$$\mathbf{g}_0(\boldsymbol{\alpha}) = \left[0, 0, 0, 0, 0, \frac{q^2\sqrt{p\mu_e}}{p^2}\right] \tag{2.40}$$

and

$$\mathbf{G}(\boldsymbol{\alpha}) = \begin{bmatrix} 0 & \frac{2p\sqrt{\frac{p}{\mu_e}}}{q} & 0 \\ \sqrt{\frac{p}{\mu_e}}\sin L & \frac{\sqrt{\frac{p}{\mu_e}}(f+(1+q)\cos L)}{q} & -\frac{g\sqrt{\frac{p}{\mu_e}}(-k\cos L+h\mathrm{Sin}[L])}{q} \\ -\sqrt{\frac{p}{\mu_e}}\cos L & \frac{\sqrt{\frac{p}{\mu_e}}(g+(1+q)\sin L)}{q} & \frac{f\sqrt{\frac{p}{\mu_e}}(-k\cos L+h\sin L)}{q} \\ 0 & 0 & \frac{s^2\sqrt{\frac{p}{\mu_e}}\cos L}{2q} \\ 0 & 0 & \frac{s^2\sqrt{\frac{p}{\mu_e}}\sin L}{2q} \\ 0 & 0 & \sqrt{\frac{p}{\mu_e}}(-k\cos L + h\sin L) \end{bmatrix} \tag{2.41}$$

In the above, q and s are defined as in Eq. (2.15). It is worth noting that the boundary conditions for a given orbital transfer defined using these dynamics can be specified in terms of an initial state $\boldsymbol{\alpha}_0$ and a desired state $\boldsymbol{\alpha}_f$.

To provide sufficient conditions for accessibility, the concept of Lie brackets is used. The Lie bracket is a binary operation, which associates to a pair of vector fields $\mathbf{g}_0$ and $\mathbf{g}_1$, the vector field

$$[\mathbf{g}_0, \mathbf{g}_1] = D\mathbf{g}_1 \cdot \mathbf{g}_0 - D\mathbf{g}_0 \cdot \mathbf{g}_1 \tag{2.42}$$

where $D\mathbf{g}_i$ represents the Jacobian matrix of $\mathbf{g}_i$.

For the sake of analysing low thrust orbital transfers, the accessibility rank condition for this problem is defined as any system in the class defined by Eq. (2.39) that is accessible from $\boldsymbol{\alpha}_0$ if the reachable set $\boldsymbol{\alpha}_f$ contains an open subset of $\mathbb{R}^2$. For the purpose of showing that the system is accessible, let

$$\mathbf{G}(\boldsymbol{\alpha}) = [\mathbf{g}_1(\boldsymbol{\alpha}), \mathbf{g}_2(\boldsymbol{\alpha}), \mathbf{g}_3(\boldsymbol{\alpha})] \tag{2.43}$$

Then, to show the accessibility rank condition holds, six Lie brackets that are linearly independent for any initial orbit $\boldsymbol{\alpha}_0$ must be found. These Lie brackets are defined in Λ as follows

$$\Lambda = ([\mathbf{g}_0, \mathbf{g}_1], [\mathbf{g}_0, [\mathbf{g}_0, \mathbf{g}_1]], [\mathbf{g}_0, \mathbf{g}_2], [\mathbf{g}_0, [\mathbf{g}_0, \mathbf{g}_2]], [\mathbf{g}_0, \mathbf{g}_3], [\mathbf{g}_0, [\mathbf{g}_0, \mathbf{g}_3]]) \tag{2.44}$$

Thus, accessibility is not possible for the cases for which Λ drops rank and as such these cases must be found. To do this, the equation $det\Lambda = 0$ is examined and simplified using the symbolic algebra functionality of the software Wolfram Mathematica [140] to give

$$\begin{aligned} det\Lambda = \mu_e\sqrt{p\mu_e}\left(1 + h^2 + k^2\right)\left(1 + f\cos L + g\sin L\right) \\ \left(-5f^2 - 5g^2 - 6f\cos L + 3\left(f^2 - g^2\right)\cos 2L - 6g\sin L + 6fg\sin 2L\right) = 0 \end{aligned} \tag{2.45}$$

The obvious solutions to this equation are

$$p = 0 \tag{2.46}$$

$$h^2 + k^2 = -1 \tag{2.47}$$

For solution (2.46) $p = a(1 - e^2) = 0$, there is a lower constraint on a defined by the radius of Earth and p will therefore only be zero if $e = 1$, i.e., when the target orbit is parabolic. This will not be the case for any chaser transfers to space debris orbiting Earth. Furthermore, by definition $h, k \in \mathbb{R}^2$ which rules out the solution to Eq. (2.47) as a possibility as well.

To find the other real solutions to Eq. (2.45), the classical orbital elements are substi-

tuted into the equations

$$1 + f \cos L + g \sin L = 0 \tag{2.48}$$

and

$$-5f^2 - 5g^2 - 6f \cos L + 3 \left(f^2 - g^2 \right) \cos 2L - 6g \sin L + 6fg \sin 2L = 0 \tag{2.49}$$

using Eqs. (2.1-2.6); this yields the solutions presented in Table 2.2, found using Wolfram Mathematica [140].

e	θ (rad)
1	π
0	$\frac{\pi}{2}$
0	$\frac{3\pi}{2}$
1	$2 \arctan \left(\sqrt{(\frac{1}{2}(7 + \sqrt{57}))} \right)$
1	$2\pi - 2 \arctan \left(\sqrt{\frac{1}{2}(7 + \sqrt{57})} \right)$
$\frac{6 \cos(\theta)}{-5 + 3 \cos(2\theta)}$	$\forall \frac{\pi}{2} \leqslant \theta \leqslant 2 \arctan \left(\sqrt{(\frac{1}{2}(7 + \sqrt{57}))} \right) \ \vee$
	$2\pi - 2 \arctan \left(\sqrt{\frac{1}{2}(7 + \sqrt{57})} \right) \leqslant \theta \leqslant \frac{3\pi}{2}$

Table 2.2: Solutions to Eqs. (2.48) and (2.49)

There are two distinct types of solutions in Table 2.2: the first type requires the target orbit to be parabolic ($e = 1$) which will not be the case for any chaser transfers to space debris orbiting Earth. The second type is for a constant true anomaly θ, i.e. a specific true anomaly for a specified eccentricity, a scenario which is unlikely and easily avoidable. These results imply that there exist continuous-time control inputs that steer the spacecraft from any initial orbit to almost all desired target orbits.

2.3   Software Tools Used in this Thesis

The software described in this section are those specialized beyond other standard tools employed in this thesis, such as Matlab, Mathematica, and Excel. These specialized software

include: GPOPS-II used for solving minimum-time low-thrust optimal control problems associated with orbital transfers, D-SPOSE used for satellite and debris position and attitude propagation, and DRAMA and DAS both used for debris re-entry and risk analysis. In the following, we present a high level brief introduction to these tools, citing references which the reader can consult for additional details.

2.3.1 GPOPS-II

The minimum-time low-thrust optimal control problem analyzed in Chapter 3 of this thesis is solved using the optimal control software GPOPS-II [4]. GPOPS-II is a MATLAB software that transcribes an optimal control problem to a nonlinear programming problem (NLP) on a given mesh. In order to do this, GPOPS-II implements the variable-order Legendre–Gauss–Radau (LGR) quadrature collocation method [141], together with an hp-adaptive mesh refinement method [142]. In broad terms, the collocation method discretizes the domain (in our case the true longitude L) into a number of collocation points at which the dynamic equations of motion are enforced, using specifically chosen parameters and basis functions. A hp-adaptive method is a hybrid between a p method and an h method in that both the number of mesh intervals (containing collocation points) and the degree of the approximating basis function within each mesh interval can be varied. The NLP arising from the LGR collocation method is solved using the open-source NLP solver IPOPT (interior point optimizer) [143], which implements a primal-dual interior point method [144]. Analytical first and second derivatives are obtained using the open-source algorithmic differentiation package ADiGator, for which the underlying algorithm is described in [145]. Then, the boundary conditions, constraints, and path errors of the optimal control problem are estimated and checked against the desired error tolerances. If the tolerances are satisfied, a solution is found and the problem is solved; if not, a new mesh is determined and the unsatisfactory solution is used as the initial guess.

2.3.2 Debris SPin/Orbit Simulation Environment (D-SPOSE)

For the purpose of this research, the open source software Debris SPin/Orbit Simulation Environment (D-SPOSE) [146] is used as a coupled position-attitude propagator. D-SPOSE was originally developed by former Ph.D. candidate in the McGill Aerospace Mechatronics

2.3 Software Tools Used in this Thesis

Lab Luc Sagnières, to study the long-term evolution of the attitude dynamics of large space debris. Containing the major torques that affect the attitude dynamics of spacecraft in orbit, D-SPOSE enables accurate analyses and predictions of the rotational motion of a piece of debris and a high fidelity coupled orbit-attitude propagation [138]. In order to validate the results generated by D-SPOSE, the simulated propagations have been compared to observations of satellites. As such, D-SPOSE has been applied to three passive spacecraft that have been continuously tracked by the International Laser Ranging Service (ILRS) since launch: the American and Italian Laser Geodynamics Satellite 2 (LAGEOS-2) and Laser Relativity Satellite (LARES), and the Japanese Ajisai satellite [138]. Furthermore, D-SPOSE propagations have been compared to observations of Envisat [147] and Topex/Poseidon [148]. A detailed description of the relevant perturbations and their implementation can be found in [138].

D-SPOSE is employed as part of the solution procedure for the majority of work presented in this thesis. In Chapters 3 and 4, D-SPOSE is specifically employed to propagate and predict debris locations during low-thrust rendezvous as well as to predict the position and orientation of the debris as it descends from the initial release orbit to the re-entry orbit at ∼125 km altitude. At altitudes lower than 125 km, the atmospheric conditions become more difficult to predict which makes further propagation less accurate. D-SPOSE is also employed as a means of estimating the altitude decay rate of debris as well as the RAAN drift rate at a given altitude. In Chapter 5, the attitude propagation element of D-SPOSE is combined with the orbital propagation of a re-entry analysis tool DRAMA (presented in Section 2.3.3 to investigate the effects of the rotational dynamics of space debris during re-entry.

The perturbations affecting debris propagation considered by D-SPOSE can be split into two categories, namely gravitational and non-gravitational perturbations. In terms of gravitational perturbations, Earth's gravitational field, gravity-gradient torque, and third-body interactions are included. The effect of Earth's gravitational field is considered up to the degree and order specified by the user including oblateness, sectoral, and tesseral terms. The gravity-gradient torque, is computed for a general gravitational field from the spherical-harmonic expansion of the geopotential, with the simplifying assumption that the gravitational acceleration in the vicinity of the center of mass varies linearly with distance.

The geopotential model used by D-SPOSE is EGM2008 [5]. Finally, the effect on the orbital dynamics of Earth satellites of third-body accelerations caused by the Moon and the Sun are included and calculated based on the gravitational parameter and position of said bodies. The positions of the Sun and the Moon are obtained by D-SPOSE from planetary ephemerides provided by the Virtual Observatory of the Institut de Mécanique Céleste et de Calcul des Éphémérides [149].

Non-gravitational perturbations taken into account in D-SPOSE include aerodynamic drag and torque, eddy-current torque, radiation perturbations, and internal energy dissipation. The effect of aerodynamic drag diminishes at higher orbits due to the atmospheric density's exponential decrease and its computation was already explained in Section 2.2.2. The NRLMSISE-00 model [136] is implemented to generate values of atmospheric density and wind velocity vectors at the debris position. The force arising from the atmosphere will cause a torque which depends on the geometry of the satellite surface exposed to the incoming flow. The aerodynamic torque for a spinning spacecraft is calculated by computing the surface integral over the area of a surface and summing over all the exposed surfaces. The eddy-current torque is defined as the interaction between the spinning satellite's conductive surfaces and the Earth's magnetic field. For slowly spinning spacecraft, the time variation of the magnetic field as seen by the orbiting spacecraft is also considered. The radiation perturbations considered arise from the pressure that an incoming flux of photons exert on satellite surfaces, causing both acceleration and torque. Sources of radiation include the Sun and Earth's Albedo and infrared emissions. Internal energy dissipation is considered due to the fact that no physical body is truly rigid and damping can arise in a satellite from multiple sources, including the sloshing of fuel, vibrations, or moving appendages. Within D-SPOSE, the torque arising as a result of internal energy dissipation is modelled using a Kane damper. This mechanism consists of a spherical mass contained inside a cavity full of viscous fluid at the spacecraft's center of mass. Assuming that the centers of mass of the spacecraft and the damper remain coincident, a torque proportional to their relative angular velocity will arise.

For the purpose of generating the results presented in Chapters 4 and 5, D-SPOSE requires a triangulated representation of debris geometry, and the following perturbations are included: Earth's gravitational effects up to degree and order 4 (including sectoral and

tesseral terms) as well as third body gravitational effects caused by the Sun and the Moon, the aerodynamic effects (drag and torque), and the internal energy dissipation torque. Solar radiation pressure and eddy-current torques are not modelled.

2.3.3 Software for Re-Entry Analysis

Given that the atmospheric re-entry of large space debris poses a threat due to the risk of impacting populated areas, some means of quantifying this risk are necessary such that mitigation measures can be implemented. As such, the two debris risk analysis softwares, DRAMA (developed by ESA) [150, 151] and DAS (developed by NASA) [152], are used as part of this research to calculate the casualty risk factor for different re-entry scenarios to determine which aspects of the ADR mission can be designed to minimize said risk.

The first of the two software suites used for re-entry analysis is the ESA software package DRAMA [150], and more specifically the SARA tool within DRAMA. The SARA tool employs two components, namely SESAM (Spacecraft Entry Survival Analysis Module) for re-entry and break-up estimation, and SERAM (Spacecraft Entry Risk Analysis Module) for casualty risk analysis. The DRAMA version employed in this work is DRAMA3.0.3 [153]. The second software suite, DAS, is a NASA software that provides lower fidelity analysis, in terms of risk assessment, than SARA. The DAS version used for the results in this paper is DAS3.0.1 [154]. The two software suites are described in further detail in Section 5.1 along with a comparison of the results from each software, for a given test case.

3

Motion Planning for Multiple Debris Removal

In this chapter, we address the first main contribution of this thesis: development of a so-lution for the motion planning problem for de-orbiting multiple debris. The key difference between considering ADR for one piece of debris and for multiple pieces of debris is the increased number of orbital transfers required for multiple debris removal. Consequently, solving the motion planning problem for removing multiple pieces of debris is vital and is therefore the first step towards designing a multiple debris removal mission. In Section 3.1, the motion planning problem is formulated followed by the analysis of other key features unique to multiple debris removal presented in Section 3.2. Different methods for solving the motion planning problem are presented in Sections 3.3, 3.4, and 3.6 as well as a fuel mass analysis, presented in Section 3.5.

3.1 Problem Definition

Multi-debris missions can be broadly categorised as those where a mothership travels from one piece of debris to the next, deploying smaller thruster modules which attach to and de-orbit the debris [118, 155] to a disposal orbit, as depicted in Figure 3.1. In this scenario the chaser starts in its initial orbit and is transferred to the first piece of debris, after which the chaser travels to each consecutive debris directly, without returning to the initial orbit. The other category involves a chaser de-orbiting the targeted piece of debris to a disposal

orbit and then returning to another debris orbit in order to de-orbit the next piece of debris in a sequential or recursive fashion, as depicted in Figure 3.2. Here the chaser spacecraft starts in its initial orbit, otherwise referred to as the disposal orbit for consecutive debris, to which it will return once a piece of debris has been captured. The majority of research carried out on multiple debris removal missions has assumed mission scenarios in the first category [156, 157]; however, this approach is not well suited for capture methods resulting in a tethered connection between the chaser and the debris, such as the tethered-net capture methods [158] or harpoon capture [81]. In these scenarios, stabilizing the debris and attaching a de-orbiting device is cumbersome and inefficient. Capture methods that result in a tethered connection between the chaser and the debris, as those mentioned, are among the most researched [41] and tested methods for ADR. For example, recent experiments for the RemoveDebris initiative [159] have demonstrated capturing an object using a net and a harpoon in space.

As such, the work presented here focuses on using optimized orbital transfers as a novel approach to achieving multiple debris removal in a recursive fashion. Moreover, previous studies show that for ADR to be successful, at least five pieces of debris are required to be removed within one year [26, 98]. In this chapter, three problem formulations are outlined. The first two formulations represent lower fidelity approaches. First, in Section 3.3 continuous thrust transfers are defined using Edelbaum's methodology [1] to estimate the mission time and fuel cost given the recursive approach in Figure 3.2. Edelbaum's methodology is employed as low-continuous thrust engines are assumed for this type of mission given the likelihood for high ΔV costs. The application of Edelbaum's formulation to continuous low thrust transfers is not a novel approach; however, it is employed as an initial, low fidelity option for analysing the orbital transfers needed to achieve a multiple debris removal mission. Furthermore, this approach is used to generate initial guesses of transfer times used for the higher fidelity analysis outlined in Sections 3.2.2 and 3.6 and as a comparative case for more complex numerically optimized solutions presented in Chapter 4. Second, as a comparative measure to the recursive scenario, a methodology for estimating the time and ΔV cost of transferring the chaser directly from debris to debris is presented in Section 3.4, as would be the case in the mothership approach for debris de-orbiting. A formulation of Lambert's Theorem based on [2] is used in order to find low ΔV cost

transfer orbits between the debris. Again, this approach is well established for optimized impulsive transfers; however, it allows us to make a comparison between multiple debris removal mission employing a mothership approach to one which makes use of the recursive approach. The third problem formulation involves the minimum-time low-thrust optimal control problem which represents a higher fidelity approach to optimizing orbital transfers specifically suited for recursive debris removal missions. This approach is outlined in Section 3.6 and represents a novel approach to designing and planning multiple space debris removal missions given a recursive strategy.
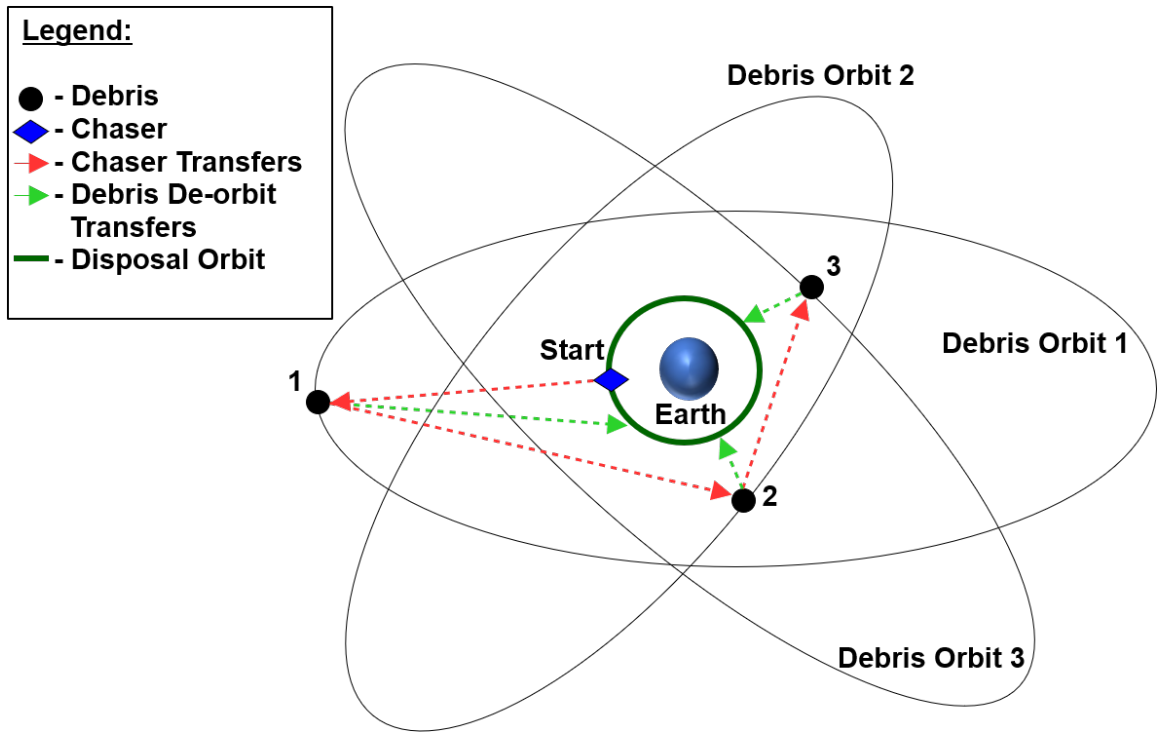
Figure 3.1: Mothership multiple debris removal scenario for three debris

3.2   Unique Aspects of Multiple Debris Removal

In addition to the challenges associated with active debris removal missions designed to remove only one piece of debris, multiple debris removal missions need additional consideration in terms of debris selection and sequencing and fuel and time cost. Consequently, presented in this section are the approaches taken towards selecting appropriate debris,
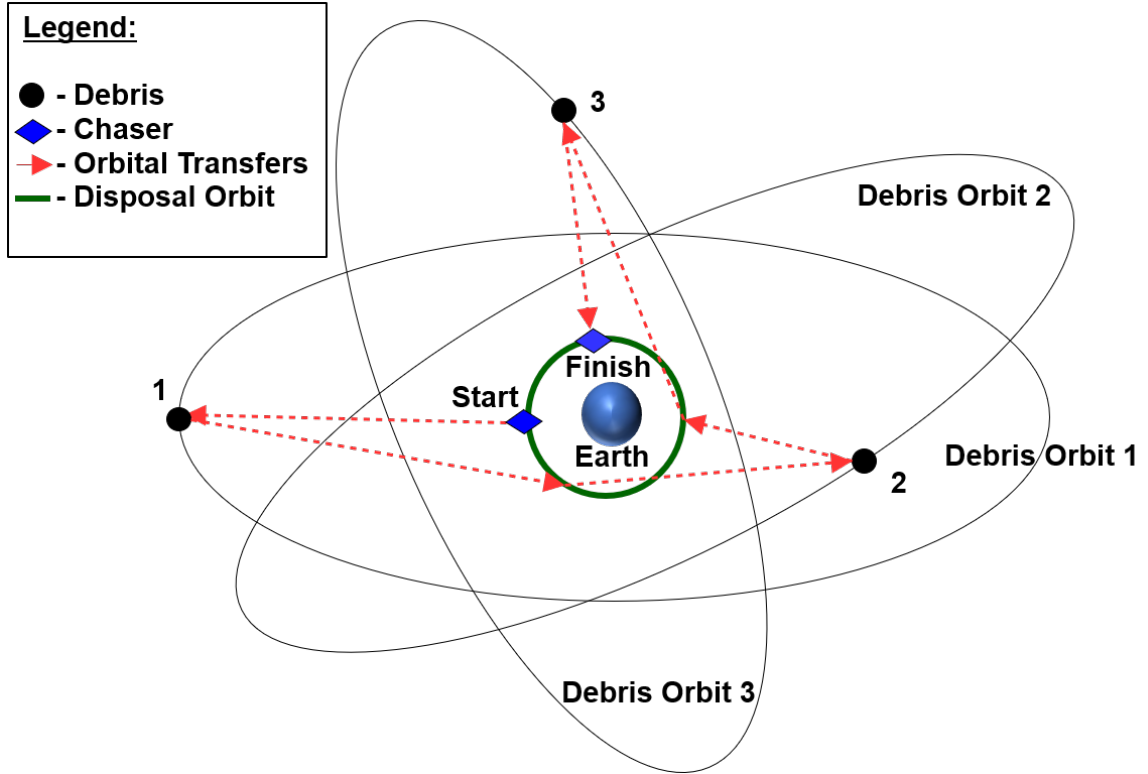
Figure 3.2: Recursive multiple debris removal scenario for three debris

finding an optimized sequence in which to remove the debris to minimize the time taken and the fuel costs of the mission, and introducing drift orbits in certain rendezvous phases. Drift orbits are specifically selected orbits, in which the chaser spacecraft is parked, where the natural changes in RAAN due to gravitational perturbations result in the RAAN of the chaser "drifting", ideally to match that of the debris. These drift orbits allow for a trade-off between spending fuel to change the RAAN and spending time to let the RAAN of the chaser drift naturally towards that of the debris.

3.2.1 Debris Selection and Sequencing

Two approaches to selecting debris in LEO have been chosen based on [98] and [155] respectively. In [98] the debris are singled out due to their high risk factor, which takes into account a combination of the orbital parameters, mass, and likelihood of fragmentation. The debris in [155] are chosen based on similar criteria to [98], however, with the added

consideration that the inclination of each debris does not differ from the others in the set by more than $2°$.

Consequently, the first group of debris considered are the "highest" priority targets, i.e., with the highest risk factors according to the aforementioned taxonomy. These debris are in the inclination range $\sim 99°$ as this is considered to be the most critical region due to it containing sun synchronous orbits. The second, and primary, group of debris of interest for this research are large rocket bodies from SL-8 rockets with semi-major axes ranging between 7100-7400 km, of which there are 289 pieces with masses around 1440 kg currently being tracked. This represents a large proportion of space debris mass, as well as debris with high risk factors, due to the orbits in which the pieces of debris are located. The orbits are near-circular and have inclinations between $70°$ and $83°$.

As the pool of SL-8 rocket bodies in similar inclination and altitude bands is large, there is significant freedom with respect to selecting the particular pieces of debris for the ADR mission. Individual pieces of debris can be chosen based on further selection criteria, such as risk factor [98] or the inclination bands in which they are located [155] in order to minimize the costs of transfers to the debris orbits. The specific orbital elements of each piece of debris considered are detailed for each case study in Chapter 4.

For the sets of SL-8 rocket bodies employed to illustrate the multi-debris removal missions in Chapter 4, the individual pieces of debris are selected and sequenced based on the achievable RAAN change of the chaser within a given transfer. This procedure and the RAAN envelope to which the chaser can be transferred are detailed in Section 3.2.2. This envelope is relevant both when choosing and sequencing the pieces of debris: each consecutive debris within the multiple debris removal mission needs to be chosen such that after propagation, the RAAN of the piece of debris falls within the achievable envelope of the chaser transfer. It is also important to note, when selecting and sequencing debris for a given mission, that the debris is in motion as the mission is carried out. This means, each debris needs to be propagated over the time taken to remove the previous pieces of debris in the given mission. Hence, considerations for debris selection and sequencing, based on debris initial conditions, need to be made based on the debris parameters after the time taken to de-orbit previous debris.

3.2.2 RAAN Limitations

As alluded to above, apart from fuel and time limitations, special considerations are required in terms of RAAN changes that can be achieved, given the required altitude and inclination changes for the transfer. First, the RAAN limitations as described in this section primarily apply to low-thrust transfers; however, RAAN drift orbits, as defined later in this section, can be included in the impulsive transfer process to achieve certain, otherwise high fuel cost, RAAN changes in the context of the mothership approach. Second, natural RAAN changes caused by Earth oblateness are inevitable and therefore contribute to the overall RAAN changes during transfers and propagations. Third, there is a limit on the RAAN change that can be provided by the chaser thrusters within a given altitude and/or inclination change.

In light of the aforementioned considerations, there is not only a maximum RAAN change for a given transfer or propagation, but also a minimum, so that the resulting RAAN change envelope is specified by:

$$\Delta\Omega_{envelope} = \Delta\Omega_{pertub} \pm \Delta\Omega_{thrust} \tag{3.1}$$

In the above, the rate of change of RAAN due to Earth oblateness is given by:

$$\dot{\Omega}_{perturb}(t) = -\frac{3}{2}J_2\sqrt{\mu_e}R_e^2 a(t)^{\frac{-7}{2}}\cos i(t) \tag{3.2}$$

where J_2 is the zonal harmonic coefficient specified in Table 2.1, R_e is the radius of Earth, and μ_e is Earth's gravitational constant also specified in Table 2.1. In Eq. (3.2), the dependency on eccentricity is not included as all orbits considered are near circular which makes the eccentricity contribution to the RAAN drift calculation negligible. In addition, the $\Delta\Omega_{thrust}$ can be estimated by assuming a constant thrust direction in the body-fixed frame of the chaser throughout the orbital transfer. The optimal heading angle (as illustrated in Figure 2.5) for changes in certain orbital parameters can be found analytically [160]. The out-of-plane thrust acceleration Δ_{T_h} (from Eq. (2.29)) can be described in terms

of the heading angle χ as follows:

$$\Delta_{T_h} = \frac{T}{m} u_h = \frac{T}{m} \sin \chi \qquad (3.3)$$

and the rate of change of RAAN due to thrust is given by:

$$\dot{\Omega}_{thrust}(t) = \frac{a \sin \theta}{H \sin i} m \Delta_{T_h} \qquad (3.4)$$

where $H = \sqrt{\mu p}$ is the magnitude of the angular momentum vector of the orbit, and θ is the true anomaly of the spacecraft.

Eq. (3.4) represents the general equation for RAAN change for a given thrust component Δ_{T_h}. It is possible to prescribe an optimum heading angle for achieving the highest rate of change in a specific orbital parameter. For example, to achieve a maximum rate of change in RAAN, $\chi = \text{sign}(\sin \theta) \frac{\pi}{2}$; however, this results in no change in altitude. Alternatively, $\chi = 0$ results in the highest rate of change in altitude, but no change in RAAN. For the purpose of narrowing the target selection in this thesis, a constant heading angle of $\chi = \text{sign}(\sin \theta) \frac{\pi}{4}$ is chosen to allow for changes in both altitude and RAAN, in order to gain insight into the achievable RAAN changes. This RAAN analysis is carried out prior to optimizing the thrust direction components for a given transfer to gauge the attainability of the RAAN change given the altitude change, inclination change, and the magnitude of thrust. Thus, the $\Delta\Omega_{envelope}$ for a given transfer can be estimated by integrating Eqs. (3.2) and (3.4), where the time of transfer is estimated using Edelbaum's low-thrust transfer analysis outlined in Section 3.3.

As mentioned in Section 3.2.1, the achievable RAAN change as quantified by the RAAN envelope introduced in this section is used to select and sequence the pieces of debris for the multiple debris removal mission. The RAAN envelope $\Delta\Omega_{envelope}$, indicates the region of achievable RAANs to which the chaser can transfer, for a given altitude and inclination change. As a result, available pieces of debris within the selection pool are propagated over the time taken to remove previous pieces of debris within the mission, as well as the estimated transfer time for the chaser to reach the altitude and inclination for a given piece of debris. A potential debris target that falls within the chaser RAAN envelope can then be identified. It should be noted that the semi-major axis and inclination of the

Figure 3.3: Rendezvous transfer with drift orbit

debris may change significantly during propagation, resulting in a re-estimate of the chaser transfer time and therefore a re-propagation, making this process iterative.

3.3 Continuous Thrust Transfers Using Edelbaum's Formulation

In this section, a mission plan for removing multiple pieces of large space debris, using a recursive approach is formulated. For each transfer, a modified Edelbaum methodology is used to account for the changes in semi-major axis and inclination and, perturbations introduced by the first order effects of the flattening of the Earth are considered (J_2 effect) in order to use the natural RAAN drift to alter the RAAN of the chaser orbit to match that of the orbit of the debris target.

3.3.1 Evaluating Mission Costs

When applying Edelbaum's methodology [1] to the recursive approach, two orbital transfers are considered (for cases where no drift orbit is required). The first is the rendezvous where the chaser is transferred from its original orbit (or the disposal orbit) to the orbit of

the first/next debris. During this stage the altitude, inclination, and RAAN of the chaser are changed in order to match the orbital characteristics of the debris. Once the debris is captured and stabilized the chaser-debris system will transfer to the disposal orbit in the de-orbiting stage. During de-orbiting, only the altitude is changed by the chaser, however, changes in RAAN due to the RAAN drift are also accounted for in the analysis. It is also important to note that t_0, i.e., when $t = 0$ is the point at which a given transfer, at any stage of the mission, is initiated.

Rendezvous

Edelbaum transfer [1] is employed as low-continuous thrust engines are assumed for this type of mission given the likelihood for high ΔV costs. Equations from Edelbaum [1] stated in Eqs. (3.6), (3.7), and (3.9) are used to estimate the time required for a given low-thrust transfer as well as the ΔV cost, where τ is the thrust acceleration of the engine:

$$\tau = \frac{T}{m} \tag{3.5}$$

where recall, T is the thrust of the chaser and m is mass of the chaser or chaser-debris system during the de-orbit stage.

For the analysis in this section, the debris orbits are approximated as circular since for a significant number of large space debris in LEO the eccentricities are very small ($\leqslant 0.001$). This assumption can be removed when all changes in the orbital elements (not only altitude, inclination, and RAAN) are accounted for during transfers, as will be done in Section 3.6.

Considering these assumptions, the ΔV cost (subscripts a and i refer to the cost of changing the semi-major axis and the inclination respectively) can be found for a transfer of the chaser from the initial orbit to the target debris orbit using the following equations [1]:

$$\Delta V_{a,i} = v_C \cos(\chi_0) - \frac{v_C \sin(\chi_0)}{\tan(\frac{\pi}{2}\Delta i + \chi_0)} \tag{3.6}$$

where the initial heading angle χ_0 of the chaser is:

$$\tan \chi_0 = \frac{\sin(\frac{\pi}{2}\Delta i)}{\frac{v_C}{v_D} - \cos(\frac{\pi}{2}\Delta i)} \tag{3.7}$$

and the in-orbit circular velocity of the chaser (subscript C) and debris (subscript D) orbits are:

$$v_n = \sqrt{\mu/a_n}, \quad n = C, D \tag{3.8}$$

where a_C and a_D are the initial and final radii from the center of the Earth of each orbit, μ is the Earth's gravitational constant. Then, the thrust duration required to achieve this transfer is given by:

$$t_{tr} = \frac{\Delta V_{a,i}}{\tau} \tag{3.9}$$

De-Orbit

Once the rendezvous and capture phases have been completed, the debris needs to be de-orbited. The procedure for this is similar to the no-drift rendezvous phase except the mass of the system is now given by the chaser mass plus the mass of the debris and only changes in semi-major axis are taken into account for the ΔV_{Do} and time t_{Do} calculations as no changes in i or RAAN are required.

It should be noted that changes in RAAN and inclination are carried out during the rendezvous phase rather than the de-orbit phase for reasons of simplicity and efficiency. During the rendezvous phase, it is only the chaser which needs to perform the manoeuvres for the required changes, whereas if these changes were carried out during the de-orbit phase, they would involve the tethered chaser-debris system which would be more complicated and less cost effective.

3.3.2   Including RAAN Drift

The RAAN drift and the J_2 effect, both on the chaser and the debris, can be included in the Edelbaum analysis. RAAN drift applies to the chaser during long (non-impulsive) transfers, as well as to the debris as it is orbiting the Earth. Therefore, the relative RAAN drift between the chaser and the debris needs to be considered at all stages of the mission.

The chaser drift during the rendezvous and de-orbit transfers can be found by integrating the first-order ODE for the RAAN as given by Eq. (3.2) over the time of transfer found using Eq. (3.9). Eq. (3.2) must be integrated jointly with the rates of change of altitude $\dot{a}$

and inclination $\dot{i}$ of the chaser given by Eqs. (3.10) and (3.11), respectively:

$$\dot{a}_C(t) = \frac{2a_C(t)\tau}{v_C(t)} \tag{3.10}$$

$$\dot{i}_C(t) = \frac{2\tau}{\pi v_C(t)} \sin(\chi(t)) \tag{3.11}$$

where

$$v_C(t) = \sqrt{v_C(0)^2 - 2v_C\tau t \cos(\chi_0) + (\tau t)^2} \tag{3.12}$$

The thrust heading direction χ during the transfer can be found using Eq. (3.13), given the initial heading angle χ_0 found using Eq. (3.7).

$$\tan(\chi(t)) = \frac{v_C(0)\sin(\chi_0)}{v_C(0)\cos(\chi_0) - \tau t} \tag{3.13}$$

The RAAN drift of the debris within its orbit is found using Eq. (3.2), however, with a and i constant which yields a constant RAAN rate. Now, if a drift orbit (introduced in Section 3.2.2) is required for rendezvous, the RAAN drift of the chaser when parked in a drift orbit is calculated in the same way as that of the debris within its orbit. As a result, Eq. (3.14) gives the RAAN after a certain time t spent by the chaser or debris in a given orbit.

$$\Omega(t) = \Omega_0 + \dot{\Omega}(t - t_0) \tag{3.14}$$

where $\Omega(t)$ refers to the RAAN at the mission time t and Ω_0 is the initial RAAN of debris or chaser in the drift orbit.

The ΔV cost of changing the RAAN (from that of the chaser orbit to that of the debris orbit) using low continuous thrust can be found using Eq. (3.15) as derived by Pollard [161].

$$\Delta V_\Omega = \frac{\pi}{2}\sqrt{\frac{\mu}{a_D}}|\Delta\Omega|\sin(i_D) \tag{3.15}$$

where $\Delta\Omega$ is the difference between the desired RAAN and the RAAN of the chaser after the effect of RAAN drift during transfer. Consequently, the total ΔV cost for these transfers is calculated as the sum of $\Delta V_{a,i}$ and ΔV_Ω, bearing in mind that introducing a drift orbit would reduce or even remove the contribution of ΔV_Ω.

3.3.3 Solving the Multiple Debris Removal Motion Planning Problem Using Edelbaum's Formulation

The solution to the multiple debris removal problem using Edelbaum's formulation [1] is defined as a novel optimization procedure. The aim of this optimization procedure is to find the drift orbit in which to place the chaser as part of the debris rendezvous stage, such that the mission constraints of removing 5 debris within a total time t_{max} and a total cost ΔV_{max} are satisfied while minimizing the actual total mission time and fuel cost. A flowchart of the entire procedure is shown in Figure 3.4.

The inputs in the procedure are the orbital characteristics of the chaser in its initial orbit, the orbital characteristics of the 5 pieces of debris (pre-selected based on considerations made in Sections 3.2.1 and 3.2.2, the thrust capabilities of the chaser, the mass of chaser and the debris, and an estimate of the cost (time and ΔV) for the de-orbit stage of the mission (no drift orbit). The outcome is then the altitude and inclination of the drift orbit, a_{drift} and i_{drift}, as well as the ΔV and time cost of the debris rendezvous stages of the entire mission.

To start, the debris are sequenced as described previously and the objective function and constraints used in order to find a minimum mission cost are defined as follows

$$
\begin{aligned}
\min_{a_{drift}, i_{drift}} \quad & f\big(a_{drift}, i_{drift}\big) = \frac{\Delta V_{total}}{\Delta V_{max}} + \frac{t_{total}}{t_{max}} \\
\text{subject to} \quad & g_1\big(a_{drift}, i_{drift}\big) = \Delta V_{total} - \Delta V_{max} \leqslant 0 \\
& g_2\big(a_{drift}, i_{drift}\big) = t_{total} - t_{max} \leqslant 0
\end{aligned}
\tag{3.16}
$$

where, ΔV_{total} is the sum of the total transfer ΔV of the rendezvous stage and the de-orbit stage ($\Delta V_R + \Delta V_{Do}$) and t_{total} is the sum of the total transfer time taken to rendezvous and the time taken to de-orbit ($t_R + t_{Do}$), with t_R accounting for the time spent in the drift orbit.

The constraints may cause the mission to be infeasible for some combinations of debris, in which case the best case scenario is found using the objective function in Eq. (3.17)

where the deviation from the desired mission cost is minimized rather than the actual costs.

$$\min_{a_{drift}, i_{drift}} f(a_{drift}, i_{drift}) = \frac{|\Delta V_{max} - \Delta V_{total}|}{\Delta V_{max}} + \frac{|t_{max} - t_{total}|}{t_{max}} \tag{3.17}$$

The optimization procedure, specified by Eq. (3.17), becomes more effective for a given mission when higher changes in RAAN are required for a given rendezvous. It is noted that, the described optimization procedure could also be tailored for the mothership approach, however, it is likely to be less effective since the 'design space' is limited by the relatively small altitude changes between each debris.

3.4 Impulsive Transfers by Applying Lambert's Theorem to Orbital Manoeuvres

In this section a formulation of Lambert's Theorem based on [2] is used in order to find low ΔV cost transfer orbits from debris to debris to calculate the expected costs of the mothership approach. These orbital transfers can each be achieved using separate 2-thrust impulsive transfer manoeuvres as illustrated in Figure 3.5. The results of this analysis are used to compare and contrast with results found using Edelbaum's formulation for a recursive approach and identify scenarios where one approach may be more appropriate in terms of cost efficiency. It is noted that the formulation of Lambert's theorem for impulsive transfers does not take into account perturbing effects as a result of a non-spherical Earth. The approach is included to be comparable to results in the literature [119]; however, considerations can be made to include drift orbits and reduce the fuel cost in exchange for longer transfer time.

First, Lambert's theorem [2] states:

"The transfer time of a body moving between two points on a conic trajectory is a function only of the sum of the distances of the two points from the origin of the force, the linear distance between the points, and the semi-major axis of the conic"
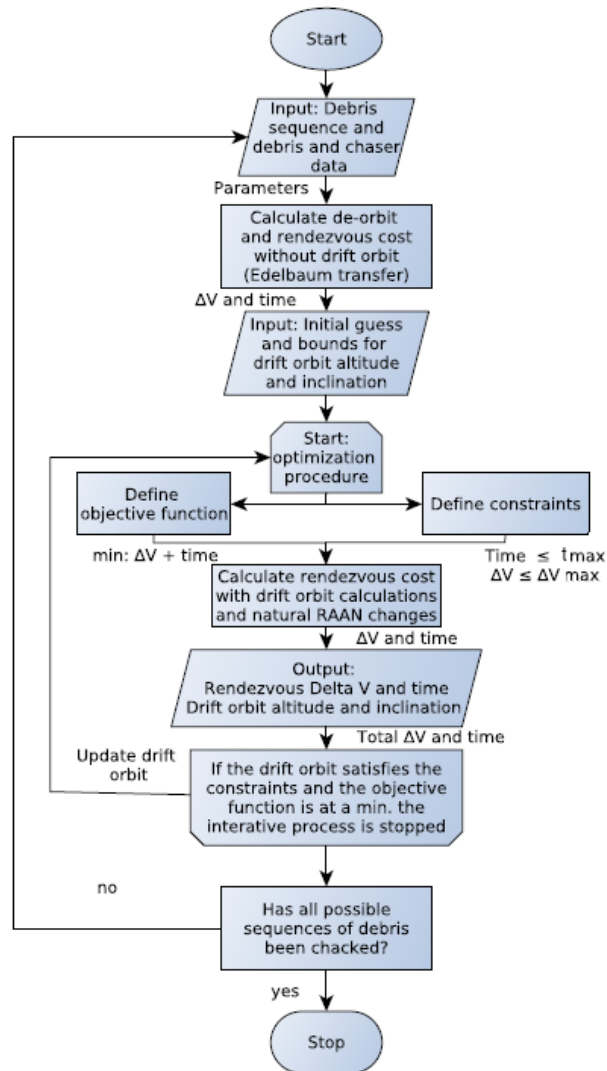
Figure 3.4: Flow chart of procedure for low continuous thrust employing the Edelbaum formulation

3.4 Impulsive Transfers by Applying Lambert's Theorem to Orbital Manoeuvres

To formulate this theorem in the context of an orbital transfer problem, Kepler's equation relates the transfer time between two orbits ($t_D - t_C$) to the semi-major axis (a_{tr}) and the eccentricity of the transfer orbit (e_{tr}) and the eccentric anomaly of the first and second orbits (E_C and E_D):

$$\sqrt{\mu_e}(t_D - t_C) = 2a_{tr}^{3/2}(\frac{1}{2}(E_D - E_C) - e_{tr}\sin(\frac{1}{2}(E_D - E_C))\cos(\frac{1}{2}(E_C + E_D))) \quad (3.18)$$

By defining the angles ψ and σ as:

$$\psi = \frac{1}{2}(E_D - E_C), \quad \cos(\sigma) = e_{tr}\cos(\frac{1}{2}(E_C + E_D)) \quad (3.19)$$

Eq. (3.18) can be rewritten as follows:

$$\sqrt{\mu_e}(t_D - t_C) = 2a_{tr}^{3/2}(\psi - \sin(\psi)\cos(\sigma)) \quad (3.20)$$

In order to achieve a point-to point transfer, Lambert's Theorem [2] relates the transfer time to the semi-major axis of the transfer orbit a_{tr}, the sum of the magnitudes of the position vectors of the chaser and the debris when the transfer is initiated, ($r_1 + r_2$), and magnitude of the chord between the chaser and the debris (c) by writing these geometric quantities in terms of ψ and σ defined as follows:

$$r_1 + r_2 = 2a_{tr}(1 - \cos(\sigma)\cos(\psi)) \quad (3.21)$$

$$c = 2a_{tr}\sin(\psi)\sin(\sigma) \quad (3.22)$$

Equation (3.20) can then be solved for a given transfer time $t_D - t_C$ or for a given transfer trajectory represented by a_{tr}. The transfer time is a function of the geometric parameters shown in Figure 3.5.

Now, both Lagrange and Gauss have developed methods for finding the lowest transfer time for a point-to-point transfer by varying the transfer orbit characteristics [2]. For this analysis, a combination of Lagrange's and Gauss' methods applied to Lambert's theorem are used following the solution in [2], in order to take advantage of the efficiency of Gauss'
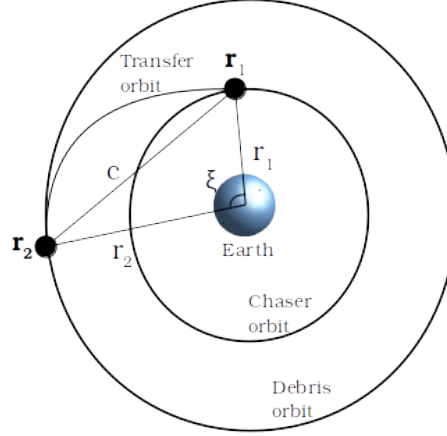
Figure 3.5: Geometric parameters for Lambert's theorem

equation and the robustness of Lagrange's equation. Therefore, Eq. (3.20) is rewritten as:

$$\sqrt{\frac{\mu_e}{a_m^3}}(t_D - t_C) = \kappa^3 H_L + 4\lambda_L \kappa \tag{3.23}$$

where a_m is defined as:

$$a_m = \frac{s}{2} = \frac{1}{4}(r_1 + r_2 + c) \tag{3.24}$$

and λ_L is defined as:

$$\lambda_L = \frac{1}{s}\sqrt{r_1 r_2}\cos\frac{1}{2}\xi \tag{3.25}$$

where ξ is the angle between the position vector of the chaser and the position vector of the debris relative to the focus (in this case the Earth) as shown in Figure 3.5; s is as defined in Eq. (3.24); H_L is a hypergeometric function, introduced in order to take into account hyperbolic transfers as well as parabolic and elliptical transfers. It is defined as:

$$H_L = \frac{4}{3}F(3, 1; \frac{5}{2}; S_1) \tag{3.26}$$

where

$$F(\alpha_L; \beta_L; \gamma_L; z_L) = \sum_{n=0}^{\infty} \frac{(\alpha_L)_n (\beta_L)_n}{(\gamma_L)_n} \frac{z_L^n}{n!} \tag{3.27}$$

57

and $(\alpha_L)_n$ is defined as $\alpha_L(\alpha_L + 1)(\alpha_L + 2)...(\alpha_L + (n-1))$ with $(\alpha_L)_0 = 1$. The variable S_1 is defined as:

$$S_1 = \frac{1}{2}(1 - \lambda_L - x_L\kappa) \tag{3.28}$$

where

$$\kappa = y_L - \lambda_L x_L \tag{3.29}$$

and

$$y_L = \sqrt{1 - \lambda_L^2(1 - x_L^2)} \tag{3.30}$$

The value used for x_L determines the shape of the transfer orbit in the following fashion: if $-1 < x_L < 1$ then it is an elliptic transfer orbit, if $x_L = 1$ it is a parabolic transfer orbit, and if $1 < x_L < \infty$ it is a hyperbolic transfer orbit. The value of x_L can be varied in order to tailor the time, ΔV cost, and accuracy of the rendezvous; this is preferred to varying a_{tr} (defined earlier) which results in numerical problems [2].

Now that a specific transfer orbit has been found, the velocity of the transfer orbit is calculated as follows:

$$\mathbf{v}_{tr} = \frac{1}{\kappa}\sqrt{\frac{\mu_e}{a_m}}[(2\lambda_L\frac{a_m}{r_1} - (\lambda_L + x_L\kappa))\mathbf{n}_{r_1} + \sqrt{\frac{r_2}{r_1}}\sin(\frac{1}{2}\xi)(\mathbf{n}_h \times \mathbf{n}_{r_1})] \tag{3.31}$$

where $\mathbf{n}_{r_1}$ is the unit vector defining the direction of the chaser from the focus and $\mathbf{n}_h$ is the unit vector normal to the orbital plane of the transfer orbit. Finally, the ΔV cost of the transfer of the chaser to the debris is found as:

$$\Delta V_R = \Delta V_1 + \Delta V_2 = |v_C - v_{tr}| + |v_{tr} - v_D| \tag{3.32}$$

with the velocities of the chaser and debris in their respective orbits as computed from the orbital elements and v_{tr}, the magnitude of $\mathbf{v}_{tr}$ of Eq. (3.31).

3.5   Fuel Mass Analysis

The mass of fuel required, given certain thruster specifications, plays an important role in the feasibility of the mission and also provides a good indication of the mission cost. In this section, the equations for estimating the fuel cost both for chemical propulsion and

electric propulsion systems are presented, based on that outlined in [162], followed by how this is specifically applied to electric propulsion systems specific to the Edelbaum analysis, and chemical propulsion systems specific to impulsive transfers analyzed by applying Lambert's theorem. Electric propulsion is a potential and realistic option for achieving low-thrust Edelbaum transfers and hence applies directly to the analysis of fuel costs for this formulation.

The basis of rocket and spacecraft propulsion analysis comes from Tsiolkovsky's rocket equation [163], which describes a vehicle, the mass of which is decreasing as a jet of matter is projected rearwards. The force that projects the exhaust rearwards is the same force that propels the rocket. The thrust-exhaust velocity relationship is based on Newton's second law, as

$$T = \dot{m}_e v_e \tag{3.33}$$

where $\dot{m}_e$ is the mass flow rate, T is the thrust of the rocket, and v_e is the effective exhaust velocity. From Eq. (3.33) Tsiolkovsky obtained the following formula, using simple differential calculus, for the vehicle velocity v:

$$v = v_e \log_e \frac{M_0}{M} \tag{3.34}$$

Here M_0 is the mass of the rocket at ignition, and M is the current mass of the rocket.

3.5.1 Electric Propulsion

Electric propulsion systems make use of electrical power to accelerate a propellant by different possible electrical and/or magnetic means. Electric power can come from a battery, solar panels, or an on-board nuclear or solar generator. The performance of electrical propulsion systems can be considered using the principles of momentum transfer and the rocket equation (Eq. (3.33)). It is worth noting that the total mass of the system includes the mass of the propellant, the mass of the structure, and the mass of the power supply. Also, the exhaust velocity depends on the power delivered, the nature of the propellant, and the way the thrusters transfer momentum to the propellant.

The thrusters have a certain efficiency in converting electric power to thrust, and the

power supply has a certain power-to-mass ratio. Expressing these efficiencies as ν for the thruster efficiency, and η for the power-to-mass ratio, the following relationships apply:

$$v = v_e \log_e R \tag{3.35}$$

with the mass fraction:

$$R = \frac{M_S + M_P + M_E}{M_S + M_E} \tag{3.36}$$

where

$$\eta = \frac{P_E}{M_E}; \quad \nu = \frac{\dot{m}_e v_e^2}{2P_E} \tag{3.37}$$

and subscripts S, P, and E refer to structure, propellant and electric power supply respectively, P_E is the electric power. The mass flow rate is given by

$$\dot{m}_e = \frac{M_P}{t_B} \tag{3.38}$$

where the burn time in seconds is represented by t_B (for continuous thrust transfers $t_B = $ transfer time) and the mass flow rate $\dot{m}_e$ is assumed constant. Hence, the exhaust velocity can be written as

$$v_e = \sqrt{\frac{2\nu P_E}{\dot{m}_e}} = \sqrt{\frac{2\nu\eta M_E}{\dot{m}_e}} = \sqrt{\frac{2\nu\eta t_B M_E}{M_P}} \tag{3.39}$$

and as a result the thrust is given by

$$T = \dot{m}_e v_e = \sqrt{2\dot{m}_e \nu \eta M_E} = \sqrt{\frac{2\nu\eta M_E M_P}{t_B}} \tag{3.40}$$

where the electric power is assumed to be proportional to the mass of the power supply. Using given thruster specifications and the calculated transfer time, the propellant mass M_P can be defined in terms of the power supply mass M_E using Eq. (3.40). Furthermore, The rocket equation (Eq. (3.33)) now becomes:

$$v = \sqrt{\frac{2\nu\eta M_E}{\dot{m}_e}} \log_e(1 + \frac{M_P}{M_S + M_E}) \tag{3.41}$$

where the electric power is represented as a function of the power supply mass. Now, Eq. (3.41) can be solved for M_P or M_E by substituting $\dot{m}_e$ from Eq. (3.38) and either M_P or

M_E from Eq. (3.40).

3.5.2 Chemical Propulsion

The basis for fuel mass analysis presented at the beginning of this section can also be applied to chemical propulsion systems. These systems are necessary when considering impulsive transfers, as is the case for Lambert's theorem. When analyzing a chemical spacecraft propulsion system the exhaust velocity v_e is usually given in terms of the *specific impulse* of the engine in the following way:

$$v_e = g_e I_{sp} \tag{3.42}$$

where g_e is the acceleration due to gravity at the surface of the Earth. Equations (3.34) and (3.42) are combined to find the mass of propellant required to achieve a manoeuvre with a given ΔV cost:

$$\Delta V = v_e \log_e\left(\frac{M_P + M_d}{M_d}\right) = g_e I_{sp} \log_e\left(\frac{M_P + M_d}{M_d}\right) \tag{3.43}$$

where mass at ignition has been divided into M_P, the mass of propellant required and M_d, the dry mass of the system. Lastly, Eq. (3.43) is re-arranged to find the propellant mass for a given transfer ΔV using chemical propulsion:

$$M_P = M_d \exp\left(\frac{\Delta V}{g_e I_{sp}}\right) - M_d \tag{3.44}$$

Eq. (3.44) will be used in Section 4.2 to compute the mass of fuel required for the impulsive transfers.

3.6 Minimum-Time Low-Thrust Optimal Control Problem

To achieve a rendezvous between the chaser and the debris sufficient for ADR, a high accuracy point-to-point transfer is required. It is therefore important to take into account the changes in true anomaly as well as the other orbital elements of both the chaser and

the debris in designing such a transfer. This is a somewhat different scenario from other missions with continuous low thrust propulsion. The aim of the optimization formulation presented here is to achieve a high accuracy transfer in LEO and to determine the trajectory and the control directions.

3.6.1 Optimal Control Problem Formulation

The objective function for the optimization problem to be solved is:

$$J = t_f \tag{3.45}$$

for a chaser with the state, $\boldsymbol{\alpha}$

$$\boldsymbol{\alpha} = (p, f, g, h, k, L, m) \tag{3.46}$$

defined as in Section 2.2.3, with the added m term included as a means of calculating the mass of propellant required for a given transfer. The state $\boldsymbol{\alpha}$ is subject to the dynamics described in Section 2.2, Eqs. (2.9-2.16). Transfer time is chosen as the minimization objective due to the continuous thrust nature of the transfer: if the thrust is constant and continuous, the shortest transfer time is also the most fuel efficient.

The solution of the optimization problem in (3.45) is subject to boundary constraints. As such, the boundary conditions for the orbit transfer are described in terms of classical orbital elements and converted to modified equinoctial elements using Eqs. (2.1-2.6). The chaser starts in a near-circular inclined low Earth orbit, and the initial debris location is given by two-line-elements [12] data at time $t_0 = 0$. The initial orbit is specified in terms of classical orbital elements as

$$\begin{bmatrix} a(t_0) & e(t_0) & i(t_0) & \Omega(t_0) & \omega(t_0) & \theta(t_0) \end{bmatrix} = \begin{bmatrix} a_0 & e_0 & i_0 & \Omega_0 & \omega_0 & \theta_0 \end{bmatrix} \tag{3.47}$$

The orbital transfer of the chaser is terminated at the debris location after propagation, given by

$$\begin{bmatrix} a(t_f) & e(t_f) & i(t_f) & \Omega(t_f) & \omega(t_f) & \theta(t_f) \end{bmatrix} = \begin{bmatrix} a_f & e_f & i_f & \Omega_f & \omega_f & \theta_f \end{bmatrix} \tag{3.48}$$

Finally, during the transfer, the thrust direction **u** must remain a unit vector. Thus, the equality constraint given by Eq. (3.49) is enforced at all points during the transfer.

$$||\mathbf{u}||_2 = u_r^2 + u_\theta^2 + u_h^2 = 1 \tag{3.49}$$

3.6.2 Solving the Minimum-Time Low-Thrust Optimal Control Problem

The minimum-time low-thrust optimal control problem outlined in Section 3.6 is solved using the optimal control software GPOPS-II [4] introduced in Section 2.3.1. The boundary conditions, constraints, and equality errors (error in Eq. (3.49)) of the optimal control problem are estimated and checked against the desired error tolerances. If the tolerances are satisfied, a solution is found and the problem is solved; if not, a new mesh is determined and the unsatisfactory solution is used as the initial guess.

In addition, to achieve a high accuracy transfer, it is necessary to match the chaser's arrival location to the actual location of the debris after the transfer time. This means the location of the debris needs to be propagated for the duration of the estimated transfer time, and a new transfer problem needs to be solved for the new debris location. As a result, a novel iterative procedure is proposed here, to ensure that the chaser and debris rendezvous to the desired accuracy at the same time, given certain orbital perturbations. Furthermore, for each iteration, the optimal control problem can only be solved and converge to a solution if given a good initial guess. When generating the initial guess, the procedure for which is detailed in Section 3.6.3, it needs to contain approximately the same number of revolutions as that required for the transfer. A novel aspect of the initial guess generation is the inclusion of desired RAAN changes in the objective function.

Given that the chaser is transferred to an estimated debris location, an iterative procedure is introduced in order to achieve convergence between the final chaser location and the actual debris location after transfer. By propagating the debris orbital elements for the duration of the rendezvous found using the methodology described in Section 3.6.3, a more accurate location of the debris can be found, and the full optimal control problem can be solved again for the updated debris location. The iterations are repeated until the chaser

location after the transfer matches the propagated debris location after said chaser transfer time. This iterative procedure is illustrated in Figure 3.6, where an optimal control problem is solved, in which the chaser is transferred to the initial debris orbit ($C \rightarrow D_i$) in t_c^0 days. The debris is then propagated (P_1) for duration t_c^0 and a new debris location is found. The chaser is transferred to new debris location ($C \rightarrow D_{P_1}$) and a new transfer time t_c^1 is found. The debris is then propagated (P_2) for t_c^1 days and a corresponding transfer time to this next location is calculated. This process is repeated until the difference in sequential propagation times, $t_c^n - t_c^{n-1}$, is smaller than a desired specified tolerance. Figure 3.6 highlights two scenarios, one in which the piece of debris is moving further away from the chaser after each iteration and one where the piece of debris moves closer to the chaser after each iteration.

The iterative procedure described above is initiated by specifying each debris location only at the beginning of the mission. This means consecutive pieces of debris in the multiple debris removal mission are propagated from the beginning of the mission over the time taken to remove previous pieces of debris through to the rendezvous with the piece of debris at hand. However, the chaser transfer time is only considered as the time from the moment the chaser and the previous piece of debris had arrived in the disposal orbit, to the time of rendezvous between the chaser and the current piece of debris.

It should be noted that the iterative procedure proposed here is chosen over introducing the debris propagation as a constraint within the NLP solver for two reasons. First, introducing a high fidelity optimal propagator, such as D-SPOSE, into a NLP solver such as GPOPS-II significantly increases the computational cost of solving the problem. Second, having a de-coupled system, that is, a debris propagator independent of the NLP solver, allows for flexibility of using different orbital propagators, as well as selecting required perturbations to achieve varying degrees of propagation accuracy.

3.6.3 Initial Guess Generation

Due to the nature of the problem being solved, the solution will contain a large number of orbital revolutions of the chaser ($\sim$100-400 as will be seen in Chapter 4 numerical results). As such, in order for GPOPS-II to converge to the solution, a good initial guess in terms

3.6 Minimum-Time Low-Thrust Optimal Control Problem
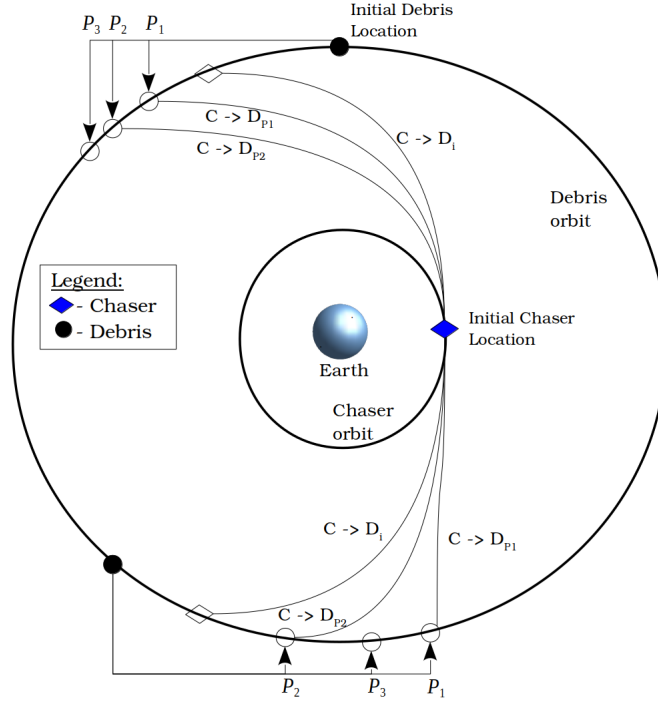
Figure 3.6: Illustration of iterative rendezvous process

of the number of revolutions required to complete the transfer needs to be found. A good initial guess is important for solving this problem due to the accuracy requirement of the transfer. This means that the solution is unlikely to converge to a transfer, which satisfies all the constraints unless the initial guess is close to the required transfer in terms of revolutions and transfer time.

The procedure for generating the initial guess requires two steps. The first step is finding a coarse initial guess using a variable step ordinary differential equation solver (ODE45 in Matlab) by propagating the modified equinoctial dynamics from the initial conditions over an estimated time for transfer. The estimated time for transfer is found using Edelbaum's analytical low-thrust transfer analysis described in Section 3.3. In computing this coarse initial guess, the control direction is assumed to lie along the direction of the inertial velocity of the chaser, that is,

$$\mathbf{u} = \mathbf{Q}_r^T \frac{\mathbf{v}}{||\mathbf{v}||} \tag{3.50}$$

where $\mathbf{Q}_r$ is defined as in Section 2.1.3.

The second step of generating the initial guess requires refining the guess found in step one, and the procedure is based on that outlined in [133], with a new modification to the objective function used. Here, the initial guess from the first step is used to solve a sequence of optimal control subproblems. Solving each subproblem results in the state after one true longitude cycle, which has the minimum difference from the desired end state for the whole transfer. The objective function is defined based on the mean-square relative difference:

$$
J = w_1 \left[\frac{p(L_{rev}) - p_f}{1 + p_f} \right]^2 + w_2 \left[\frac{f^2(L_{rev}) + g^2(L_{rev}) - e_f^2}{1 + e_f^2} \right]^2
$$
$$
+ w_3 \left[\frac{h^2(L_{rev}) + k^2(L_{rev}) - \tan^2(0.5i_f)^2}{1 + \tan^2(0.5i_f)} \right]^2 + w_4 \left[\frac{\frac{k(L_{rev})}{h(L_{rev})} - \tan(\Omega_f)}{1 + \tan(\Omega_f)} \right]^2
$$

(3.51)

where p_f, e_f, i_f, Ω_f, are the desired final semi-latus rectum, the desired final eccentricity, the desired final inclination, and the desired final RAAN respectively; w_n, $n = 1, ..., 4$ are the weights to prioritise the different terms. Subscript rev refers to the value of the true longitude after one revolution. The objective function stated in Eq. (3.51) is a modification of that defined in [133], as it includes the fourth term to allow a degree of control and priority of desired RAAN changes. The subproblems are solved under the dynamic constraints Eqs. (2.17)-(2.22) and Eq (2.16) described in Section 2.2 and the equality constraint given by Eq. (3.49). The optimal control subproblems are solved sequentially using the result of the previous subproblem as the starting point for the next, until the desired final state is reached. Once the desired end state is reached, the results (state and control) of each subproblem are combined to provide an initial guess for the entire transfer.

The particular choice for the weights w_n is important and has a significant effect on the outcome of the optimization. For instance, in general cases where no particular emphasis is put on any of the orbital parameters, the weights are set as $w_1 = w_2 = w_3 = w_4 = 1$. Other values for the weights can be chosen based on which non-dimentionalized term in Eq. (3.51) requires the most significant change; for example, if there are large differences in the non-dimentionalized semi-major axis and RAAN of the chaser and the piece of debris, as compared to the differences in non-dimentionalized inclination and eccentricity, then w_1

and w_4 will be significantly larger than w_2 and w_3. One way to perform this comparison is by considering the change in a given orbital element of the transfer on hand and the rate of change of the same orbital element. Similar consideration is given to the other orbital elements of interest and finally, based on which orbital elements require large changes with lower rates of change, the weights can be distributed accordingly. For the research presented in this thesis, special cases include the following: de-orbiting, where only the change in semi-major axis is important, so that $w_1 = 1$, and $w_2 = w_3 = w_4 = 0$, and large changes in inclination where $w_3 = 10$, and $w_1 = w_2 = w_4 = 1$. Some convergence issues have been encountered where the value of two or more orbital parameters converge at the same rate and then oscillate outside of the desired region. This can be solved by increasing the weighting on one or more of said parameters, changing the convergence rate and thereby allowing the solver to converge to a solution within the tolerance region.

3.6.4   Including a Drift Orbit

The last special aspect of the optimized transfer solution proposed here is the incorporation of the drift orbit into the transfer manoeuvre. As outlined in Section 3.2.2, to achieve certain RAAN changes that would otherwise be too costly in terms of fuel, an optimized drift orbit can be found, in which the chaser can be parked during the rendezvous stage of an ADR mission. Considering Eq. (3.2), the natural drift rate is inversely proportional to the altitude of the orbit. This means the drift orbit should be at as low an altitude as possible, while ensuring that the aerodynamic drag does not cause significant perturbations to the drift orbit parameters during drift. A conservative estimate obtained using the D-SPOSE tool, described in Section 2.3.2 of the decay rate at an altitude of 500 km is 0.14 km/day, which is deemed sufficiently low for the purpose of the drift orbits.

The inclination of the drift orbit is determined by minimizing the overall rendezvous time:

$$\min_{i_{drift}} \quad f(i_{drift}) = t_{transfer1} + t_{transfer2} + t_{drift}$$

$$\text{subject to} \quad g_1(i_{drift}) = \Delta V_{a,i} - \Delta V_{max} \leqslant 0 \tag{3.52}$$

$$g_2(i_{drift}) = t_{total} - t_{max} \leqslant 0$$

where $\Delta V_{a,i}$ is the sum of the total transfer ΔV for transfers 1 and 2 (transfer 1 being the

transfer from the initial chaser orbit to the drift orbit and transfer 2 the transfer from the drift orbit to the debris location, as depicted in Figure 3.3), and accounts for any ΔV required to match the debris RAAN; ΔV_{max} is the ΔV estimate (compute using Edelbaum's formulation) for performing the rendezvous without a drift orbit; t_{total} is the sum of the total transfer time taken to rendezvous with the debris ($t_{transfer1} + t_{transfer2} + t_{drift}$) as shown in Figure 3.3, and t_{max} is the maximum allowable time for the transfer. The parameters t_{max} and ΔV_{max} are constants for a given transfer, and t_{max} is user defined. The values for $t_{transfer}$ and $\Delta V_{a,i}$ for both orbital manoeuvres during rendezvous are calculated using Edelbaum's equations for low-thrust orbit-to-orbit transfers (Eqs. (3.6) and (3.9) in this thesis). The estimate for t_{drift} is calculated by comparing the drift rate of a given drift orbit, Eq. (3.2) to the drift rate of a given piece of debris and finding the time taken for the chaser RAAN to 'catch up' to the debris RAAN, while accounting for the RAAN changes that will occur during transfer 2 (i.e., after the drift orbit).

3.7   Chapter Summary

Three problem definitions and the associated solutions for achieving multiple debris removal are presented in this chapter in Sections 3.3, 3.4, and 3.6 respectively. The first approach makes use of Edelbaum's methodology to achieve low thrust orbital transfers in a low fidelity manner. For the second approach Lambert's theorem is applied to impulsive orbital transfers as a comparative case for the first approach. The third approach defines each orbital transfer as a minimum-time low-thrust optimal control problem and represents a higher fidelity solution to low thrust transfers where each rendezvous is an optimized high accuracy point-to-point transfer. The de-orbiting phases are optimized orbit-to-orbit transfers, as the position of release within the disposal orbit is assumed arbitrary. For the first two problem definitions, the de-orbiting stage is analyzed using Edelbaum's formulation. For the third problem definition, a simplified optimal control is solved for the de-orbiting stage, where the final boundary constraint is only defined in terms of the semi-major axis and no iterations are needed. Each procedure developed gives an estimation of the time and fuel requirements for the different phases of the complete multi-debris removal mission.

As the notion of multiple debris removal is in its infancy, some unique aspects of such missions, as compared to missions designed to remove only a single piece of debris, are

3.7 Chapter Summary

identified and analyzed. In Section 3.2.1 the debris selection and sequencing process, used to minimize mission cost, is presented, followed by an analysis of RAAN limitations encountered when considering low-thrust orbital transfers and how these can be overcome by including RAAN drift orbits during the rendezvous stage of multiple debris removal missions in Section 3.2.2. More specifically, there is a bounded RAAN change that can be achieved for a given change in altitude and inclination. As long as there are a large number of pieces of debris within a small inclination range, the subsequent piece of debris to be de-orbited can be chosen to fall into the achievable RAAN range. However, in the event where only a limited choice of debris is available, chaser RAAN change limitations need to be overcome in order to achieve rendezvous.

4

Multiple Debris Removal Case Studies

Presented in this chapter are the results generated from analysing case studies consisting of various debris sets, based on the formulations presented in Chapter 3. These results are the transfer times and fuel mass requirements for removing said debris sets. The case studies presented all make use of TLE data [12] to define the debris orbits and initial location. When applying the high fidelity approach outlined in Section 3.6 the mission requires a starting date defined as the 1st of January 2016, selected as an arbitrary date such that accurate historical data (two-line elements and atmospheric density) can be used for simulation purposes. The debris sets selected for each case study are picked based on three distinct debris parameters, namely: the inclination band, the RAAN of the debris orbit, and the specified risk factor of each debris. These debris selection criteria are in addition to the premise that we are considering only large pieces of debris in LEO.

4.1   Mission Parameters

For the results presented in this chapter, the mass of the chaser is assumed to be 2000 kg [92], as this is considered to be an adequate mass for removing large pieces of debris. The initial orbit of the chaser which is the same as the disposal orbit of the debris is only constrained to have an altitude of 200 km. This is both a realistic parking orbit and the decay rate of space debris at this altitude is reduced from an order of hundreds of years to within one year, i.e., the decay rate of the debris is high enough for it to burn up or enter the Earth's atmosphere without creating a significant collision risk.

Object	a (km)	i (deg)	RAAN (deg)	Mass (kg)
Chaser	6571	97.9	45.0	2000
Daichi	7064	97.9	45.0	4000
Envisat	7143	98.3	89.8	8111
Zenit-2 stage-2	7374	99.3	235.7	9000
Zenit-2 stage-2	7185	98.5	235.7	8226
H-2A stage-2	7164	98.4	245.1	4000
Chaser	6578	82.5	101	2000
Debris 1	7378	82.5	101	~1440
Debris 2	7377	82	100.5	~1440
Debris 3	7400	81.6	100	~1440
Debris 4	7377	82.3	99.5	~1440
Debris 5	7388	81.9	99	~1440

Table 4.1: Debris and chaser sets 1 & 2 used for analysis using Edelbaum and Lambert's formulations - orbital parameters and mass

4.2   Results Using Edelbaum and Lambert's Formulations

Using Edelbaum's and Lambert's formulations presented in Sections 3.3 and 3.4 two sets of LEO debris, chosen based on [98] and [155] respectively, are analyzed to demonstrate the low fidelity approach to solving the motion planning problem for a multiple debris removal mission. The aim here is to compare and contrast the results of the two formulations in terms of the estimated time needed and the fuel cost of carrying out a multiple debris removal mission. The pieces of debris considered were chosen in accordance with the criteria outlined in Section 3.2.1. The first set of debris is chosen based on the high risk to the space environment posed by each piece of debris, notably this set includes Envisat which is predicted to present the highest risk. As such, each piece of debris in set 1 is situated in highly congested Sun synchronous orbits, having similar orbital inclinations. For set 1, no special consideration has been given to the RAAN nor the mass of the pieces of debris other than a minimum mass requirement of 500 kg. The second set of debris (Debris 1-5) consists only of unnamed SL-8 rocket bodies with similar masses, all situated in similar inclination and RAAN orbits. The debris data for the two sets can be found in Table 4.1.

For the results presented here, the debris sequence which minimizes the cost in the recursive scenario is in ascending RAAN order for set 1 and descending RAAN order for

set 2, as found from the exhaustive approach detailed in Section 3.2.1. For comparison these are also the same debris orders used in the mothership scenario. Results for each mission presented below were constrained using $\Delta V_{max} = 7$ km/s and $t_{max} = 365$ days.

A summary of the results of the recursive mission scenario for debris sets 1 and 2 can be found in Table 4.4 where we present the mission objective, the total ΔV requirement, the total time taken, the power supply mass, and the mass of propellant required. For debris set 1, it was not possible to carry out the mission using the recursive strategy while satisfying both the ΔV and maximum time constraints. However, the detailed results of the rendezvous phase when only satisfying the fuel cost constraint can be found in Table 4.2 and the results for the de-orbit phase are given in Table 4.5. The breakdown of the results for debris set 2 can be found in Table 4.2. As can be seen, the cost both in terms of time and ΔV are larger for the debris set 1. The large differences in RAAN for this set imply that a much longer drift time is required in order to satisfy the ΔV constraint; however, as the debris in set 1 also have higher mass the transfer times are higher as well. This means there is not as much leeway in terms of trading off time and ΔV in set 1 despite introducing a drift orbit.

Some observations are made based on the drift orbit parameters presented in Table 4.2. First, for debris set 1, the RAAN differences are large, meaning, the RAAN drift (calculated using Eq. (3.2)) needs to be as high as possible to compensate. As such, the semi-major axis is, for the most part, at the lower constraint (same as disposal orbit), and the inclination is as far from $90°$ as possible, without introducing a ΔV cost exceeding that needed to change the RAAN in the first place. Second, for debris set 2 where the RAAN differences are smaller, two scenarios unfold. One scenario where the drift orbit semi-major axis is near that of the disposal orbit and the difference in inclination between that of the previous debris and the drift orbit inclination is small. In this scenario, the drift rate increase as a result of the low altitude is sufficient. In the second scenario, the semi-major axis of the drift orbit is similar to that of the target debris and the difference in drift orbit inclination and target debris inclination is sufficient to account for the RAAN change required.

Based on the results given in Table 4.4, debris set 1 cannot be de-orbited within the constraints chosen. As expected, the ΔV is high for the recursive approach despite introducing a drift orbit, which justifies the use of low continuous thrust transfers. For debris

4.2 Results Using Edelbaum and Lambert's Formulations

Debris name	ΔV_R (km/s)	t_R (days)	a_{drift} (km)	i_{drift} (deg)
Daichi	0.273	12.6	N/A	N/A
Envisat	0.554	177	7000	100.0
Zenit-2 stage-2	2.85	174	6578	105.4
Zenit-2 stage-2	1.03	98.9	6578	101.1
H-2A stage-2	0.609	28.8	6583	99.50
Total	**5.32**	**488**	**N/A**	**N/A**
Debris 1	0.439	35.0	N/A	N/A
Debris 2	0.748	38.2	7328	80.91
Debris 3	1.01	34.2	6578	82.76
Debris 4	0.831	38.5	6892	83.61
Debris 5	0.927	38.7	7388	81.07
Total	**3.95**	**185**	**N/A**	**N/A**

Table 4.2: Results of recursive approach, for debris sets 1 and 2 - rendezvous only

set 1 with an active ΔV constraint (ΔV_{max} mission in Table 4.4) the total mission time is 826 days. Notably, the time constraint could not be satisfied for set 1 and the minimum time solution (min. t mission in Table 4.4) is the trivial case where no drift orbit is included in the rendezvous phase. In the minimum time case the mission time would be 422 days with the infeasible ΔV cost of 44.1km/s. The mission is feasible for the given constraints for debris set 2 and a minimum is found with a mission time of 359 days and a ΔV of 6.14km/s.

A summary of the results of the mission scenario using a mothership approach for debris set 1 and debris set 2 can be found in Table 4.4. In this mission scenario, a transfer orbit between each consecutive debris was designed and implemented in order to find the ΔV cost and transfer times of such an approach. The total ΔV requirement for the mothership approach is the sum of all the ΔV transfer requirements, i.e., the rendezvous of the mothership with the each piece of debris and the de-orbit ΔV required by each packet. In addition, the packets are assumed to be able to de-orbit the debris using low continuous thrust (Edelbaum formulation) and the values for the de-orbit phase in the mothership scenario can be found in Table 4.5. The mass of the packets, excluding propellant and power supply, assumed for the de-orbit calculations is 30 kg as mentioned in [164] and the thrusters are assumed to provide 0.16 N of continuous thrust based on thrusters specifications given in

Debris name	ΔV_1 (km/s)	ΔV_2 (km/s)	ΔV_R (km/s)	t_R (min)
Daichi	0.145	0.174	0.319	4.95
Envisat	3.51	6.43	9.94	5.37
Zenit-2 stage-2	0.331	6.93	7.26	6.26
Zenit-2 stage-2	0.630	0.056	0.689	140
H-2A stage-2	0.308	1.85	2.16	30.0
Debris 1	0.157	0.080	0.237	4.53
Debris 2	0.027	0.073	0.100	6.30
Debris 3	0.165	0.452	0.617	56.2
Debris 4	0.268	0.052	0.320	57.4
Debris 5	0.115	0.041	0.156	27.0

Table 4.3: Results of mothership approach for debris sets 1 and 2

[162]. The packets allow for the de-orbit phase to occur simultaneously to the consecutive rendezvous phase and the total mission time is therefore the sum of the rendezvous transfer times added to the de-orbit time of the last piece of debris brought to disposal orbit. The de-orbit takes days to complete whereas the impulsive rendezvous transfers take hours, hence the removal of the debris occurs within the time of the longest de-orbit plus the total rendezvous time. The total mission time for debris set 1 is therefore $t_{total} = 258$ days and the total mission ΔV cost is $\Delta V_{total} = 22.1$ km/s which is infeasible. The total mission time for debris set 2 is 47.4 days and the total mission ΔV cost is 3.26 km/s. The ΔV cost for set 1 is again much greater as the RAAN differences between each piece of debris in this set are much larger than the corresponding differences for debris in set 2. The de-orbit times for set 1 remain higher as the masses and RAAN differences of the debris in set 2 are much lower than those in set 1.

For set 1, the recursive approach is not able to satisfy the two constraints that we imposed on the mission, but does produce a feasible solution at the maximum allowed ΔV cost of 7 km/s with the mission time of over 2 years. On the other hand, the mothership solution requires an unrealistic ΔV cost to de-orbit this debris set. For debris set 2, there is a recursive mission plan which satisfies both the time and ΔV costs, with a small margin from the maxima imposed. The mothership approach requires approximately half the ΔV of the recursive solution and a small fraction of time to carry out the de-orbit mission for set 2. From that perspective alone, it may be the solution of choice for the de-orbit mission

of debris set 2. However, further analysis of both mission plans is required to assess the fuel mass needed for the two approaches, plus the costs associated with the capture of the debris that are suitable for the two types of missions.

Based on the ΔV and time requirements, the fuel required to perform each mission is estimated and given in Table 4.4. The thruster specifications used to make these estimates are summarized in Table 4.6 and the mass-to-power ratio of the power supply is taken as 32 kg/kW, deemed an appropriate value based on [106, 162]. For the minimum time mission in Table 4.4 no masses are given as the ΔV is so high that the mission is rendered infeasible. The mass of the power supply for the mothership approach is the sum of all power supplies required for the packets each of which has a mass of ~ 99 kg. The fuel mass required for the mothership approach is the sum of the fuel required for each packet added to the fuel required for all the rendezvous transfers. It is evident that a lower $M_E +$ M_P is required for low continuous thrust transfers, even with the requirement of a power supply. When comparing the results for sets 1 and 2 using the recursive approach, the lower time needed for set 2 means that the power supply is heavier. This is because the ratio of fuel mass to power supply mass is highly dependent on transfer time as evident from Eq. (3.38). Furthermore, it can be shown from the mass analysis that a high ΔV can render the mission infeasible due to exceedingly high fuel mass requirements. Therefore, the mothership approach is not suitable for debris set 1 as it requires too much fuel.

Set	Mission	ΔV_{total} (km/s)	t_{total} (days)	M_E (kg)	M_P (kg)
		Recursive Approach			
1	min. t	44.1	422	N/A	N/A
1	ΔV_{max}	7	826	899	514
2	optimal	6.14	359	1110	276
		Mothership Approach			
1	N/A	22.1	258	497	2.07×10^7
2	N/A	3.61	47.4	497	2259

Table 4.4: Mission costs summary for recursive and mothership approaches

Debris	ΔV_{Do} (km/s)	t_{Do} (days) - R	t_{Do} (days) - M
Daichi	0.273	63.8	98.0
Envisat	0.314	80.0	161
Zenit-2 stage-2	0.432	102	205
Zenit-2 stage-2	0.336	46.7	258
H-2A stage-2	0.325	45.2	94.8
Total	**1.68**	**338**	**N/A**
Debris 1	0.439	35.0	46.7
Debris 2	0.434	34.5	46.1
Debris 3	0.445	35.5	47.3
Debris 4	0.434	34.5	46.1
Debris 5	0.434	34.6	46.2
Total	**2.19**	**174**	**N/A**

Table 4.5: De-orbit results, sets 1 and 2 - recursive approach (R) and mothership approach (M)

Thruster Name	Manoeuvre	Propulsion	Thrust (N)	I_{sp} (s)
NASA HiPEP	Recursive - All	Electrical	0.5	9000
T-140	Packet - DO	Electrical	0.16	2200
Bipropellant Thruster	Packet - R	Chemical	22	300

Table 4.6: Thruster specifications for De-orbit (DO) and Rendezvous (R) manoeuvres

4.3 Results Using Point-to-Point Optimal Control

Using the high fidelity approach detailed in Section 3.6, three different case studies have been considered. In the first case study, debris with similar orbital inclination are used, in the second case study debris with large inclination differences are considered, and in the third case study drift orbits are included in the analysis and the same debris as those in set 1 are considered. Given the results presented in Section 4.2, removing debris set 1 using a recursive approach is very costly and these debris are therefore only considered in the scenario where a drift orbit can be included. Furthermore, this high fidelity approach to analysing a recursive multiple ADR mission takes into account the changing orbital state of the debris as the mission is carried out/simulated. Therefore, more detailed debris data

4.3 Results Using Point-to-Point Optimal Control

(in the form of raw TLE data) than that available in [155], used in Section 4.2, is required. In addition, without introducing a drift orbit, when propagated, the debris in set 2, does not fall within an achievable RAAN envelope. To account for this, the debris sets in Sections 4.3.1 and 4.3.2 are chosen from the entire tracked set of SL-8 rocket bodies in LEO, which all have similar characteristics to debris set 2 in Section 4.2 allowing for some comparison, while also demonstrating the various nuances and capabilities of this high fidelity approach.

For the point-to-point continuous thrust manoeuvres presented here, the thrust T of the chaser is taken as 0.5 N, and the specific impulse I_{sp} in chosen to be 2000 s [106]. In addition, for completing an iteration of the procedure presented in Section 3.6.2, reasonable and practical constraints on the accuracy of matching the orbital elements of the chaser and the piece of debris are assumed, as well as the time difference between the chaser after transfer and the piece of debris post-propagation. In particular, each iteration is only complete if the final orbital elements of the chaser match those of the piece of debris to within the following accuracies:

$$a_f = a_d \pm 0.5 \text{ km}$$
$$e_f = e_d \pm 0.001$$
$$i_f = i_d \pm 0.01°$$
$$\Omega_f = \Omega_d \pm 0.1° \tag{4.1}$$
$$\omega_f = \omega_d \pm 10°$$
$$\theta_f = \theta_d \pm 1°$$
$$t_c^n - t_c^{n-1} \leqslant 0.003 \text{ days}$$

The 0.5 km semi-major axis tolerance specified in Eq. (4.1) is deemed an adequate distance for initiating close range rendezvous [165]. The 0.001 tolerance on e_f is of the same order of magnitude as the eccentricity of the debris themselves; however, as all pieces of debris considered are in near-circular orbits with eccentricities in this order of magnitude, the effect of the difference in eccentricity on the accuracy of the rendezvous is negligible. The other orbital elements margins were chosen based on attainability with current propulsion capabilities, while accounting for perturbations. The constraint placed on the final argument of perigee $\omega(t_f)$ is large as compared to those put on the other orbital parameters as the

77

pieces of debris are all located in near-circular orbits, meaning differences in ω have a significantly smaller effect on the accuracy of the rendezvous. A constraint of $\pm 10°$ is chosen as this is the angular difference in argument of perigee that results in a variation in semi-major axis of $\sim \pm 0.5$ km at an eccentricity of 0.0055 (the maximum for the case studies considered).

4.3.1 Similar Inclination Band

The initial locations defined using orbital elements of the SL-8 rocket bodies are shown in Table 4.7 for a similar inclination band debris set. The debris in Table 4.7 were chosen due to the small differences in inclination between the debris orbits (inclination ranges between $82.90° - 82.95°$) and all have a mass of ~ 1440 kg. Small changes in inclination require significantly more fuel than small changes in altitude. Furthermore, changes in RAAN can be compensated for to a certain extent due to the effect of oblate Earth perturbations. Consequently, it is a priority to keep the inclination changes small, as opposed to changes in other orbital elements like semi-major axis or RAAN. As already noted, the orbits are nearly circular with altitudes between 700 and 1100 km.

Name	Norad ID	a (km)	e	i (deg)	Ω (deg)	ω (deg)	θ (deg)
Chaser	N/A	6571	0.0000	82.90	6.500	0.000	0.000
Debris 1	25569	7364	0.0021	82.94	3.078	184.1	239.0
Debris 2	22889	7349	0.0049	82.94	354.1	283.1	86.03
Debris 3	13758	7342	0.0029	82.91	347.3	60.47	348.6
Debris 4	20046	7349	0.0043	82.94	339.8	120.0	259.4
Debris 5	11327	7353	0.0027	82.95	331.0	227.9	85.10

Table 4.7: Debris set 3 and chaser initial locations for high fidelity similar inclination band transfers

A summary of the results for this set of debris can be found in Table 4.8 with the full set of iterative results presented in Table A.1 in Appendix A. Each line in the table represents either a propagation, for example Deb.3 P_5 refers to piece of debris number 3, propagation number 5 (P_n in Figure 3.6), or an orbital transfer, for example chaser to Deb.3 P_5 is the transfer of the chaser from its initial position (after removing debris 2) to debris 3 after propagation 5. The initial location of the pieces of debris shown is the location of the debris at the very beginning of the mission. In addition, the total time is the accumulated

4.3 Results Using Point-to-Point Optimal Control

time at the given mission stage.

When propagating pieces of debris other than the first one in the sequence, the time taken to rendezvous and de-orbit previous debris also needs to be taken into account, and the propagation time for the piece of debris is therefore cumulative and does not correspond to the chaser transfer time to that piece of debris. Thus, for example, the time indicated in Table 4.8 for Deb.3 P_5 is the time taken to remove debris 1 and 2, in addition to the time for the chaser to transfer to Deb.3 P_5. Furthermore, the later the piece of debris appears in the five debris sequence, the longer it will be propagated, and therefore the effects of perturbations will be more significant. During propagation, the semi-major axis of the debris may increase slightly due to the nature of the gravitational perturbations acting on them. It should also be noted that the chaser is assumed to embark on each consecutive rendezvous immediately after the previous piece of debris is de-orbited. The de-orbit results are calculated using the same methodology as the rendezvous, except only with a constraint on semi-major axis and all the other orbital elements left 'free' for the final disposal orbit. The time taken to de-orbit is significantly longer due to the combined mass of the debris and the chaser.

As the rendezvous with each piece of debris is of similar nature, a closer look at the specific results for one piece of debris (Figures 4.1-4.4) is adequate to provide insights into the chaser transfer response and control inputs of the full set. Figure 4.1 illustrates the path of the chaser during rendezvous with debris 3 and indicates initial and final locations of the chaser. During the transfer, the chaser revolves 293.6 times around the Earth and since the start of the mission, debris 3 has revolved 1877.6 times around the Earth. The three plots in Figure 4.2 show the progression of semi-major axis, inclination, and RAAN respectively over the course of the transfer for both the chaser and the debris; as can be seen, the orbital elements of the chaser reach the desired (debris) values at the end of the transfer. It is important to note that the dynamics of the semi-major axis, inclination, and RAAN are coupled, making the solution non-trivial. Oscillations in each of the variables are highlighted, and these occur due to the perturbing effects of the Earth's oblateness. The control direction components (u_r, u_θ, u_h) are shown in Figure 4.4. The most significant changes in inclination occur within the first ~4 days which is reflected in the larger oscillations in u_h during this time, as well as the irregularities in u_r and u_θ. After ~4 days, the radial compo-

4.3 Results Using Point-to-Point Optimal Control

Transfer Description	a (km)	e	i (deg)	Ω (deg)	ω (deg)	θ (deg)	Time (days)	Total Time (days)
Debris 1 initial	7363.6	0.0021	82.94	3.078	184.1	239.0	N/A	0.000
Chaser to Deb.1 initial	7363.5	0.0017	82.93	2.981	193.5	240.0	19.67	19.67
Deb.1 P_6	7374.4	0.0019	82.95	348.5	122.3	212.7	19.82	19.82
Chaser to Deb.1 P_6	7373.9	0.0009	82.96	348.4	132.3	213.7	19.82	19.82
Chaser and Deb.1 de-orbit	6579.0	0.0006	82.95	318.8	149.8	287.4	32.90	52.72
Debris 2 initial	7349.0	0.0049	82.94	354.1	283.1	86.03	N/A	0.000
Chaser to Deb.2 initial	7348.5	0.0039	82.95	301.2	288.5	87.03	19.23	71.96
Deb.2 P_2	7348.9	0.0053	82.94	300.8	79.71	89.17	71.96	71.96
Chaser to Deb.2 P_2	7348.4	0.0043	82.93	300.9	85.03	90.17	19.24	71.96
Chaser and Deb.2 de-orbit	6579.0	0.0026	82.99	271.5	348.0	41.46	32.51	104.5
Debris 3 initial	7342.6	0.0029	82.91	347.3	60.47	348.6	N/A	0.000
Chaser to Deb.3 initial	7342.1	0.0035	82.92	254.3	70.47	349.6	19.27	123.7
Deb.3 P_8	7339.1.0	0.0028	82.91	254.3	60.47	245.9	124.0	124.0
Chaser to Deb.3 P_8	7338.6	0.0018	82.92	254.2	70.47	246.9	19.39	124.0
Chaser and Deb.3 de-orbit	6579.0	0.0012	82.91	225.2	6.912	224.2	31.90	155.9
Debris 4 initial	7349.0	0.0043	82.94	339.8	120.0	259.4	N/A	0.000
Chaser to Deb.4 initial	7348.5	0.0033	82.93	207.0	110.0	258.4	19.74	175.6
Deb.4 P_3	7340.6	0.0029	82.93	209.0	29.36	280.6	175.1	175.1
Chaser to Deb.4 P_3	7340.1	0.0019	82.94	208.9	39.36	281.6	19.19	175.1
Chaser and Deb.4 de-orbit	6579.0	0.0007	82.95	179.5	357.7	152.4	32.36	207.5
Debris 5 initial	7352.8	0.0027	82.95	331.0	227.9	85.10	N/A	0.000
Chaser to Deb.5 initial	7352.3	0.0017	82.94	163.2	237.9	84.10	19.19	226.7
Deb.5 P_5	7352.8	0.0033	82.95	163.3	351.2	136.1	226.6	226.6
Chaser to Deb.5 P_5	7352.3	0.0023	82.94	163.4	341.2	135.1	19.13	226.6
Chaser and Deb.5 de-orbit	6579.0	0.0026	82.94	133.8	199.7	219.7	32.76	259.4
Total Time:	N/A	N/A	N/A	N/A	N/A	N/A	259.4	259.4

Table 4.8: Orbital transfer results summary for high fidelity similar inclination band transfers (debris set 3)

nent oscillates around 0 and the θ-component oscillates around 1. This signifies a focus on changing the semi-major axis and little to no change in inclination. The non-zero value of u_h following the first $\sim$4 days is due to the continued change in RAAN required to reach the desired value. It should be noted that the majority of the RAAN change results from perturbations and not the thrust provided by the chaser shown by the RAAN limitation analysis described in Section 3.2.2. The large amplitude of oscillations of the control inputs is a representation of the change in thrust direction required to optimize out-of-plane changes such as inclination and RAAN, during orbital transfers requiring multiple revolutions. The smaller oscillations compensate for small perturbations arising due to Earth oblateness during the orbital transfer. Figure 4.3 shows the true anomaly θ of the chaser and debris 3 during the last three revolutions of the rendezvous, highlighting their convergence at the end of the transfer.

(a)

(b)

Figure 4.1: Chaser orbits for rendezvous with debris 3: (a) Chaser orbits around Earth (b) Chaser start and finish location

4.3 Results Using Point-to-Point Optimal Control
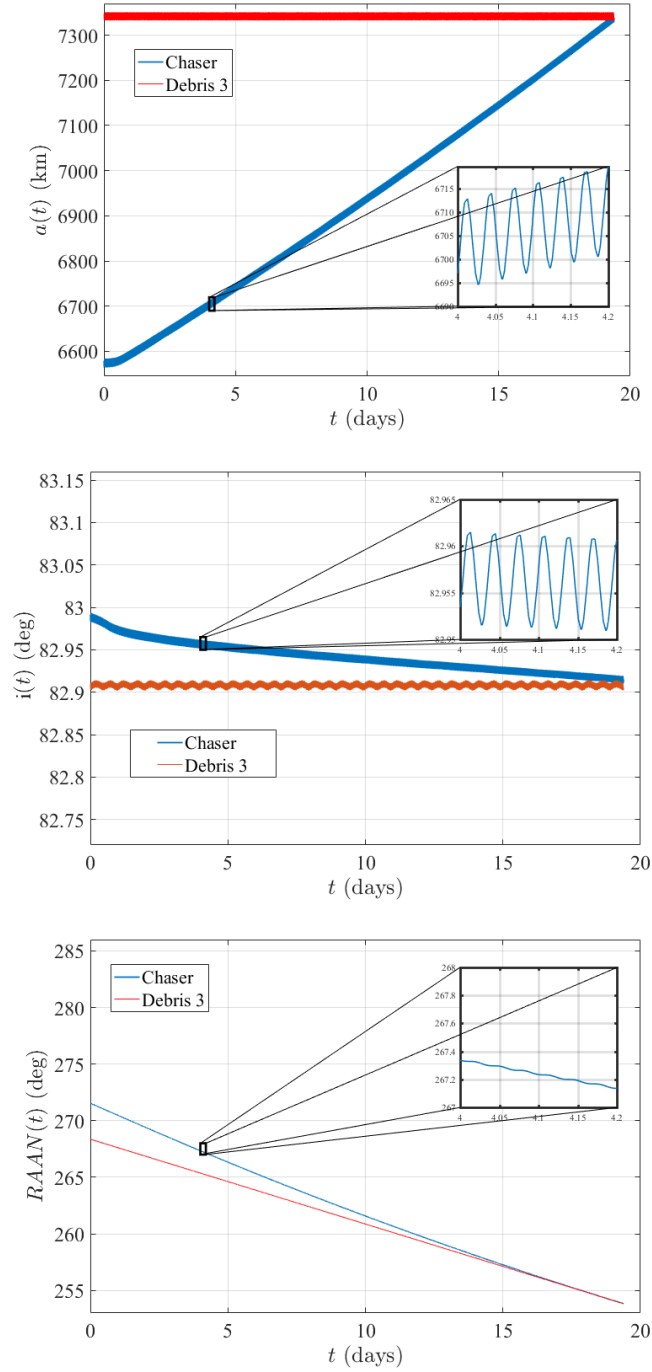
Figure 4.2: Chaser and debris changes in orbital elements during rendezvous with debris 3
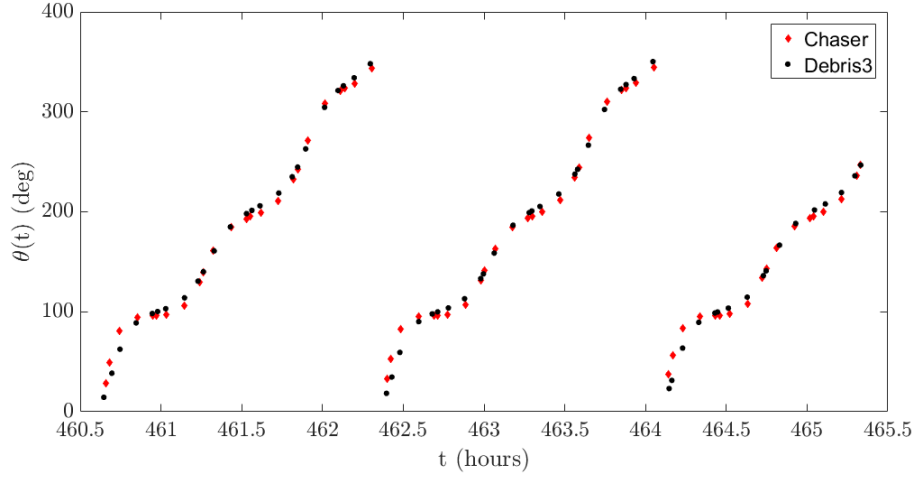
Figure 4.3: Chaser and debris changes in true anomaly for the last three revolutions during rendezvous with debris 3[1]

For debris set 3 (debris in Table 4.7), the most significant contributor to transfer time is the change in semi-major axis, as the change in inclination required is very small. The change in mass due to fuel expenditure during rendezvous and de-orbit are presented in Table 4.11. This change is computed by using Eq. (2.16) and is linear in time due to the constant nature of the thrusting. Therefore, the expected fuel mass required for a single rendezvous is, on average, approximately 85.38 kg and the expected fuel mass requirement for a single de-orbit is, on average, approximately 145.5 kg. The total expected fuel mass requirement for the removal of this debris set is 1154 kg, that is approximately 58% of the total chaser mass and, therefore, a feasible requirement for long range space missions [166]. The total time for rendezvous and de-orbiting five pieces of debris in the similar inclination band is found to be 259.4 days (see Table 4.8). This leaves some time for other aspects of a multi-debris removal mission, such as close range rendezvous and capture of the pieces of debris, as well as releasing the debris. These results suggest that a full five-debris removal mission with debris in similar inclination orbits is achievable within the one year time limit.

---

[1]The reversal in true anomaly is caused by a rapid change in argument of perigee due to near-circular orbits and does not represent the chaser reversing in orbit
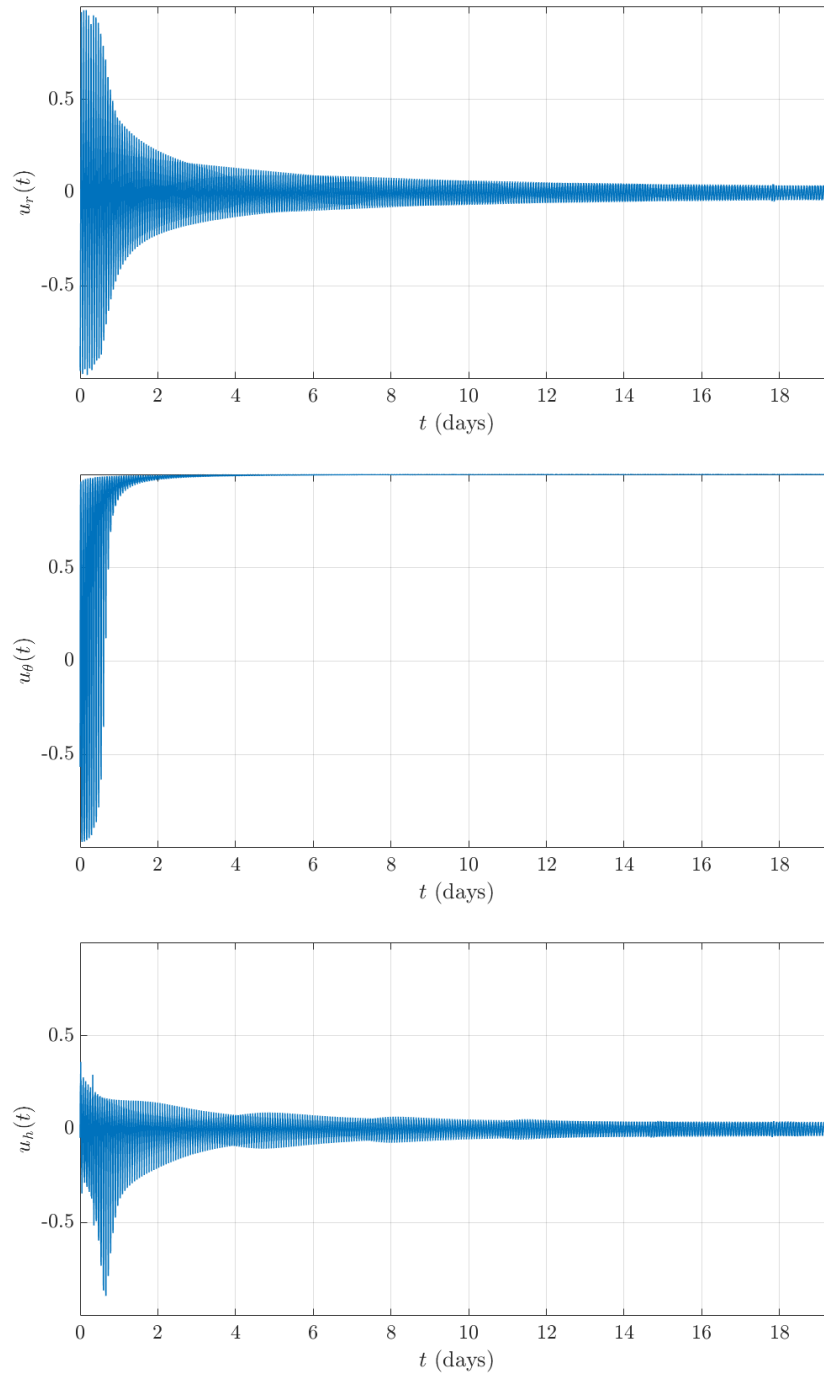
Figure 4.4: Chaser control direction components during rendezvous with debris 3

4.3.2 Large Inclination Change

This set of debris, was chosen to demonstrate a multi-debris mission for debris with larger inclination differences; only two pieces of debris are considered, as large inclination changes require significantly longer transfer times. This scenario is relevant when considering removing multiple "high risk" pieces of debris in a single mission, as these might not be located within a narrow inclination band. The initial locations defined using orbital elements of the two SL-8 rocket bodies in set 4 are shown in Table 4.9. As already noted, the orbits are nearly circular with altitudes between 700 and 1100 km and all pieces of debris have a mass of $\sim$1440 kg. The difference in the inclination of the two debris orbits is $8.94°$.

Name	Norad ID	a (km)	e	i (deg)	Ω (deg)	ω (deg)	θ (deg)
Chaser	N/A	6571	0.0000	74.00	181.0	0.000	0.000
Debris 1	16953	7146	0.0012	74.01	176.6	168.5	2.414
Debris 2	23527	7365	0.0029	82.94	64.92	2.661	13.79

Table 4.9: Debris set 4 and chaser initial locations for large inclination change transfers

A summary of the results for transfers with large inclination changes can be found in Table 4.10. Figure 4.5 illustrates the nature of the path of the chaser during rendezvous with debris 2 and indicates initial and final locations of the chaser for said rendezvous. For this transfer, the chaser requires 1183.5 revolutions around the Earth while the piece of debris revolves 1755.8 times around the Earth, from the start of the mission. The full set of iterative results for this set of debris can be found in Table A.2 in the Appendix.

Transfer Description	a (km)	e	i (deg)	Ω (deg)	ω (deg)	θ (deg)	Time (days)	Total Time (days)
Debris 1 initial	7145.9	0.0012	74.01	176.6	168.5	2.414	N/A	0.000
Chaser to Deb.1 initial	7146.0	0.0016	74.00	151.1	158.5	22.44	14.63	14.63
Deb.1 P_3	7144.1	0.0013	74.01	149.6	169.6	31.7	14.61	14.61
Chaser to Deb.1 P_3	7143.6	0.0009	74.00	149.6	167.5	30.7	14.61	14.61
Chaser and Deb.1 de-orbit	6579.0	0.0009	73.99	100.8	150.9	142.3	23.63	38.24
Debris 2 initial	7365.1	0.0029	82.94	65.92	2.661	13.79	N/A	0.000
Chaser to Deb.2 initial	7365.6	0.0011	82.94	338.9	91.86	13.69	80.12	118.4
Deb.2 P_3	7363.0	0.0030	82.94	339.0	23.62	309.8	117.3	117.3
Chaser to Deb.2 P_3	7362.5	0.0023	82.94	339.1	33.62	308.8	79.07	117.3
Chaser and Deb.2 de-orbit	6579.1	0.0026	82.93	308.6	349.2	46.35	32.40	149.7
Total Time:	N/A	N/A	N/A	N/A	N/A	N/A	149.7	149.7

Table 4.10: Orbital transfer results summary for large inclination change transfers

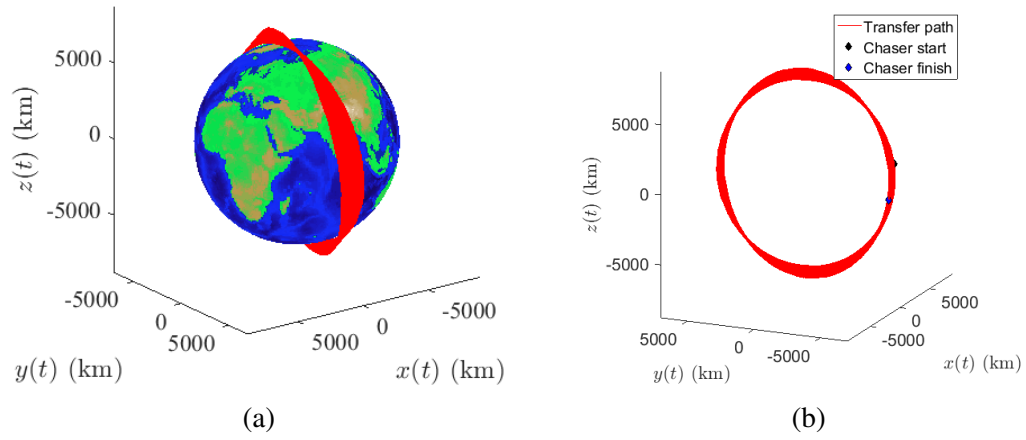The changes in the orbital elements during rendezvous with debris 2 are presented in
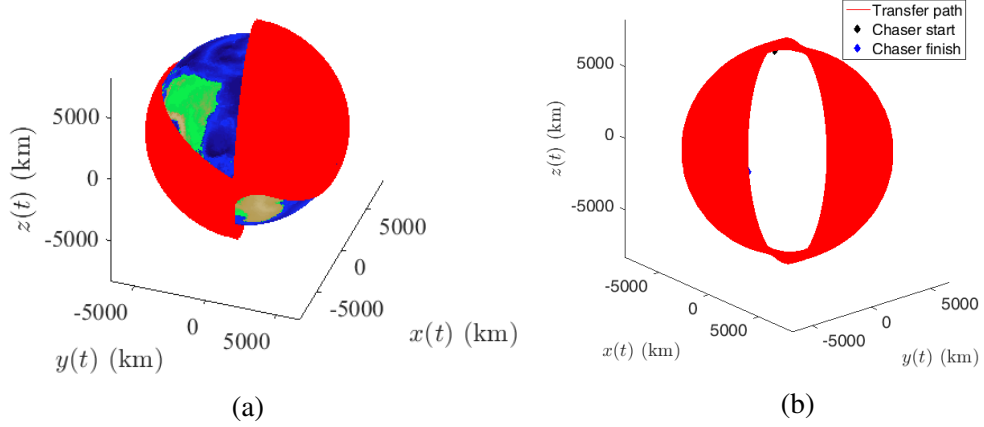
Figure 4.5: Chaser orbits for rendezvous with debris 2: (a) Chaser orbits around Earth (b) Chaser start and finish location

Figures 4.6 and 4.7. The three plots in Figure 4.6 show the progression of semi-major axis, inclination, and RAAN respectively over the course of the transfer for both the chaser and the piece of debris. Due to the much larger inclination change requirement, the transfer now takes significantly longer, which also results in a significantly higher RAAN change, as the effect of drift increases with time. The control direction components in Figure 4.8 are shown as the radial, and θ components of the thrust respectively. The radial component oscillating around 0 is required for changes in eccentricity and argument of perigee, unlike the transfer in set 3 (Section 4.3.1); however, the θ-component fluctuating further from 1 as priority has shifted from semi-major axis to inclination change. The changes in inclination occur throughout the transfer, which is reflected in larger oscillations in u_h during the entire time. In addition, the u_h component also contributes to the continued change in RAAN and inclination required to reach the desired values. The out-of-plane u_h component is not shown, as it is oscillating between approximately -1 and 1 throughout the transfer, filling out the entire plot without providing additional insight. Figure 4.7 shows the true anomaly θ during the last three revolutions of rendezvous between the chaser and debris 2, confirming the convergence at the end of the transfer.

The change in mass due to fuel expenditure during the rendezvous is shown in Table 4.11 (right column). The expected fuel mass required for high inclination change rendezvous is 348.2 kg, which is significantly higher than the 64.4 kg required for the small
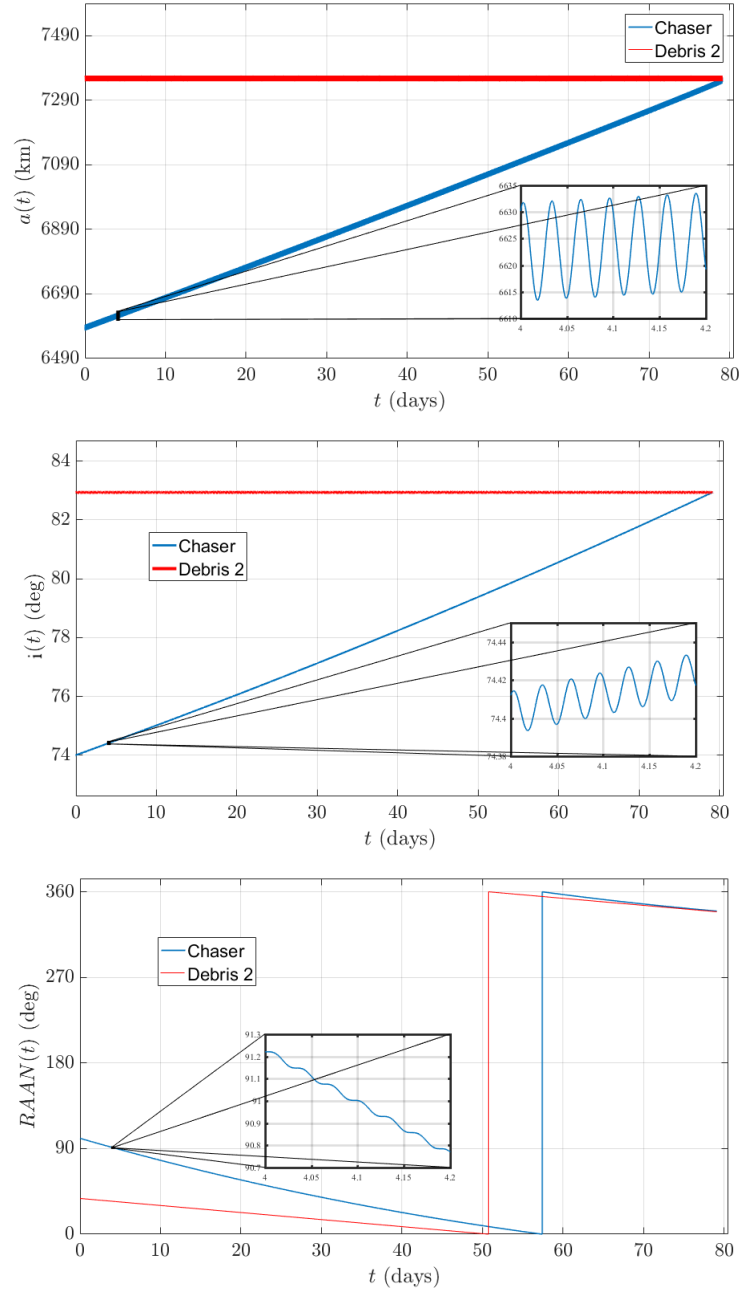
Figure 4.6: Chaser and debris changes in orbital elements during rendezvous with debris 2
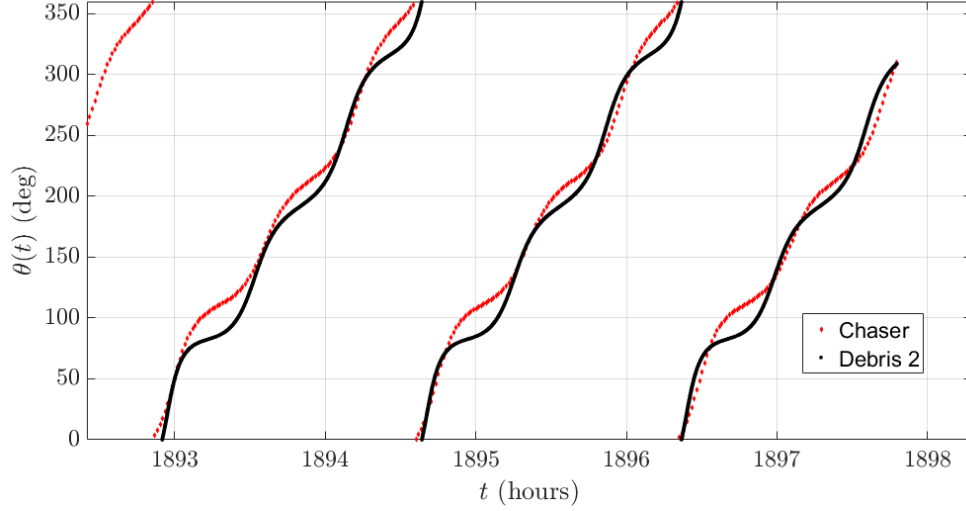
Figure 4.7: Chaser and debris changes true anomaly for the last three revolutions during rendezvous with debris 2

inclination change transfer to debris 1. Now, the total mission fuel mass for the two pieces of debris with large inclination differences is estimated to be 656.8 kg. As a result, only two pieces of debris with inclination differences of this magnitude ($\sim 10°$) can be included in a single mission to maintain a fuel mass 60% or lower of the chaser mass. The total time for rendezvous with and de-orbiting of two pieces of debris is found to be 149.7 days (see Table 4.10). This also shows that if five pieces of debris are to be removed within a year, at most one rendezvous can involve a large inclination change.
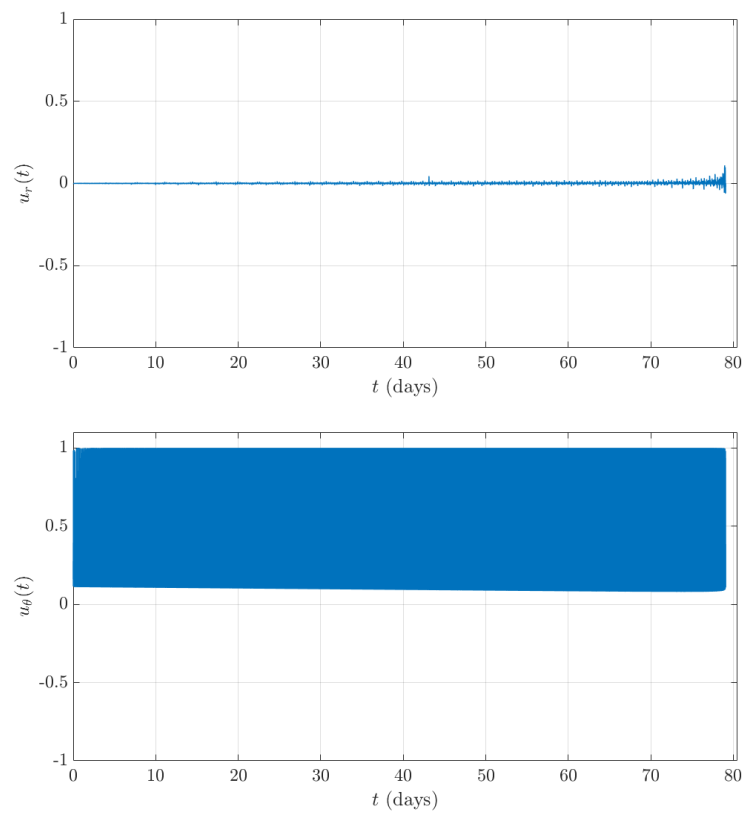
Figure 4.8: Chaser control direction components during rendezvous with debris 2

Transfer	Fuel Mass (kg) - similar inclination band	Fuel Mass (kg) - large inclination changes
Rendezvous 1	88.01	64.40
De-orbit 1	144.9	101.2
Rendezvous 2	84.74	348.2
De-orbit 2	143.2	143.0
Rendezvous 3	85.38	N/A
De-orbit 3	152.5	N/A
Rendezvous 4	84.53	N/A
De-orbit 4	142.5	N/A
Rendezvous 5	84.24	N/A
De-orbit 5	144.3	N/A
Total	1154	656.8

Table 4.11: Fuel mass requirement for each orbital transfer for the debris sets in Sections 4.3.1 and 4.3.2

4.3.3   Drift Orbit Inclusion

The debris of interest for the results presented here are the large defunct satellites and rocket stages with high risk factors presented as debris set 1 in Section 4.3.1. It is important to note that this set of debris was chosen for the purpose of showcasing the solution for the drift orbit within the context of high-accuracy transfers, and it does not necessarily represent a feasible mission. The initial locations of this set of debris is now defined using TLEs generated on the 1st of January 2016 and the orbital elements of the debris on this date and the order in which the debris is removed is shown in Table 4.12. The debris altitudes and inclinations are all in a narrow band around 760 km and 98°; however, the RAAN differences are very large for these debris. Moreover, this particular set of debris have very large masses, which will affect the de-orbiting stage of the debris removal mission. The sequence of the debris is chosen such that consecutive RAAN differences are as low as possible. Other than this, the particular debris choice and sequencing have not been optimized in any way to the specific ADR mission presented here.

A summary of the results for the removal of the 5 debris set can be found in Table 4.13. Each line in the table represents a given stage in the proposed methodology. When propagating debris other than the first one in the sequence, the time taken to rendezvous and de-orbit previous debris also needs to be taken into account, and the propagation time for the debris is therefore cumulative and does not correspond to the chaser transfer time to that

4.3 Results Using Point-to-Point Optimal Control

Name	Norad ID	a (km)	e	i (deg)	Ω (deg)	ω (deg)	θ (deg)	approx. mass (kg)
Chaser	N/A	6578	0.0000	98.00	320.0	0.000	0.000	2000
Zenit-2 stage-2	25400	7185	0.0011	98.41	323.3	57.96	302.2	8226
Daichi	28931	7065	0.0001	97.91	47.76	133.3	226.8	4000
Envisat	27386	7144	0.0001	98.31	60.30	82.82	277.3	8111
H-2A stage-2	27601	7164	0.0073	98.44	80.20	72.97	36.14	4000
Zenit-2 stage-2	27006	7374	0.0014	99.23	154.9	259.7	226.2	9000

Table 4.12: Debris and chaser initial locations of debris set 1 for drift orbit inclusion

debris. Thus, for example, the time indicated in Table 4.13 for Deb.2 P_3 is the time taken to remove debris 1, in addition to the time for the chaser to transfer to the drift orbit associated with debris 2, drift, and then transfer to Deb.2 P_3, as in previous sections. As a result, the later the debris appears in the five debris sequence, the longer it will be propagated. As in all previous results, the chaser is assumed to embark on each consecutive rendezvous immediately after the previous debris is de-orbited. The de-orbit results are calculated using the same methodology as the rendezvous, except only with a constraint on semi-major axis and all the other orbital elements left 'free' for the final disposal orbit. The times taken to de-orbit are long for this debris set (36 to 114 days) due to the combined mass of the debris and the chaser.

As the rendezvous with each debris is of similar nature, a closer look at the specific results for one debris (Figures 4.9 and 4.10) is adequate to provide insights into the chaser transfer response and control inputs of the full set. The three plots in Figure 4.9 show the progression of semi-major axis, inclination, and RAAN respectively over the course of the rendezvous for both the chaser and Debris 2; as can be seen, the orbital elements of the chaser reach the desired (debris) values at the end of the transfer. It should be noted that the importance of the drift orbit can be observed in the RAAN plot as the drift portion of the transfer allows for significant RAAN 'catch up'. The control direction components (u_r, u_θ, u_h) for the point-to-point transfer after the drift orbit (transfer 2) are shown in Figure 4.10. Changes in inclination occur throughout the transfer which is reflected in the oscillations in u_h, as well as the irregularities in u_r and u_θ. u_h oscillates between -1 and 1 to change angle of inclination in the appropriate direction depending on the location of the chaser within the transfer orbit: the u_h plot shown (bottom figure in Figure 4.10) is only a short section of transfer 2 to better highlight these results. In particular, to decrease the

4.3 Results Using Point-to-Point Optimal Control

Transfer Description	a (km)	e	i (deg)	Ω (deg)	ω (deg)	θ (deg)	Time (days)	Fuel Mass (kg)
Chaser to drift 1	6877.6	0.0006	98.64	331.7	144.6	355.9	9.762	42.99
Drift 1	6885.2	0.0016	98.63	332.4	172.7	12.67	0.600	0.000
Deb. 1 P_1	7169.2	0.0008	98.43	341.0	39.54	140.3	18.39	N/A
Drift 1 to Deb. 1 P_1	7168.8	0.0003	98.44	341.0	29.54	139.3	8.030	35.60
Chaser and deb.1 de-orbit	6578.5	0.0002	98.42	61.60	123.8	46.27	77.74	344.6
Deb 1 Total	N/A	N/A	N/A	N/A	N/A	N/A	96.13	423.2
Chaser to drift 2	6878.5	0.0033	102.8	129.1	118.8	170.0	42.87	188.8
Drift 2	6883.7	0.0007	102.8	246.8	112.7	196.1	70.12	0.000
Deb. 2 P_3	7058.8	0.0022	97.91	292.4	220.1	264.6	254.7	N/A
Drift 2 to Deb.2 P_3	7058.4	0.0030	97.90	292.3	214.4	263.6	45.55	200.6
Chaser and deb.2 de-orbit	6574.8	0.0038	97.92	331.7	71.95	267.0	36.17	159.3
Deb.2 Total	N/A	N/A	N/A	N/A	N/A	N/A	194.7	548.7
Chaser to drift 3	6878.2	0.0040	99.74	0.004	14.32	162.4	21.36	94.04
Drift 3	6850.0	0.0059	99.74	10.62	53.92	161.8	8.043	0.000
Deb. 3 P_2	7133.8	0.0084	98.31	30.75	16.54	211.3	340.7	N/A
Drift 3 to Deb.3 P_2	7133.5	0.0082	98.31	30.76	11.08	241.7	20.42	89.93
Chaser and deb.3 de-orbit	6578.5	0.0029	98.32	142.6	34.58	234.7	114.1	502.3
Deb.3 Total	N/A	N/A	N/A	N/A	N/A	N/A	163.9	686.3
Chaser to drift 4	6879.1	0.0022	99.18	159.3	327.5	258.8	13.95	61.43
Drift 4	6871.0	0.0028	99.19	218.9	146.4	291.1	49.00	0.000
Deb. 4 P_2	7169.7	0.0052	98.46	232.5	80.18	120.3	532.6	N/A
Drift 4 to Deb.4 P_2	7169.4	0.0043	98.46	232.4	72.60	119.3	12.58	55.40
Chaser and deb.4 de-orbit	6578.5	0.0041	98.46	275.7	167.5	310.7	43.40	191.1
Deb.4 Total	N/A	N/A	N/A	N/A	N/A	N/A	118.9	307.9
Chaser to drift 5	6880.0	0.0051	102.6	339.8	33.63	78.15	45.64	201.0
Drift 5	6886.4	0.0032	102.6	59.32	271.6	314.6	48.10	0.000
Deb. 5 P_3	7385.1	0.0024	99.23	112.7	27.89	12.45	707.6	N/A
Drift 5 to Deb.5 P_3	7384.7	0.0018	99.24	112.5	21.98	12.38	37.24	166.6
Chaser and deb.5 de-orbit	6578.9	0.0016	99.24	215.0	236.3	74.35	106.0	466.9
Deb.5 Total	N/A	N/A	N/A	N/A	N/A	N/A	237.0	834.4
Mission Total:	N/A	N/A	N/A	N/A	N/A	N/A	813.6	2800.5

Table 4.13: Rendezvous transfer results summary — each line of data corresponds to the end of transfer described on that line

inclination, u_h is +1 near apoapsis and -1 near periapsis. Moreover, the radial component oscillates around 0, as no change in eccentricity is required. The θ-component oscillates between 0 and 1. This signifies a focus on changing the semi-major axis while still achieving the desired inclination change. It should be noted that the majority of the RAAN change results from natural (J_2) perturbations and not the thrust provided by the chaser, as shown by the RAAN limitation analysis described in Section 3.2.2. The large amplitude of oscillations of the control inputs is a representation of the change in thrust direction required to optimize out-of-plane changes such as inclination and RAAN, during orbital transfers requiring multiple revolutions. The smaller oscillations compensate for small perturbations arising due to Earth oblateness during the orbital transfer.
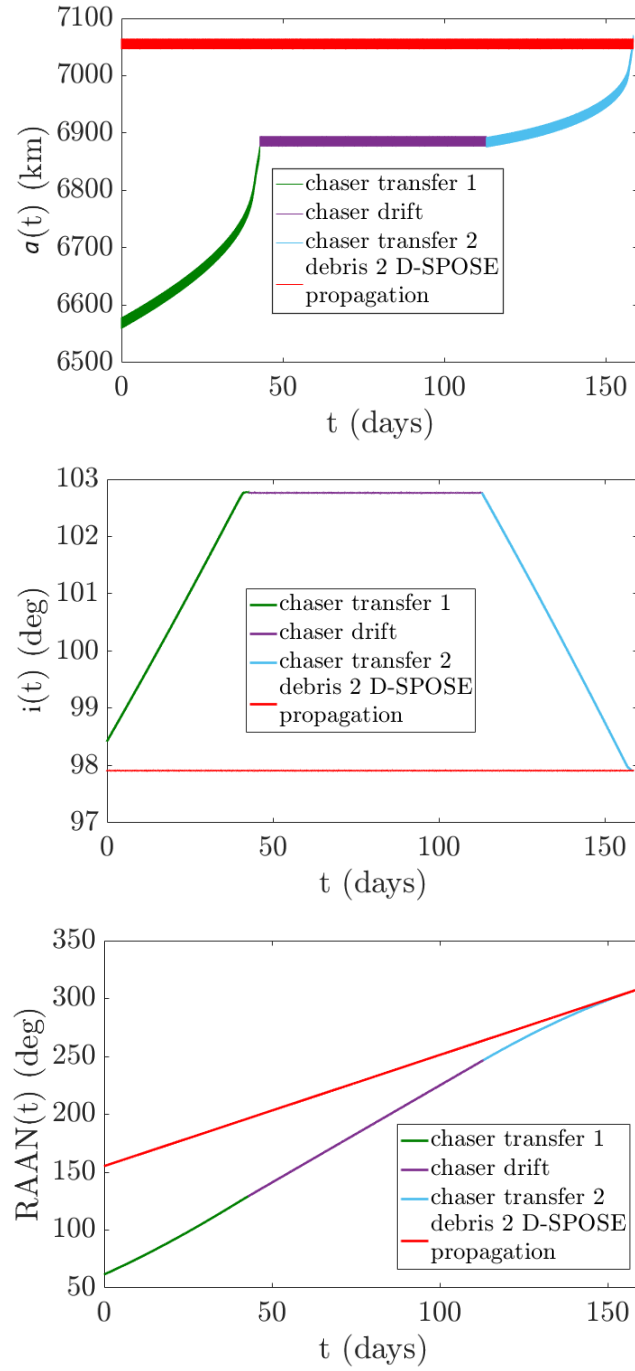
Figure 4.9: Main orbital elements during rendezvous with debris 2

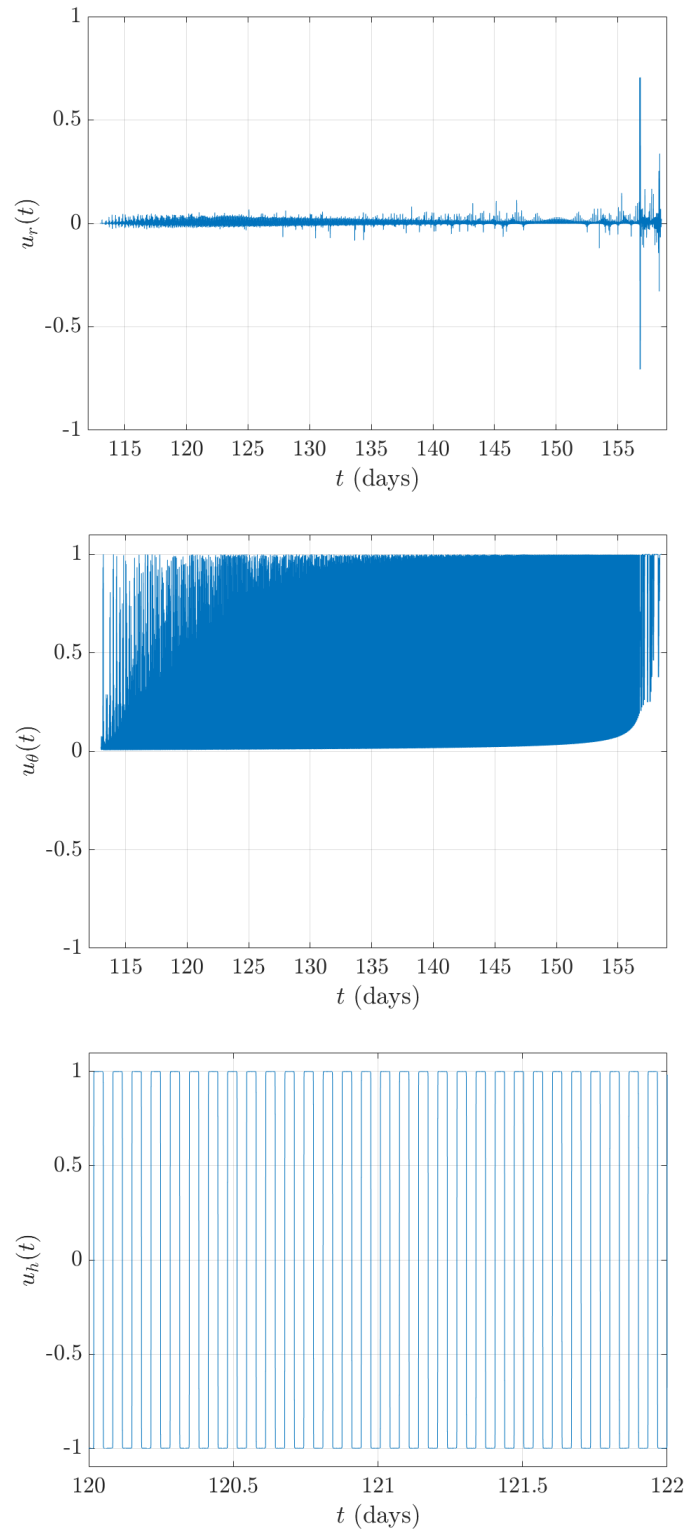Figure 4.10: Chaser control direction components during transfer 2 of the rendezvous with debris 2

For the debris considered in this scenario, the most significant contributor to rendezvous transfer time is the change in RAAN, as the focus is on debris with large RAAN differences. The large RAAN changes required result in higher inclination drift orbits, as a higher inclination (in the band around 98°) results in a higher drift rate, which also contributes to the time of transfer. The total time for rendezvous with and de-orbiting five pieces of debris is found to be 813.6 days (see Table 4.13). It is important to note that some time needs to be allocated for other aspects of a multi-debris removal mission, such as close-range rendezvous and capture of the debris, as well as releasing the debris. These results suggest that a full five-debris removal mission with massive debris in orbits with large differences in RAAN is not achievable within one-year time frame. It should also be noted that a main contributor to mission time is the long de-orbit time, due to the large masses of the debris showcased here. Furthermore, de-orbiting all five debris considered in this set requires significantly more fuel than is reasonable for a 2000 kg chaser: 2801 kg as per results in Table 4.13. Nevertheless, the proposed optimization framework is capable of assessing the costs of removing any set of debris regardless of the RAAN changes required to rendezvous with each piece of debris in the set.

4.4   Chapter Summary

In this chapter, several case studies are presented where various debris sets based on TLE data are used to implement the approaches outlined in Chapter 3 in order to solve the motion planning problem for a given multiple debris removal mission. The nominal mission goal in showcasing the different approaches is to achieve removal of five debris in a one-year time frame. Each case study has a defining characteristic in terms of the debris considered. These characteristics are: high risk, similar inclination band, large inclination differences, and RAAN differences requiring a drift orbit. For each case study, results are presented in the form of mission time and fuel mass requirements, and, for the point-to-point formulation only, the control inputs (thrust directions) required to achieve each transfer.

The purpose of the first part of this chapter is to demonstrate and compare the recursive and mothership approaches to multiple debris removal. The recursive approach contains various novel elements and as such the second part of this chapter demonstrates the point-to point formulation applied to recursive multiple debris removal for debris sets akin to

4.4 Chapter Summary

those analyzed using the lower fidelity approaches. A number of debris sets with various defining characteristics are used as inputs to the high fidelity formulation to highlight the scope in which it can be used to analyze, design, and plan multiple ADR missions.

Release and Re-entry

Once the debris is de-orbited to a disposal orbit, assumed at 200 km altitude above Earth, it is released and will passively re-enter the Earth's atmosphere. The focus of this chapter is to analyze the re-entry phase of the debris removal mission. Specifically, two existing re-entry models, the Debris Risk Assessment and Mitigation Analysis (DRAMA) model, developed by the European Space Agency (ESA), and the Debris Assessment Software (DAS), developed by the National Aeronautics and Space Administration (NASA), are used to study the influences of varying the parameters of the disposal orbit and the release conditions on the resultant casualty risk factor. The goal here is to identify specific desirable disposal orbit characteristics that can be used as boundary conditions for the de-orbit manoeuvre using the formulation presented in Section 3.6.

In broad terms, the casualty risk factor P_c, the principal parameter calculated by both DRAMA and DAS, is dependent on the impact probability P_i, the average population density ρ_p, and the casualty area A_c, as defined in the following equation:

$$P_c = P_i \cdot \rho_p \cdot A_c \qquad (5.1)$$

The impact probability P_i is the probability that a surviving fragment impacts a specific location on Earth. For the different re-entry types (uncontrolled and controlled), the impact location is calculated differently. For uncontrolled re-entry, the predicted impact location is given as a latitude range only, whereas for the controlled re-entry, the predicted impact location is given as specific location in terms of a latitude and a longitude value. For the

analysis performed as part of this thesis, only uncontrolled re-entries will be considered; in this case, the impact location is dependent on the initial location of debris, which is the point of release, and the propagation of the debris until it reaches the Earth's surface or a point of demise. The average population density varies significantly with latitude band, meaning the specific impact location affects the value of the population density in Eq. (5.1). The casualty area A_c is a function of the debris impact cross-section A_i and the vertical projection area of a standing human A_h, and is computed from:

$$A_c = \left(\sqrt{A_h} + \sqrt{A_i} \right)^2 \tag{5.2}$$

The definition of the casualty risk factor, as per Eq. (5.1), is the same for the two pieces of software (DRAMA and DAS) used to analyze re-entry for this research. The casualty risk factor value is an internationally recognized metric used to assess the suitability of space debris re-entry and whether the specific re-entry is deemed too high-risk, by comparison with the acceptable value of 1e-4 [23].

With this perspective, the de-orbiting stage of an active debris removal mission can be designed such that the parameters of the disposal orbit minimize the casualty risk of large debris re-entry, while maintaining feasible fuel and time constraints on the de-orbit manoeuvre. With respect to release conditions, the effect of introducing a small-magnitude impulse onto the debris at the release is studied in Section 5.3, consequently showing that the casualty risk factor can be lowered even further. The change in the risk factor that results from an impulse is highly dependent on both the magnitude and the direction of the impulse with respect to the debris flight path. Furthermore, it has previously been demonstrated that the orientation and surface area of a piece of debris at the onset of re-entry have a significant impact on the characteristics of the re-entry. To this end, in Section 5.4 D-SPOSE is used to analyze the rotational state evolution of the debris between its release at ∼200 km and the onset of re-entry assumed at ∼125 km altitude. The debris is released with various attitude orientations, and the implications of the attitude state during descent on the DRAMA re-entry analysis are discussed.

5.1   DRAMA vs. DAS Comparison

In order to properly define the re-entry analysis presented in this chapter, Sections 5.1.1 and 5.1.2 detail additional aspects of the re-entry software, building on their general introduction in Section 2.3.3. This is followed by a comparative analysis between the two software suites and lastly the full re-entry analysis and the results. In the two models, the onset of re-entry is considered to occur at 125 km altitude, and this will be referred to as the *re-entry orbit* throughout this chapter. The time taken for the debris to reach the re-entry orbit from the initial (disposal) orbit, without any external control, is approximately 21 hours, while the time for the debris to reach Earth's surface from the re-entry orbit is approximately one hour.

5.1.1   DRAMA

As already noted in Section 2.3.3, DRAMA includes the SARA re-entry tool, which in turn contains two components SESAM and SERAM, as previously mentioned. The functionalities of these components are described as follows:

SESAM takes an object oriented approach, considering simplified shapes (cuboids, cylinders, spheres, etc.) to define the geometry of the various debris components that make up the debris itself for the re-entry analysis. Here, object-oriented relates to the fact that SESAM simulates the demise individually per object after they have been released from the parent body. Furthermore, a materials database is used to define the material properties of the various debris components. During propagation, the equations of motion are integrated numerically by an error controlled, variable step size 4/5 Runge-Kutta method. Only translational degrees-of-freedom are propagated, and as such, only position and velocity are considered as state vector for the integration. In addition, the thermal analysis and the dynamics are coupled, meaning that, mass losses due to thermal degradation are considered during the trajectory propagation. Specifically, the aerothermodynamic model distinguishes between the three flow regimes: free molecular, transition and continuum, which determine the heating rate of the debris material (selected from an embedded materials database)[150]. Furthermore, the model computes the drag, lift and side force coefficients for the debris as a function of its shape, dimensions, attitude and the flight conditions

99

5.1 DRAMA vs. DAS Comparison

(Mach and Knudsen number). These values are then used to compute the heat flux which in turn is used to compute the aerodynamic effects of the atmosphere on the debris. The atmospheric model consists of look-up tables used to define atmospheric properties such as air density and winds as a function of altitude. Although only trajectory of the debris is propagated, different attitude modes can be specified for the debris: randomly tumbling, and, fixed attitude, which in turn determine the effective cross-sectional area and thereby the aerodynamic coefficients of the debris. For each fragment shape, drag, lift and side force coefficients are computed as a combination of the primitives composing the fragment, and the fragment's impact velocity is calculated based on the trajectory propagation. Finally, the output includes the aerothermal effects on the debris in terms of mass change and break-up/demise events, i.e., survivability, as well as the trajectory output, including an impact location prediction and the cross-sectional area at impact A_i for each fragment that reaches the surface of Earth.

SERAM is the risk assessment module of SARA, which allows the user to predict the threat of re-entering objects from space to the human population on the ground. SERAM evaluates each term in Eq. (5.1). The values used for the population density are obtained from the UN gridded population of the world (UNGPW) population data as well as the UN World Population Prospects (UNWPP). Given an uncontrolled re-entry, DRAMA offers two settings for determining the impact probability P_i. The first is "latitude band limited" where the latitude band at the specific impact location, found using SESAM survivability analysis, fixes the impact probability for surviving debris to 1 at the impact latitude and 0 for all other latitudes ($\phi = \phi_i \rightarrow P_i = 1$, $\phi \neq \phi_i \rightarrow P_i = 0$). The mean population density at this latitude is then used for the latitude band limited casualty calculation. The second setting is "near-circular/circular" re-entry, where the impact probability of a fragment, given as the probability that this fragment impacts in a certain location, is a distribution over the latitude range of the ground track of the fragment orbit from the onset of re-entry (~ 125 km altitude). For circular re-entry, the impact probability in a certain latitude band $\Delta\phi$ is calculated as a function of inclination i, latitude ϕ, and latitude band size $\Delta\phi$ using Eq. (5.3):

$$P_i(i, \phi, \Delta\phi) = \frac{1}{\pi}\left[\arcsin\left(\frac{\sin(\phi + \frac{\Delta\phi}{2})}{\sin(i)}\right) - \arcsin\left(\frac{\sin(\phi - \frac{\Delta\phi}{2})}{\sin(i)}\right)\right] \quad (5.3)$$

5.1 DRAMA vs. DAS Comparison

The impact probability, found using Eq. (5.3), is summed over different values of ϕ along the entirety of the re-entry orbit ground track. As such, no specific impact location is found when using the circular re-entry setting. The latitude band size $\Delta\phi$ is pre-set by SERAM and is defined by the pixel boundaries of the data from the UNGWP within which the population count is read and used to compute the population density ρ_p. The singularity in Eq. (5.3) at $i = 0$ is accounted for by assuming the impact will occur only in the equatorial latitude band. For both latitude band limited and circular re-entry, the population data is extracted from the population count GeoTIFF [1], obtained from the UNGPW, where the population count for a certain pixel on the world map is read. For a given pixel, the corresponding latitudes can be determined for the upper and lower border of the pixel. From these pixel border latitudes, a mean latitude for the pixel centre can be calculated and used to determine the local Earth radius for this latitude bin, which in turn is used to compute the pixel area. The population density ρ_p is a function of the population count of a pixel and the area of that pixel [150].

Furthermore, the circular re-entry risk factor only varies significantly with initial orbit inclination (out of all the orbital parameters) because, in this case, P_i only depends on i; however, for latitude band limited re-entry, there are significant changes in casualty risk factor which are dependent on the eccentricity, inclination, RAAN, argument of perigee, and the true anomaly of the debris when released in the initial orbit. It should be noted that the inclination at 125 km (re-entry orbit) does not differ significantly from the inclination of the initial orbit, i.e., at 200 km altitude. Lastly, the casualty area is calculated as in Eq. (5.2), with A_h taken as $0.36 m^2$, and the impact cross-section A_i calculated using SESAM. The SESAM-SERAM interaction is illustrated in Figure 5.1. It is important to note that it is possible to run the SERAM risk analysis without using SESAM. In this case, SERAM does not use aerothermal coefficients, only a list of fragments/objects assumed to have reached ground, which are then used to calculate the resulting casualty risk factor.

---

[1]GeoTIFF is a public domain metadata standard which allows georeferencing information to be embedded within a TIFF file
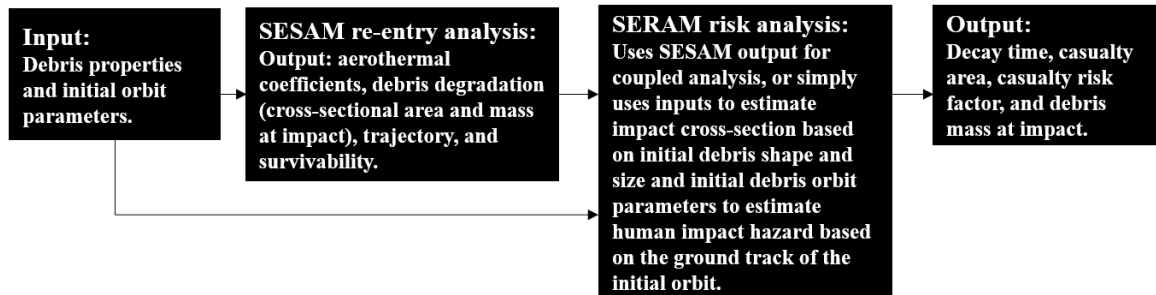
Figure 5.1: SESAM-SERAM component interaction in DRAMA

5.1.2 DAS

In DAS, the debris is defined in much the same way, as in the SARA re-entry tool of DRAMA, in terms of geometric shape and dimensions, mass, and material properties. A materials database is also included within DAS. For thermal analysis in DAS, degradation of the debris is considered as a binary outcome, which means the debris casualty area for an object is either 0 (demised) or a function of the initial debris dimensions. Demise is defined in DAS as the total destruction of a re-entering object, caused mainly by frictional heating with the atmosphere. Therefore, the debris will only be considered as demised if the external forces experienced during re-entry completely destroy (dimensions tend to zero) the debris, given its material properties. DAS is not able to predict partial melting or fragmentation; this in turn yields a more conservative risk assessment, as DRAMA includes a 15 J kinetic energy uncritical threshold. This threshold means that a piece of re-entering debris is considered uncritical (no risk) if it's kinetic energy drops below 15 J. The required input for risk analysis for DAS in terms of initial orbital parameters is only the altitude, eccentricity, and inclination, as opposed to the full set of six elements required by SARA. The main output of the re-entry analysis using DAS is the resulting demise altitudes or the calculated casualty areas for each ground impacting object, as well as the risk factor. Using DAS, the casualty risk factor of Eq. (5.1), is formulated the same as in DRAMA; however, with a simplified impact area calculation, and an impact probability based on the ground track of the re-entry orbit and the statistical population density for locations along

that ground track. A summary of the DAS analysis procedure is illustrated in Figure 5.2.
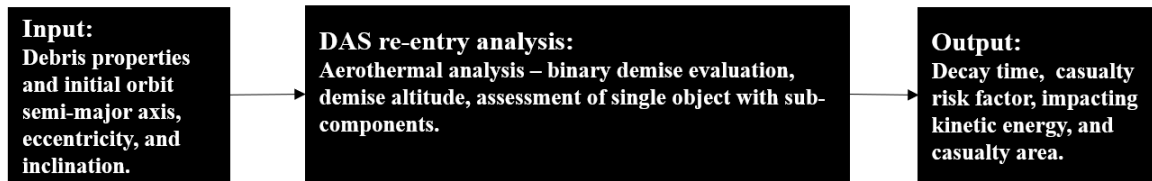

Figure 5.2: Re-entry analysis in DAS

5.1.3   DRAMA vs. DAS Case Study

To compare the output of DAS to the output of DRAMA, a re-entry scenario is considered and analyzed using both software suites. As noted earlier, for DAS, the initial conditions for the re-entry analysis can only be specified in terms of fixed values of semi-major axis (6571 km), eccentricity (0.004), and inclination (83°). The debris geometry and mass are defined as in DRAMA. All common initial conditions for this comparative study are presented in Table 5.1. The piece of debris considered is an SL-8 rocket body similar to the debris sets considered for the orbital transfer case studies in Section 4.3.1.

Given these conditions, the results of the analysis using DAS are summarized in Table 5.2. Because DRAMA takes into account all six orbital parameters, batch simulations (as part of the Monte Carlo module in DRAMA) were carried out. The RAAN and the true anomaly were varied from 0° to 360° in steps of 10°, and the mean risk factor was found for direct comparison to the DAS results. Changing the argument of perigee was not considered for these near-circular orbits given that, at near-zero eccentricity, changing argument of perigee is effectively the same as changing the true anomaly. A summary of the DRAMA results, for both latitude band limited and circular re-entry settings, can be found in Table 5.3. Comparing the results in Tables 5.2 and 5.3, it is evident that the two software produce similar results for the re-entry case considered: the risk factors are 2.6e-4 from DAS, 2.5e-4 and 2.2e-4 from DRAMA for the two re-entry types, respectively. Consistently, the average casualty risk and area predicted by DRAMA are slightly lower for both re-entry types (latitude band limited and circular), which suggests that DAS takes a more conservative

approach, as mentioned previously. The risk factor for the circular re-entry setting does not vary with RAAN or true anomaly, and therefore renders a histogram of these results redundant. DRAMA allows for a much higher degree of user input, making it a much more appropriate choice for further analysis. As such, for the remainder of this chapter, DRAMA will be used as the re-entry model of choice.
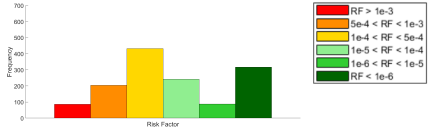
Debris Type	Mass (kg)	Material	Shape	Dimensions (m)	a (km)	e	I (deg)
SL-8 rocket body	1440	AA7075	Cylinder	Length = 6.6, Diameter = 2.4	6571	0.004	83

Table 5.1: Fixed debris and initial orbit parameters for DAS vs. DRAMA comparison

Decay time (yr)	Casualty Area (m^2)	Human Casualty Risk
0.005	20.98	1:3800 (2.6e-4)

Table 5.2: DAS output for re-entry of SL-8 rocket body of Table 5.1

Re-entry type	Decay time (yr)	Casualty Area (m^2)	Human Casualty Risk
Latitude band limited	0.005	19.66	Mean risk: 2.5e-4
Circular	0.005	19.66	2.2e-4

Table 5.3: DRAMA output for re-entry of SL-8 rocket body of Table 5.1

5.2 Orbital Parameters of Release Orbit

The focus of the research presented in this section is assessing and mitigating the risk of uncontrolled re-entry of large debris. One key distinction from regular uncontrolled re-entries is made given that the parameters of the debris in terms of orbit and attitude at approximately 200 km altitude, which were previously unknown as the debris orbits for years prior to re-entry, can be tailored to the specific re-entry as a result of ADR. As such, the parameters of the disposal orbit in Figure 3.2, henceforth referred to as the *initial orbit*,

5.2 Orbital Parameters of Release Orbit

in which the debris is released, are varied, and the resultant effect on the on-ground risk factor is calculated using the previously mentioned re-entry model, DRAMA [150, 151] introduced in Section 2.3.3.

The aim of the following analysis is to investigate the effect on the debris re-entry risk of the initial orbital parameters of the debris, at the point of release. As such, the goal is to identify any parameter patterns or regions in parameter space resulting in a reduction of casualty risk factor. Using DRAMA, the fixed initial conditions for re-entry are defined according to Table 5.1, with the exceptions that the eccentricity is not fixed and five different RAAN values are chosen for this investigation. Moreover, the debris is assumed to be "randomly tumbling" during re-entry, which is a setting that determines the cross-sectional area of the debris, and thereby the drag coefficients and impact area. According to the ESA Space Debris Mitigation Compliance Verification Guidelines [167], the average impact area of simple shapes, such as a cylinder, is given by the total surface area at impact divided by four. The effect on debris re-entry of the attitude state of the debris is further analyzed in Section 5.4.

The results shown in Figures 5.3a-5.3e illustrate the risk factors and frequencies of certain risk factor bands for various batch simulations using the Monte Carlo module in DRAMA, with latitude band limited re-entry. Given the previously mentioned 21 hour time between debris release and debris impact, longitude averaging can be justified and therefore makes latitude-band limited uncontrolled re-entry a reasonable assumption. The parameters — eccentricity (0.0001 - 0.005) and true anomaly (0° - 360°) — are varied to investigate their effect on the risk factor. Low eccentricity values are considered as they constitute the eccentricity of the vast majority of SL-8 rocket bodies in LEO [12]. Given near-zero eccentricities, changes in argument of perigee are equivalent to changes in true anomaly. It should be noted that the results for a larger eccentricity range (0.0001-0.029) yield similar risk factor statistics. Five values of RAAN are employed (319°, 275°, 225°, 180°, and 134° corresponding to the five figures according to the RAAN of disposal orbits previously considered in Section 4.3.1. Results found using the circular re-entry setting are also displayed in Table 5.4. Recall, using the circular re-entry setting means that the risk factor results do not vary with RAAN, nor with the true anomaly or eccentricity; however, the mean surviving mass does show a dependence on the RAAN of the initial orbit (see last

column of Table 5.4).

The results for latitude band limited re-entry (Table 5.4 and Figures 5.3a-5.3e) show a wide range of risk factors across all variations of initial orbit RAAN, eccentricity, and true anomaly. There is a general trend of a large number of re-entries with very low risk (RF < 1e-6), which correspond to impact bands with little to no population density and therefore near zero risk. This is confirmed by cross-referencing with the latitude band of these impact locations as shown in Figure 5.4b. All impact locations for the 319° RAAN case corresponding to the scatter plot (right sub-figure) in Figure 5.3a are shown in Figure 5.4a. From the scatter plots (right subfigures in Figure 5.3), it is clear that no distinct patterns emerge when varying eccentricity and true anomaly. However, the majority of low risk re-entries (green) occur at lower eccentricities of the range considered across all values of RAAN. It is also evident from the histogram plots in Figures 5.3a-5.3e that the risk factor distribution and the mean risk factor are consistent despite variation in RAAN. These results also show that a significant number of re-entries have an associated risk factor >10e-4, the minimal acceptable value, but again, no clear trends as to which values of eccentricity and true anomaly result in these high-risk re-entries (yellow-orange-red bars and dots). These results provide an indication of the volatility of the risk factor as a function of the initial orbital parameters of the debris; a small change in the initial orbital elements can lead to orders of magnitude change in the risk factor. Given that there is little variation in the mean casualty area and mean survival mass of the debris upon impact, the volatility is caused by the large variation in impact locations of the debris and consequently a large variation in the population density value, for different sets of initial orbit parameters.

One way to get a handle on the risk factor, despite the large variations, is to look at the mean value for a given batch or by considering circular re-entry results, where the impact probability is found across all latitude bands crossed by the ground track of the debris, the track being dependent on the inclination of the debris orbit at the onset of the re-entry only. The risk factor for circular re-entry only varies with initial orbit inclination; however, orbit inclination changes are costly (in terms of fuel) to achieve in the de-orbiting phase of the mission. It is noted that the risk factor predicted with the circular re-entry setting of DRAMA is approximately 20% lower than the risk factors computed with the latitude band limited setting (see Table 5.4). Interestingly, the circular re-entry results show a variation

of the mean surviving mass value with RAAN; however, these values mostly fall within the standard deviation of the surviving mass results found using the latitude band limited re-entry. Although the debris mass is not directly included in the calculation of the risk factor (Eq. (5.1)) in DRAMA, it is worth noting that the aerothermal effects causing this mass reduction may lead to a significant reduction in surface area and break up of debris with more complex shapes, different material compositions, or appendages [168].

Effectively, the initial orbit parameters significantly influence the predicted impact location of the debris on the surface of Earth. However, this predicted location is subject to large uncertainty, which in turn makes the specific risk factor for one particular set of initial orbit parameters uncertain as well. The unpredictable nature of Earth's atmosphere and the large variation in impact location it causes, further exemplifies the uncertainty associated with using the casualty risk factor as a determining metric for space debris re-entry analysis, as population density at the point of impact is such a significant factor. Using a ground track averaged impact location (circular setting) reduces the risk factor dependence on the initial orbit parameters to a simple dependence on initial orbit inclination, and in turn removes uncertainties associated with impact location, at the expense of accurately determining the casualty risk factor.

Re-entry type	RAAN (deg)	Mean Risk Factor	Mean Casualty Area (m^2)	Mean Surviving Mass (kg)
Latitude band limited	319	2.7e-4 (see Figure 5.3a)	19.7	240 ± 39
Circular	319	2.2e-4	19.7	206
Latitude band limited	275	2.7e-4 (see Figure 5.3b)	19.7	241 ± 39
Circular	275	2.2e-4	19.7	254
Latitude band limited	225	2.8e-4 (see Figure 5.3c)	19.7	241 ± 38
Circular	225	2.2e-4	19.7	197
Latitude band limited	180	2.7e-4 (see Figure 5.3d)	19.7	242 ± 39
Circular	180	2.2e-4	19.7	269
Latitude band limited	134	2.9e-4 (see Figure 5.3e)	19.7	239 ± 39
Circular	134	2.2e-4	19.7	236

Table 5.4: Summary of DRAMA results
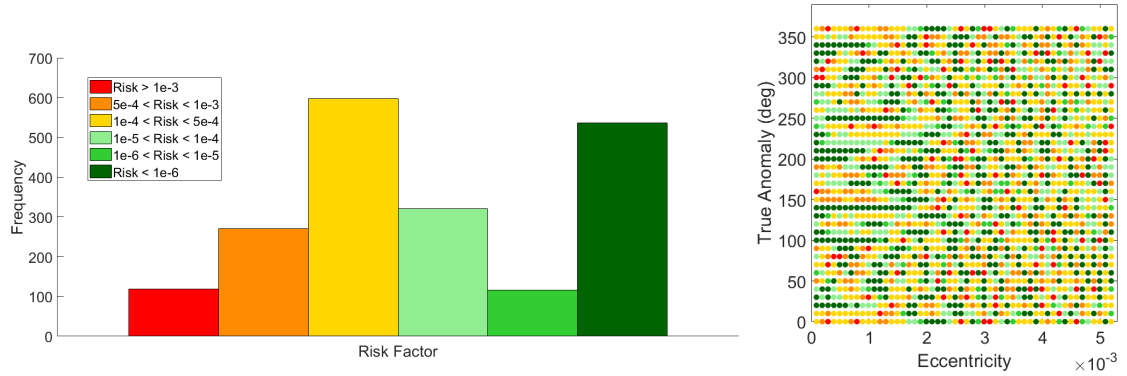
(a) 319° RAAN initial orbit
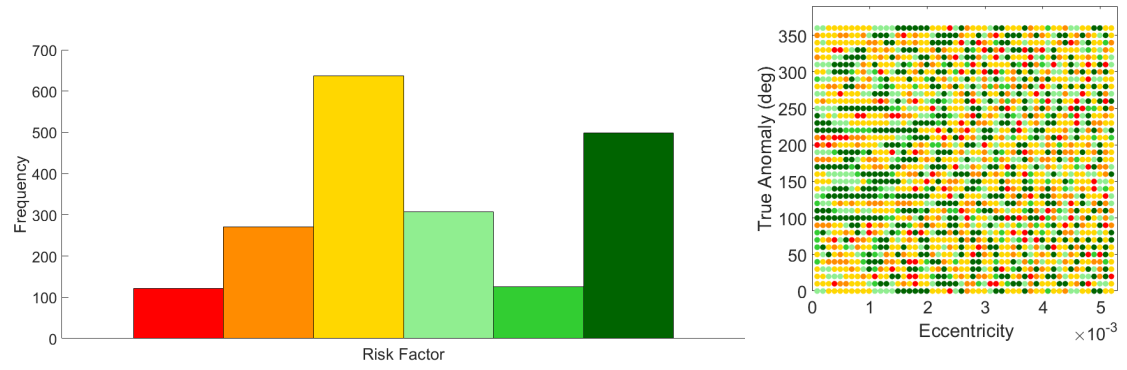
(b) 275° RAAN initial orbit
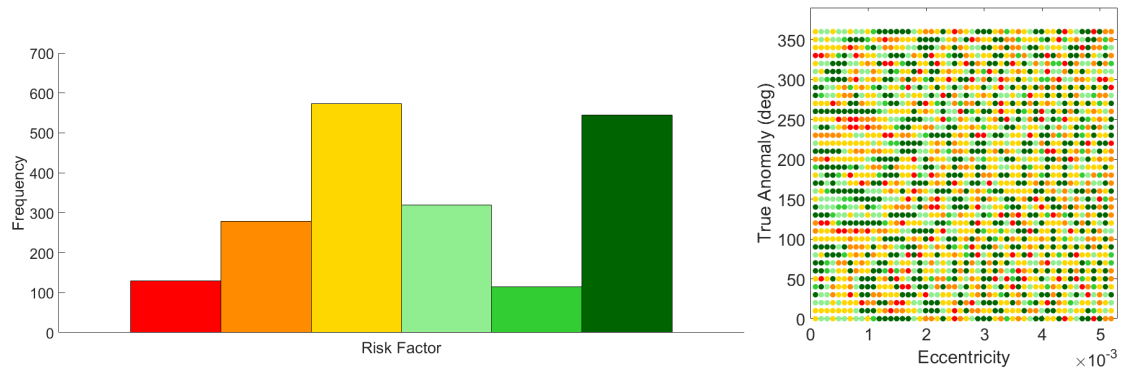
(c) 225° RAAN initial orbit

Figure 5.3: Risk factor distribution for latitude band limited re-entry
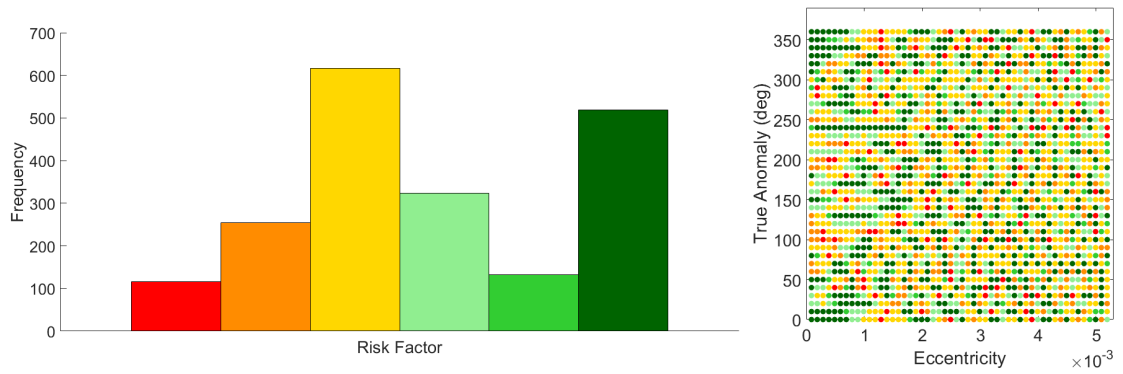
(d) 180° RAAN initial orbit
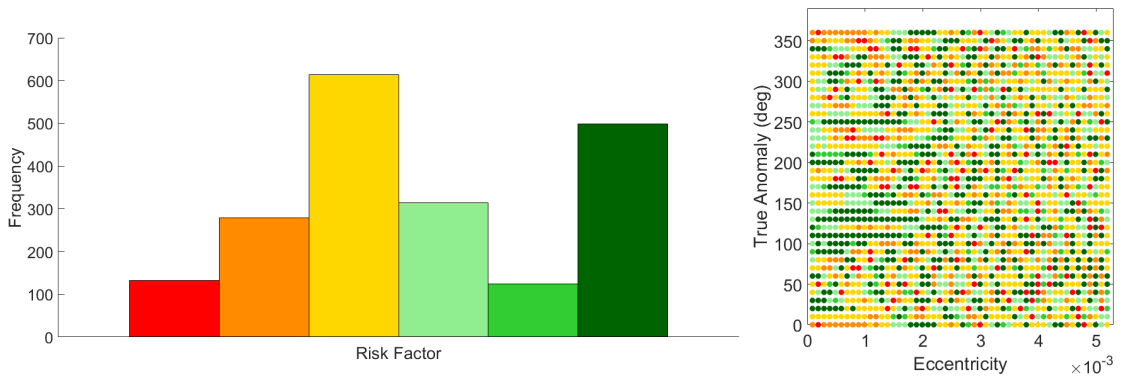
(e) 134° RAAN initial orbit

Figure 5.3: Risk factor distribution for latitude band limited re-entry (cont.)
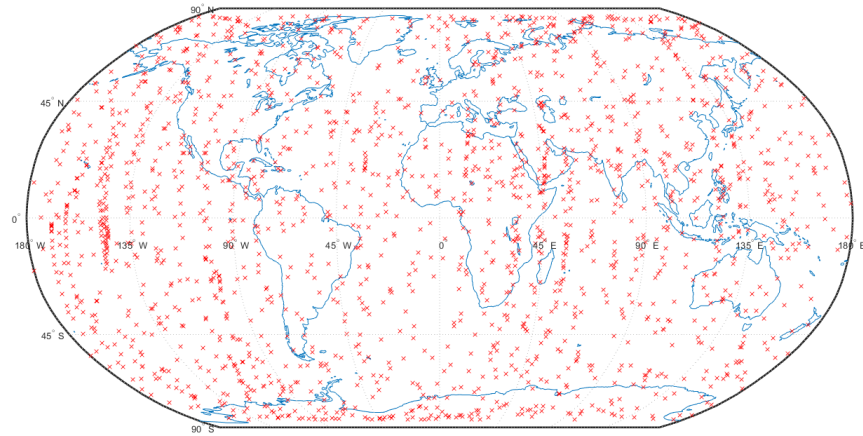
(a) All impact locations
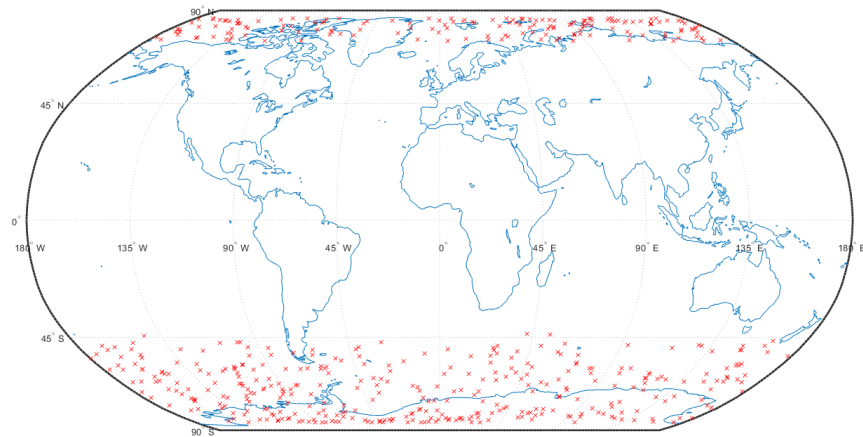
(b) Low risk (RF < 10e-6) impact locations

Figure 5.4: Impact locations for eccentricity vs. true anomaly at 319 RAAN

5.3   Debris Release Impulse

In this section, a small impulse is introduced onto the debris upon release at the initial orbit
and our objective is to quantify the effect this has on the risk factor. This may lead to viable
options to mitigate the adverse effects of space debris re-entry within the constraints of the
proposed ADR mission, hypothesising that an impulse in a specific direction relative to

the centre of mass of the debris will alter the impact location of the debris and hence the risk factor. Ideally, the impulse magnitude and direction can be chosen such that the risk of re-entry is reduced, resulting in more effective space debris mitigation for the given ADR mission. The investigation is carried out using the DRAMA software suite, latitude band limited re-entry only. It should be noted that impulses with the magnitudes considered for this investigation do not have an effect when applied with the circular re-entry setting, as the initial conditions of the debris primarily affects the exact impact location of the debris, which is not taken into account when using the circular re-entry setting. In practice, several mechanisms for debris release are available as part of launch vehicle separation systems already in use for current space missions [169]. Common separation methods include compressed spring systems, gas operated pistons, motorized separators, and auxiliary rockets, among others [170]. These systems are designed to generate impulses ranging from 0.06 - 10 m/s which is the range considered in the present analysis.

5.3.1 Impulse Definition

In order to model the effect of a release mechanism, a small impulse is introduced on the debris as an initial condition. This impulse is implemented as a velocity magnitude change ΔV, where the impulse direction is specified by the flight path angle γ and the heading angle χ, defined in the satellite centered orbital frame depicted in Figure 2.5. The impulse vector is defined in the body-fixed frame by the following equations:

$$
\begin{aligned}
\Delta v_x &= \Delta V \cos \chi \cos \gamma \\
\Delta v_y &= \Delta V \sin \chi \cos \gamma \\
\Delta v_z &= \Delta V \sin \gamma
\end{aligned}
\tag{5.4}
$$

The corresponding impulse is implemented within DRAMA as a change in the inertial Cartesian velocity vector expressed in the Earth-centered inertial frame, depicted in Figure 2.1. To transform the impulse vector from the body-fixed frame to the ECI frame, first a rotation by 180 about the x-axis is carried out to transform to the satellite-centered orbital frame, followed by a rotation from the satellite-centered orbital frame to the ECI frame utilizing the rotation matrix Q_r defined in terms of the debris position and velocity vectors defined in the ECI frame in Section 2.1.3.

5.3.2   Release Impulse Results

The initial conditions of the cases studied for the impulse analysis are given in Table 5.5 and are chosen to include one case for each of the five RAAN scenarios considered in Section 5.2, with the values of e and θ such that the risk factor without an impulse is greater than the acceptable threshold of 1e-4. In Figures 5.5-5.8, the risk factor is plotted against the flight path angle for four values of the heading angle ($0°$, $90°$, $180°$, and $270°$) and three impulse magnitudes (1 m/s, 5 m/s, and 10 m/s) for case 1 only. In these figures, the initial risk without an impulse is indicated as a black dashed line and the risk threshold of 1e-4 is indicated with a black solid line. From these figures, it is clear that an impulse applied at the release orbit does affect the risk factor computed with latitude band limited re-entry setting, and for certain combinations of (ΔV, γ, χ) values, significantly so. These are visible in Figures 5.5-5.8 as "dips" to 10e-10, for example in Figure 5.5, for $\Delta V = 10$ m/s and $\gamma = \chi = 0°$. These large dips in the risk factor correlate with the point of impact being predicted (using SESAM) to fall within a sparsely populated latitude band ($> 70°$ or $< -45°$). It is also evident from Figures 5.6 and 5.8 that at lower magnitude the impulse has less effect, regardless of direction when applied at heading angles perpendicular to the debris velocity vector. In addition, only a few impulse scenarios, specifically 11% of all (ΔV, γ, χ) combinations considered, cause the risk factor to increase beyond the no-impulse risk factor. Based on these results, we suggest that applying an impulse to the debris as it is released tends to decrease the risk factor of re-entry; however, as previously noted, the risk factor is largely based on the impact location which is difficult to predict accurately, and the validity of the risk factor as a reliable re-entry indicator can therefore be questioned.

Figure 5.9 shows the risk factor for each case in Table 5.5 plotted against impulse velocities ($\Delta V = 0$ to 10m/s), applied at $0°$ heading and flight path angles, as it is the most practical scenario. This plot shows that the effect of ΔV is very dependent on the initial orbit and furthermore, it is clear that increasing the impulse magnitude does not result in a proportional change in the risk factor. However, the impulse magnitude does significantly affect the impact location and therefore the risk factor as well. In combination with the results presented in Section 5.1, these release impulse findings suggest that applying a risk optimized impulse in an optimally chosen release orbit can significantly mitigate the risk

of large debris re-entry.

In terms of using debris release impulses as a mitigation measure, we have shown that introducing such impulses can have both favourable and adverse effects on the calculated risk factor. The key here is to design the impulse such that the lowest possible risk factor is achieved, with as low uncertainty as possible. In the vast majority of cases analyzed, as part of the research presented here, the introduced impulses mitigate the risk of debris re-entry; however, the extent to which this can be applied to ADR missions is highly dependent on the accuracy of the re-entry models. Historically, for uncontrolled re-entry, the general assumption is made, that after years on orbit, the state of the debris in terms of, among others, attitude, rotation, and mass is relatively unknown as the debris nears re-entry. As such, these results provide the basis for the analysis of the controlled release of objects with pre-selected initial conditions, specifically for ADR missions. This scenario is unique to ADR missions and should be factored in when evaluating the re-entry of debris as a result of these missions.

Case #	a (km)	e	i (deg)	Ω (RAAN) (deg)	ω (deg)	θ (deg)	RF without impulse
1	6571	0.0040	83	0	0	0	6.4e-4
2	6571	0.0027	83	319	0	170	5.1e-4
3	6571	0.0005	83	275	0	40	9.9e-4
4	6571	0.0010	83	225	0	240	7.2e-4
5	6571	0.0013	83	180	0	350	1.3e-3
6	6571	0.0018	83	134	0	230	1.5e-4

Table 5.5: Initial orbit parameters for impulse effect on re-entry investigation

Figure 5.5: Risk factor as a function of flight path angle of impulse - Case 1, $\chi = 0°$

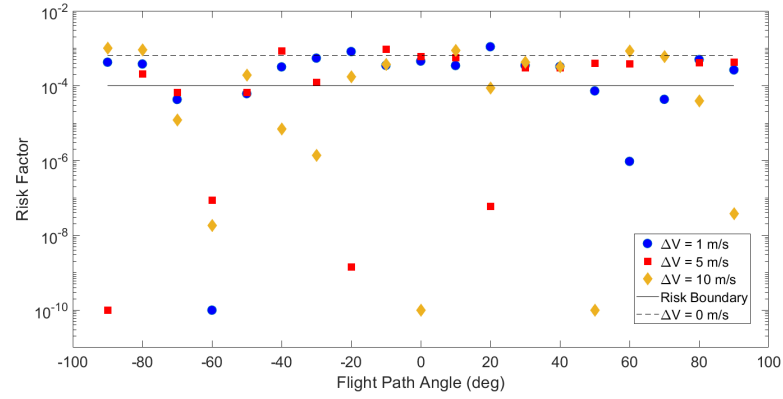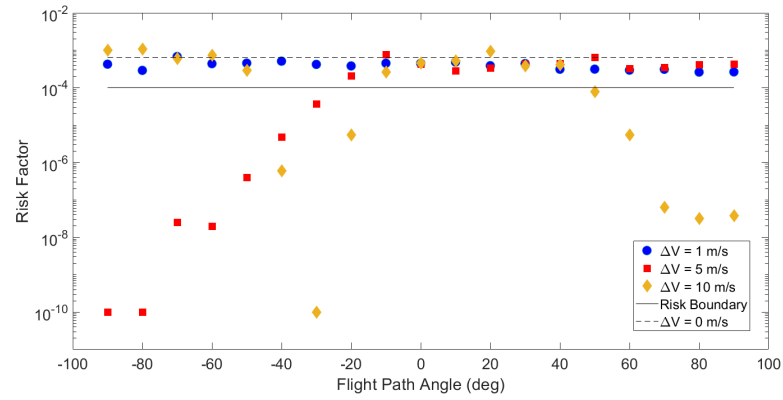Figure 5.6: Risk factor as a function of flight path angle of impulse - Case 1, $\chi = 90°$

Figure 5.7: Risk factor as a function of flight path angle of impulse - Case 1, $\chi = 180°$
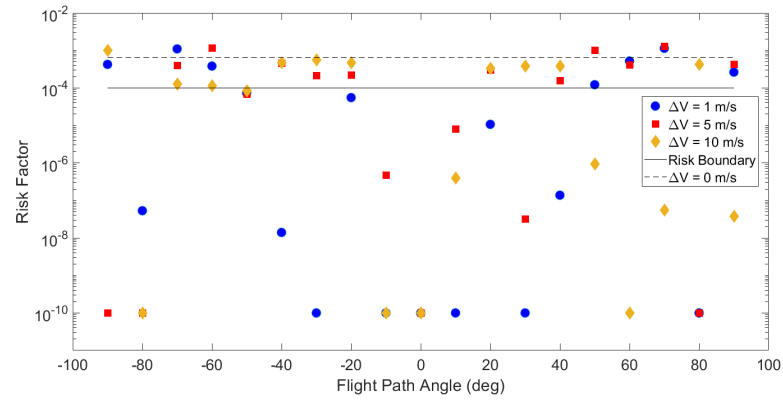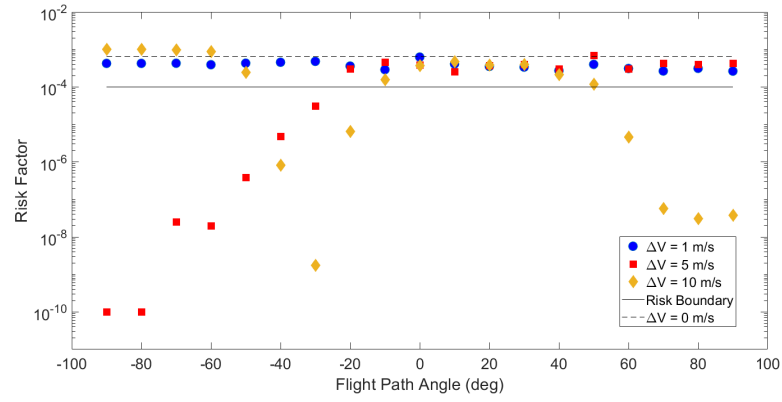
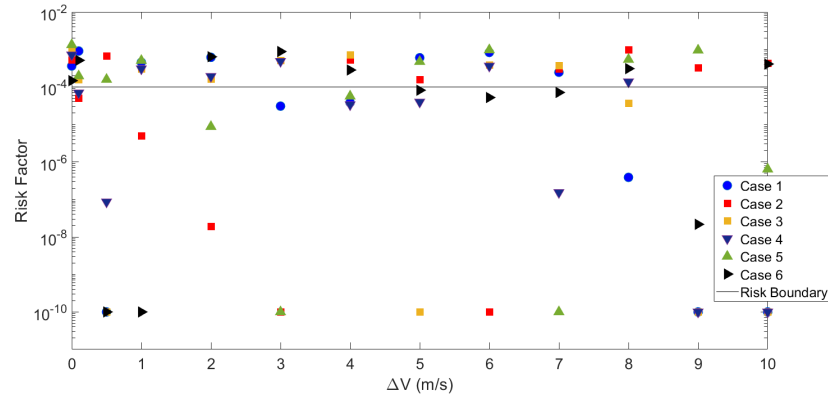Figure 5.8: Risk factor as a function of flight path angle of impulse - Case 1, $\chi = 270°$

Figure 5.9: Risk factors evaluated at $\gamma = \chi = 0°$ with varying ΔVs for the cases in Table 5.5

5.4 Attitude Motion and Re-entry

The aim of the work presented in this section is to investigate the effect of rotational motion of re-entering debris on the casualty risk factor. First, in Section 5.4.1 the DRAMA software suite is used to investigate attitude effects on the casualty risk factor by varying the initial attitude state of the debris in the release orbit. Then, to model the debris rotational motion during descent from the release orbit to the re-entry orbit, and elucidating its implications on the risk factor, D-SPOSE, introduced in Section 2.3.2, is used to propagate the attitude and position dynamics of the debris. For all scenarios considered, the debris is released with zero initial angular velocity. Last, in Section 5.4.4, observational data [171, 172] along with position-attitude propagation of the Chinese space station Tiangong-1 is used as part of a case study to analyze the rotational dynamics of large debris during re-entry and its influence on re-entry predictions such as time and location of impact.

5.4.1 Initial Debris Orientation and Rotational State

In this section, DRAMA and D-SPOSE are employed to investigate the effect of varying the initial attitude of the debris upon release on the re-entry of the debris. DRAMA is used as a dedicated re-entry analysis tool and D-SPOSE provides accurate propagation of debris positional and rotational motion.

As already mentioned, in DRAMA, there are two options for defining the initial attitude of the object for re-entry analysis: "randomly tumbling" and "fixed". For the randomly tumbling scenario, DRAMA calculates the effective cross-sectional area by averaging the "visible" area from a set of predetermined points-of-view, the directions of which are evenly distributed around the object being modelled. For the fixed attitude option, the initial attitude is defined in terms of three angles: angle of attack, side slip angle, and bank angle, corresponding to rotations about the body-fixed y-, z-, and x-axes respectively, as defined in Figure 5.10b. The initial orientation specified for the fixed attitude option determines the effective cross-sectional area during re-entry. This area is calculated as the cross-sectional area of the debris in the direction facing the flow during re-entry, including the changes due to small oscillations resulting from re-entry perturbations. As such, the calculation of the aerodynamic force and heat flux coefficients in DRAMA depend on this effective cross-

sectional area for both randomly tumbling and fixed re-entries, which in turn influence the demise and the trajectory of the debris and, thereby, determine the impact location and the value of P_i in Eq. (5.1). For both initial attitude definitions, the effective cross-sectional area changes as a result of aero-thermal effects, but is predominantly a function of initial attitude state. This effective cross-sectional area is then used to calculate the "average geometric cross-section" during re-entry, and ultimately the impact cross-section A_i in Eq. (5.2), of the debris after re-entry. It is important to note that DRAMA does not offer coupled attitude-positional propagation during re-entry.

As part of the research presented here, D-SPOSE is employed to predict the position and orientation of the debris as it descends from the initial release orbit to the re-entry orbit at ~125 km altitude. At altitudes lower than 125 km, the atmospheric conditions become more difficult to predict which makes further propagation less accurate. The piece of space debris simulated has the same material and mass characteristics as those described in Table 5.1, with initial orbital elements as specified for case 1 in Table 5.5. However, because D-SPOSE requires a triangulated representation of debris geometry, the debris shape is modelled as an equivalent surface area rectangular prism (see Table 5.6 and Figure 5.10a) for the simplicity of the triangulation, and reduced computational time. The dynamics model used for propagation in D-SPOSE includes gravitational effects up to degree and order 4 (including sectoral and tesseral terms), the aerodynamic effects (drag and torque), and the internal energy dissipation torque as described in Section 2.3.2. It should be noted that the initial debris attitude in D-SPOSE is represented by Euler 3-2-1 angles with respect to the spacecraft centered orbital frame, with the sequence of rotations being about the z-y-x axes respectively [173].

Shape	Dimensions (m)	Inertia matrix (kg m^2)
Rectangular prism	$Length = 7.448, Depth = Width = 2.126$	$\begin{bmatrix} 7198.3 & 0 & 0 \\ 0 & 7198.3 & 0 \\ 0 & 0 & 1085.7 \end{bmatrix}$

Table 5.6: Unique debris parameters for D-SPOSE propagation

117

(a) D-SPOSE   (b) DRAMA
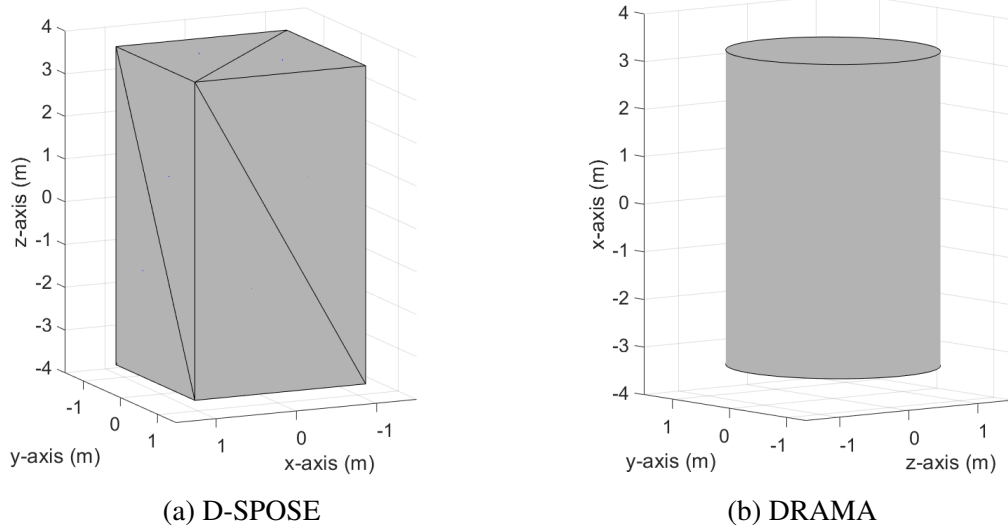
Figure 5.10: Debris geometry for simulation in D-SPOSE and DRAMA corresponding to and body-fixed axes definitions

5.4.2   The Effect of Initial Attitude Using DRAMA

DRAMA is used to generate the results showing the effect of the release attitude of the debris on the casualty risk factor presented in Table 5.7, for the release orbit with [semi-major axis, eccentricity, inclination, RAAN, argument of perigee, true anomaly] specified by $[6571, 0.004, 83, 0, 0, 0]$ (case 1 of Table 5.5). Six initial rotational states are considered in this analysis, for each of which the casualty risk factor is found using both the latitude band fixed re-entry and the circular re-entry settings. The first initial attitude state is randomly tumbling and the other five are different fixed attitudes, the latter defined with three ordered angles: angle of attack, side slip angle, and bank angle, as defined earlier.

A number of observations and conclusions can be drawn based on the results summarized in Table 5.7. First, we observe that, as expected, the different initial attitudes yield different values for the average geometric cross-section, which we have verified are within 13% of the corresponding initial flow-facing cross-sectional areas (for the fixed setting). Second, for the six attitude states considered, the risk factors computed with the latitude band limited and the circular settings are close in some cases, but drastically different in others. Indeed, the circular setting for the re-entry analysis produces risk factors which

trend with A_i values in accord with Eqs. 5.1 and 5.2: as those increase, the corresponding risk factors increase as well. For the latitude band limited re-entry, however, the attitude state with the largest cross-sectional area (16.3 m^2) produces a risk factor of 2.8e-7, which is three orders of magnitude smaller than the largest risk factor among all attitude cases considered here. This occurs because the specific impact location used to calculate P_i in Eq. (5.1) falls within a very low risk latitude band (see Figure 5.4b), resulting in significantly lower calculated casualty risk factor.

Overall, the risk factors predicted with DRAMA for different attitude states in Table 5.7 vary as follows: between 9e-5 and 2.4e-4 for the circular re-entry and, between 2.8e-7 and 8.3e-4 for the latitude band limited re-entry. This demonstrates that the effect of the rotational state on the casualty risk factor prediction is far from negligible and not necessarily intuitive. Moreover, depending on the rotational state, DRAMA may predict either a passing or a failing risk factor, all other parameters being equal. As a result, it can be concluded that the attitude state of the debris upon release can be manipulated to mitigate the re-entry risk of large debris.
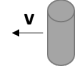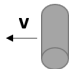
Attitude state (deg) (angle of attack, side-slip, bank)	Avg. geometric cross-section A_i (m^2)	Risk Factor latitude band limited re-entry	Risk Factor circular re-entry
Random Tumbling	14.7	3.3e-4	2.2e-4
Fixed $[0°, 0°, 0°]$	5.1	1.1e-5	9.0e-5
Fixed $[90°, 0°, 0°]$	16.3	2.8e-7	2.4e-4
Fixed $[0°, 90°, 0°]$	16.3	2.8e-7	2.4e-4
Fixed $[0°, 0°, 90°]$	5.1	1.1e-5	9.0e-5
Fixed $[45°, 0°, 0°]$	15.6	8.3e-4	2.3e-4

Table 5.7: Attitude effect on risk factor with DRAMA

5.4.3   The Effect of Initial Attitude Using D-SPOSE

D-SPOSE is employed in this section as a means to attempt high fidelity propagation of the debris rotational motion, with the view to evaluate the assumptions made in the way DRAMA captures attitude effects on the re-entry casualty risk factor calculations. D-SPOSE is used to propagate the attitude and position dynamics of the debris from the release orbit at ∼200 km altitude (semi-major axis = 6571 km) to the re-entry orbit at ∼125 km altitude (semi-major axis = 6496 km). Three propagations are carried out by initializing the simulations with three initial attitudes chosen as depicted in Table 5.8. These attitudes correspond to three of the fixed attitude cases considered in Table 5.7 using DRAMA, in particular, cases Fixed [90,0,0], Fixed [45,0,0] and Fixed [0,0,0].

We present several results, either obtained directly as outputs from D-SPOSE or by additional post processing of relevant outputs. Plotted in Figure 5.11 are the evolution of the period of rotational motion (Figure 5.11a) and the orientation of the spin axis described by its declination θ_{dec} and right ascension λ_{ra} angles (illustrated in Figure 2.1), for the three propagation cases, as per the initial conditions in Table 5.8. In Figure 5.12, the effective cross-sectional areas during descent for each release orientation case are plotted: this is the total projected area of debris faces exposed to the relative wind velocity. The results in these figures demonstrate that depending on the initial orientation, the ensuing rotational motions of the debris are significantly different. As will be shown shortly when we consider the ground tracks during descent (Figure 5.13), this can have vast implications on the risk factor analysis. The rotational motion responses in Figure 5.11 show that initially, for all three propagations, the debris rotate in an oscillatory fashion about the orbit normal direction. The rotational period responses (Figure 5.11a) cycle between values near or below the orbital period and increase to almost no rotational motion, as the direction of oscillations change. These rotational oscillations persist in a stable fashion for the [0°,0°,0°] initial attitude case, as confirmed by Figure 5.12a which shows relatively small variations in the cross-sectional area in the vicinity of the nominal value of 15.8 m^2 corresponding to the largest side of the prism facing the flow. By contrast, the [0°,90°,0°] case exhibits the most unstable response and after ∼7 hours the debris enters a tumbling motion, executing approximately two tumbles per hour henceforth. This is clearly visible in Figures 5.11b and 5.11c which reveal drastic changes in the axis of rotation from the original normal to

the orbit direction, as well as from Figure 5.12c, which shows maximal fluctuations in the effective cross-sectional area from 4.5 m^2 to 22.9 m^2. The [0°,45°,0°] initial orientation case presents an 'intermediate' response where the debris oscillates about the initial configuration for ∼12 hours, and then begins to tumble. The average rotational period for each initial orientation propagation is included in Table 5.8 and it is computed with values starting 10 seconds after release. The average rotational periods confirm that in all cases, the debris rotates or tumbles slowly, supporting the notion that each orientation of the debris experiences a sufficiently long exposure to the oncoming flow, so that its release attitude can significantly influence the descent trajectory. Not presented here, but additional propagations were carried out with D-SPOSE by initializing the debris in arbitrary orientations relative to its direction of motion. The corresponding results unequivocally confirm that the debris will enter a slow tumbling motion regime soon after its release.

In Figure 5.13 we present the ground track of the debris for each of the three initial attitude state propagations. Figure 5.13a shows the ground tracks for the first three hours of descent starting from the initial orbit, and Figure 5.13b shows the last two hours of descent before reaching the re-entry orbit. The results in Figure 5.13 are generated by postprocessing the D-SPOSE output position (time-stamped) using the MATLAB Aerospace toolbox, thereby generating latitude-longitude coordinates and altitudes at each time step of the simulation. These coordinates are then plotted on a 2-dimensional world map to show the debris ground track during the descent. As can be seen from Figure 5.13a the ground track and position along it are the same for the first three hours of descent for the three initial attitude propagations. However, as we deduce from Figure 5.13b, the trajectories of the debris start to deviate as a result of different rotational motions, which ensue after several hours. Thus, two hours before reaching the re-entry orbit, the debris are already at different points in the orbit and, not surprisingly, they are at different locations above Earth when they reach the re-entry orbit. From Figure 5.13, it is clear that for different initial orientations, the ground track the debris follows from 200 km to 125 km is approximately the same in each case; however, the trajectories and descent times of the three cases are not. The descent times presented in Table 5.8 vary, depending on the initial orientation, between 21.1 and 23.3 hours with D-SPOSE. This means the debris reaches the re-entry orbit at vastly different locations above Earth, and ultimately, the initial attitude state of

the debris affects its impact location, directly changing the risk factor for that particular re-entry.

Another relevant result presented in Table 5.8 is the average geometric cross-sectional area of the debris directly affected by the atmospheric conditions during the descent, as computed with D-SPOSE. These values were calculated by averaging the effective area (as per Figure 5.12) used at each time step to calculate the aerodynamic effects on the debris, over the entire descent and they range between 14.9 and 16.5 m^2. Our reason for presenting these values is for direct comparison to the average geometric cross-sectional area calculated in DRAMA. The largest average geometric cross-sectional area found for the [0°,0°,0°] attitude case also results in the shortest descent time and the smaller geometric cross-sectional area found for the [0°,45°,0°] attitude case results in the longest descent time as expected.

We suggest that D-SPOSE findings presented above, have direct implications on the re-entry analysis carried out with DRAMA and the results thereof. The coupled orbit-attitude propagation in D-SPOSE predicts that after releasing the debris in an arbitrary configuration, with zero initial angular velocity, the debris begins a slow tumbling motion. It should also be mentioned that, in simulation, this tumbling motion can be avoided by introducing a significant initial spin (to achieve spin stabilization) and for certain spinning motions, the debris may maintain an approximately constant (fixed) orientation in inertial space. In light of this, short of inducing a specific angular velocity in the debris upon release, D-SPOSE results imply that the fixed attitude setting in DRAMA is unrealistic.

With this insight, we can comment on the use of random tumbling option in DRAMA for re-entry analysis. First, it is noted that the average cross-sectional area range found with the randomly tumbling setting in DRAMA (14.7 m^2) is in fair agreement with the average cross-sectional area found with D-SPOSE, for the three cases in Table 5.8. On the other hand, using DRAMA with the random tumbling option, it is not possible to capture the effect of the different initial orientations at the release: as was observed from D-SPOSE results, the initial orientation has a large influence on the predicted impact location. Although DRAMA captures some aspects of randomly tumbling motion, it cannot predict variations in descent times and final positions, and hence the risk factor, resulting from different debris orientations at release.
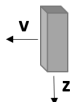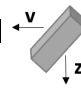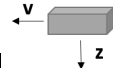
Initial attitude (3-2-1 Euler angles) (deg)	Avg. geometric cross-section (m^2)	Descent time to 125 km altitude (hours)	Avg. tumbling rotational period (hours)
$[0°, 0°, 0°]$	16.5	21.1	12.2
$[0°, 45°, 0°]$	14.9	23.3	4.3
$[0°, 90°, 0°]$	15.8	22.5	23.0

Table 5.8: Initial attitude cases for D-SPOSE propagations and relevant propagation statistics
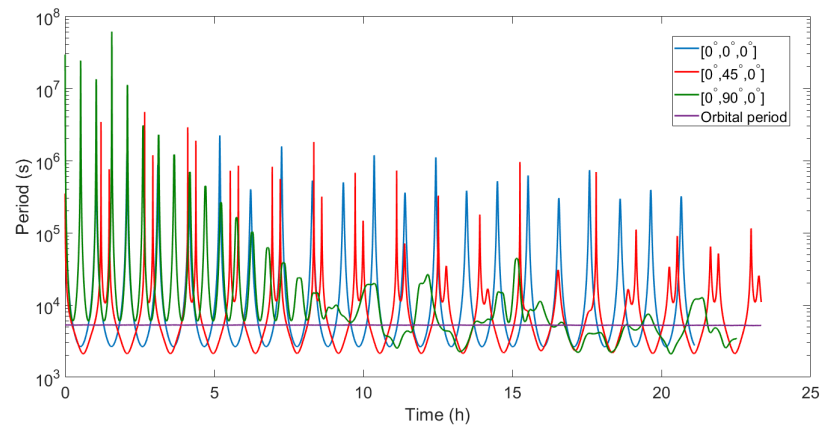
(a) Period
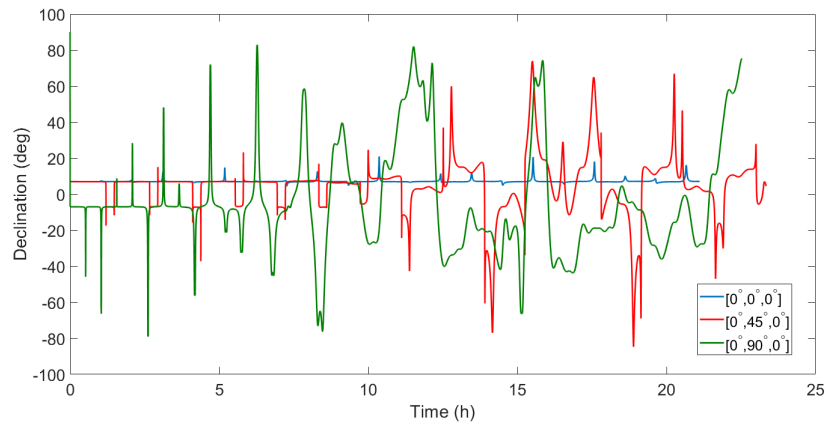
(b) Spin axis declination during re-entry
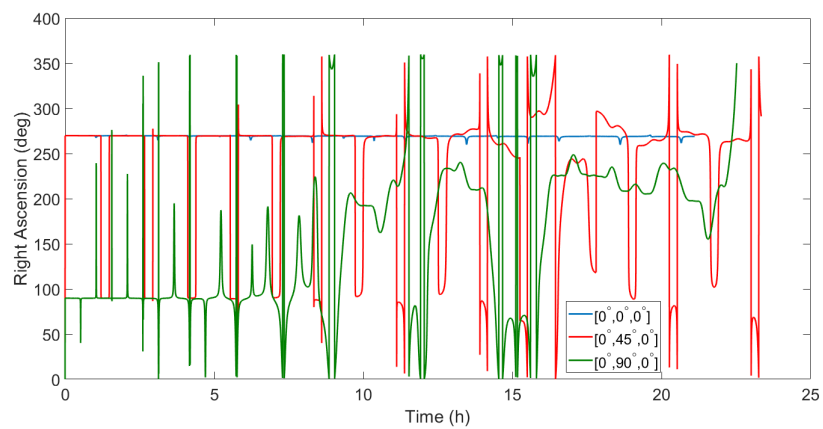
(c) Spin axis right ascension during re-entry

Figure 5.11: Attitude motion during re-entry
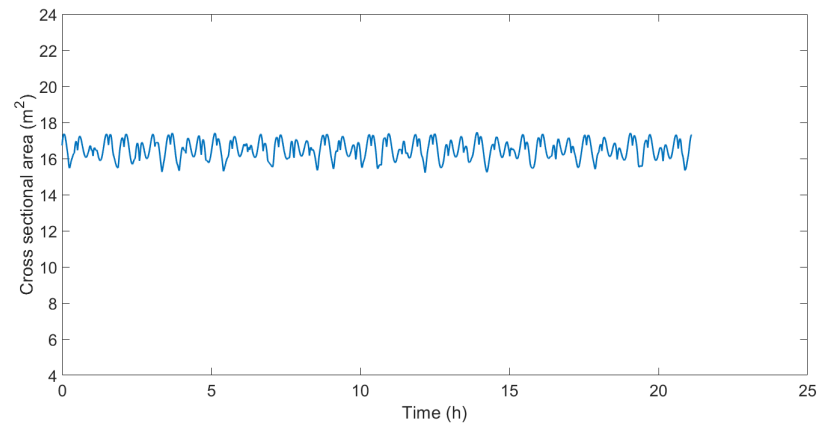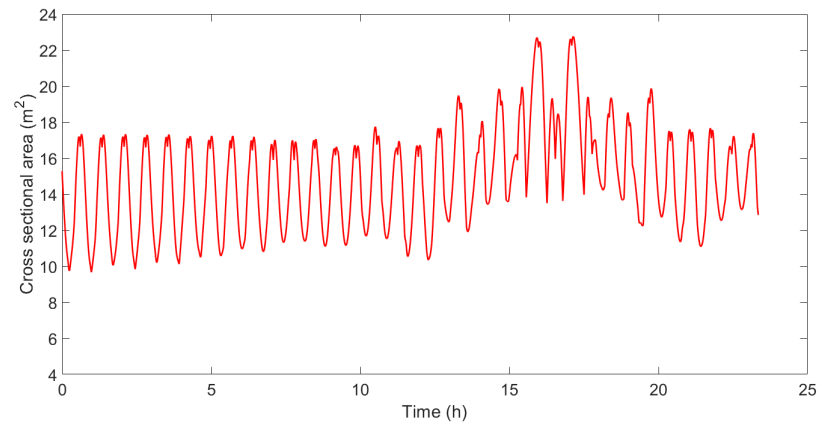
(a) $[0°, 0°, 0°]$ case

(b) $[0°, 45°, 0°]$ case
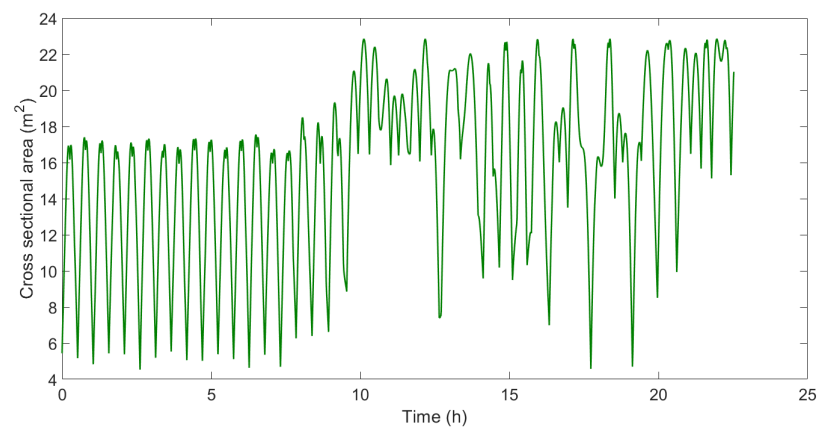
(c) $[0°, 90°, 0°]$ case

Figure 5.12: Effective cross-sectional area during descent
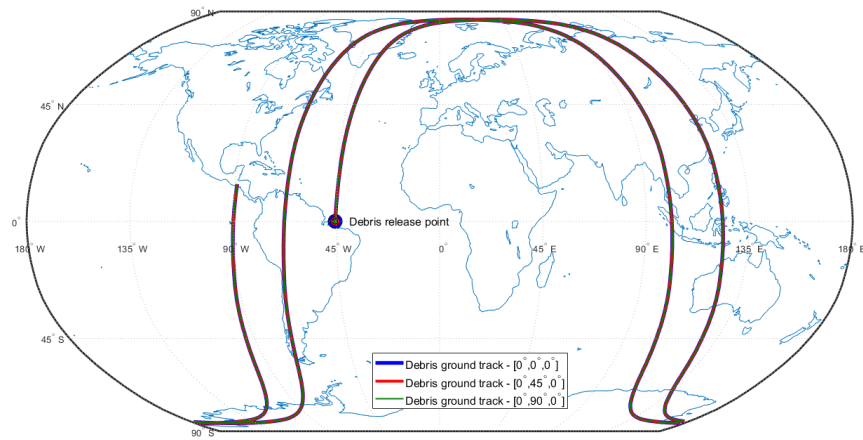
(a) First three hours of re-entry
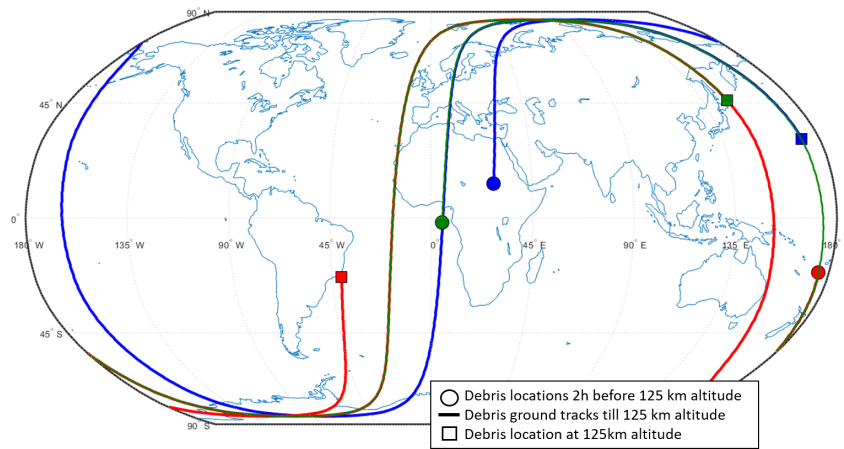
(b) Last two hours of re-entry

Figure 5.13: Ground track of debris for three initial attitude configurations - blue: [0°,0°,0°], red: [0°,45°,0°], green: [0°,90°,0°]

5.4.4 Case Study: Tiangong-1

Given the high number of large pieces of space debris in lower Earth orbit, some are bound to re-enter Earth's atmosphere and due to their size, mass, and material composition, these pieces of debris will survive re-entry and impact Earth. One example of such debris was the first Chinese space station, Tiangong-1, launched in September 2011, which re-entered Earth's atmosphere on April 2, 2018. Here, Tiangong-1 is used as a case study to analyze the effect of the orientation of large debris during re-entry and its influence on re-entry predictions such as time and location of impact. Using D-SPOSE, simulations are conducted of the satellite's rotational and positional motion to provide a better understanding of its effective cross-sectional area during the last days of its life.

(a) D-SPOSE   (b) DRAMA
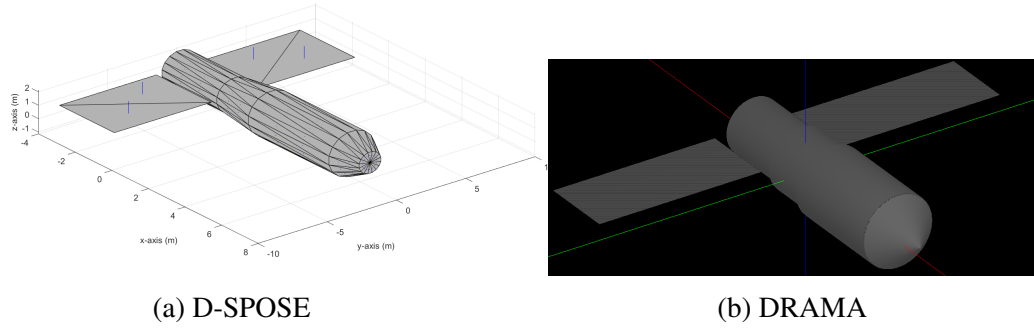
Figure 5.14: Debris geometry for simulation in D-SPOSE and DRAMA in body-fixed frame

Presented in Figure 5.14 are the two Tiangong-1 geometries used for simulation in D-SPOSE and DRAMA respectively. These geometries are generated based on dimensions provided in [172]. Furthermore, attitude observations provided by Lin et al [172] and Sommer et al [171] are plotted in Figure 5.15 along with the long-term angular velocity prediction found by propagating the motion of Tiangong-1 for 135.1 days using D-SPOSE.

With the predicted angular velocities in hand, we proceed to study the effect of the evolving attitude dynamics of the spacecraft on its orbital motion during Tiangong-1's descent to Earth. In particular, the short-term effects of the changing cross-sectional area of Tiangong-1, as a result of the rotational dynamics, on the re-entry predictions starting with one day up to 7 days prior to impact are presented. The initial conditions for each propa-
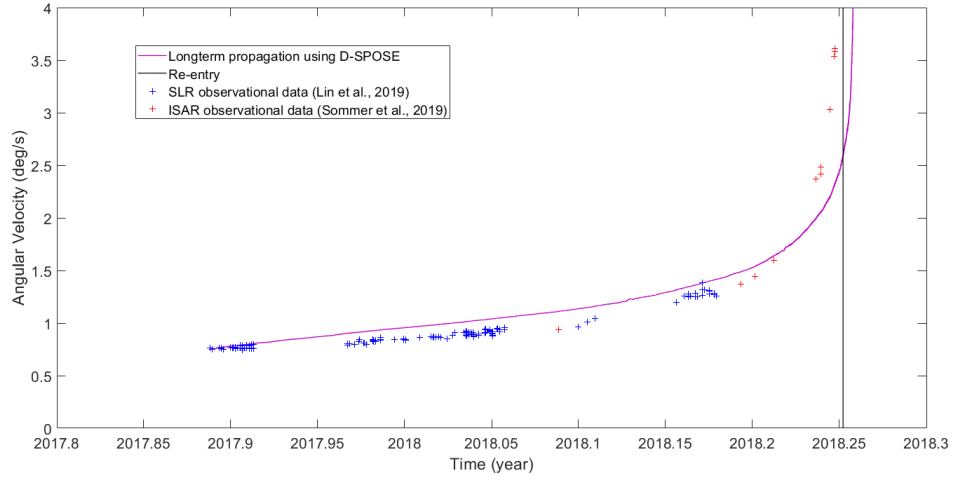
Figure 5.15: Evolution of angular velocity magnitude of Tiangong-1

gation are provided in Table 5.9. There are three types of propagation, distinguished by the length of propagation prior to the actual impact time (02/04/19 00:16:00). One additional propagation one day before impact is presented to highlight the effect of having a different initial debris attitude at the onset of propagation, this propagation is denoted by "1*". The initial orbital elements and the time of initiation of the propagation are defined by observational data from TLEs. All initial angular velocities and attitudes (with the exception of the 1* case) are defined using the corresponding values of the long-term propagation in Figure 5.15 one, three, and seven days before the predicted impact for the one-, three-, and seven-day propagations respectively.

Length of Propagation (days)	Orbital Elements (from TLEs)	Date and Time	Attitude (3-2-1 Euler angles) (deg)	Angular velocity (deg/s)
1	[6550.67,0.0019,42.76, 19.50,200.61,341.21]	01/04/2018 04:44:00	[-5.68,21.04,91.05]	[-0.09,-0.28,2.94]
1*	[6550.67,0.0019,42.76, 19.50,200.61,341.21]	01/04/2018 04:44:00	[0,0,0]	[-0.09,-0.28,2.94]
3	[[6571.73,0.0021,42.77, 15.58,213.20,344.43]	30/03/2018 02:38:00	[7.95,-26.38,78.34]	[0.07,-0.17,2.45]
7	[6595.73,0.0023,42.76, 358.12,241.04,1.90]	25/03/2018 21:00:00	[-176.80,24.33,-95.70]	[0.03,0.12,1.78]

Table 5.9: Tiangong-1 initial conditions for propagations

128

5.4 Attitude Motion and Re-entry

For each propagation (one, three, and seven days before impact), two definitions for the cross-sectional area are used. First, the time-varying values are used and the effective area of Tiangong-1 for each propagation are presented in Figure 5.16. The mean values of the cross-sectional area during each of these propagations are used as the fixed area parameter for three additional "fixed area" propagations. The effects of having time-varying vs. fixed cross-sectional area are quantified in terms of the difference in time and location of the debris at the point of re-entry (defined as reaching ∼125 km altitude) found by propagating Tiangong-1 over the same time period and with the same initial conditions for the two cross-sectional area definitions. The results of the effect of cross-sectional area on re-entry are obtained using D-SPOSE for coupled orbital-attitude propagation (hence, time-varying area) versus using D-SPOSE for orbital propagation only (with constant or fixed cross-sectional area).
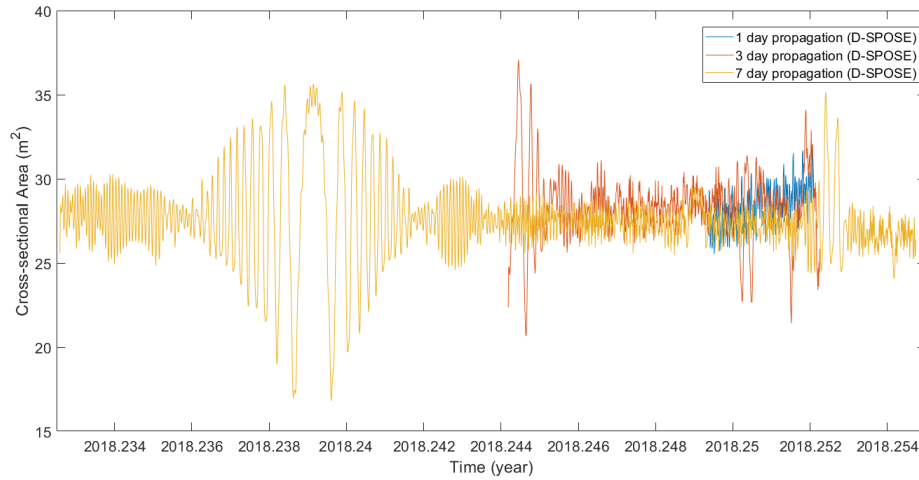
Figure 5.16: Tiangong-1's cross-sectional area during time-varying propagation (1-hour moving average)

The effect of the debris cross-sectional area definition, on the altitude during re-entry is presented as three altitude vs. time plots in Figure 5.17. The exact re-entry times are provided in Table 5.10 and the locations of Tiangong-1 post propagation are illustrated in Figure 5.14a. For the one- and three-day propagations, the re-entry time is almost the same for both definitions of cross-sectional area. However, for the seven-day propagation there are significant differences in the predicted re-entry time as depicted in Figure 5.17c. This

is expected as the effects of time-varying area on the motion of the debris are larger over time. In Figure 5.17c, the altitude vs. time plot of the long-term propagation is presented as a point of reference. It is evident from the plots in Figure 5.17 that as the propagation time increases, the prediction of re-entry time steers away from the actual re-entry time and towards that of the long-term propagation. This result suggests that the initial angular velocity and attitude play a significant role in the re-entry time prediction and more so the longer the given propagation is carried out for.

Another interesting observation, as a result of propagating Tiangong-1 with a vastly different initial attitude ($[0°,0°,0°]$) over a one-day period before re-entry, is the much earlier re-entry time as compared to the other two, one-day propagations (see Figure 5.17a). One conclusion that can be drawn from this result is, again, the significant effect initial attitude has on short-term debris re-entry predictions.

Length of Propagation (days)	Tiangong-1 Area (m^2)	Date and Time of Re-entry
135.1	Time-varying	04/04/2018 06:39:53
1	Time-varying	02/04/2018 00:19:23
1*	Time-varying	01/04/2018 12:39:23
1	28.36	02/04/2018 00:19:23
3	Time-varying	02/04/2018 02:08:01
3	28.33	02/04/2018 01:58:01
7	Time-varying	03/04/2018 10:10:00
7	28.58	03/04/2018 01:30:00

Table 5.10: Tiangong-1 time of re-entry based on cross-sectional area using D-SPOSE

The re-entry locations as a result of the D-SPOSE propagations are illustrated in Figure 5.18a. In addition, DRAMA is employed to conduct the re-entry analysis from ∼125 km altitude (defined using the latest TLE) to impact by using the time-averaged cross-sectional area. The impact locations as a result of the analysis using DRAMA are presented in Figure 5.18b. From the locations of Tiangong-1 presented in these figures, we can deduce that the cross-sectional area during re-entry plays an important role in determining not only the predicted re-entry time but the location as well. Furthermore, it is clear that including the effects of rotational motion significantly changes the location of re-entry. As concluded in Section 5.4.1, the results presented here also attest to the significance of initial attitude on debris re-entry predictions.
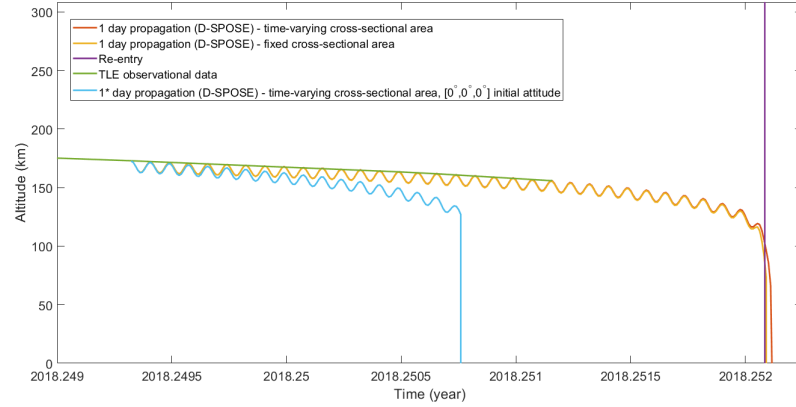
(a) Tiangong-1 position and attitude propagated from 1 day before re-entry
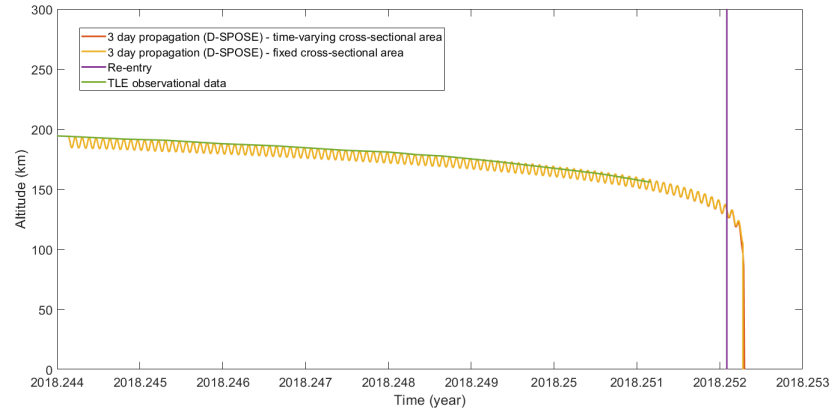
(b) Tiangong-1 position and attitude propagated from 3 days before re-entry
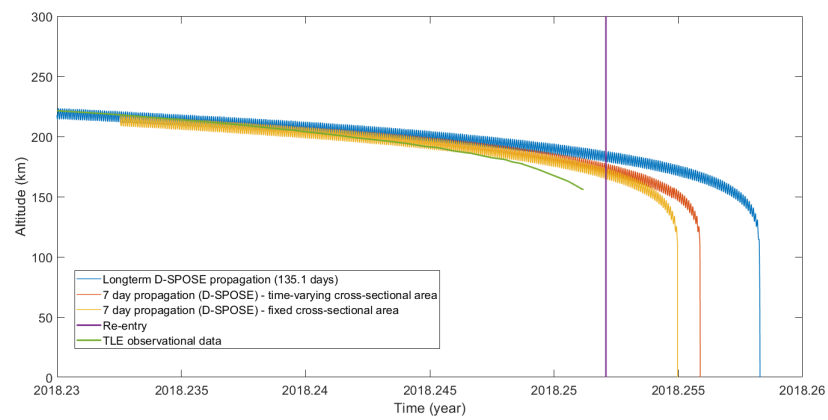
(c) Tiangong-1 position and attitude propagated from 7 days before re-entry

Figure 5.17: Tiangong-1 re-entry altitude vs. time
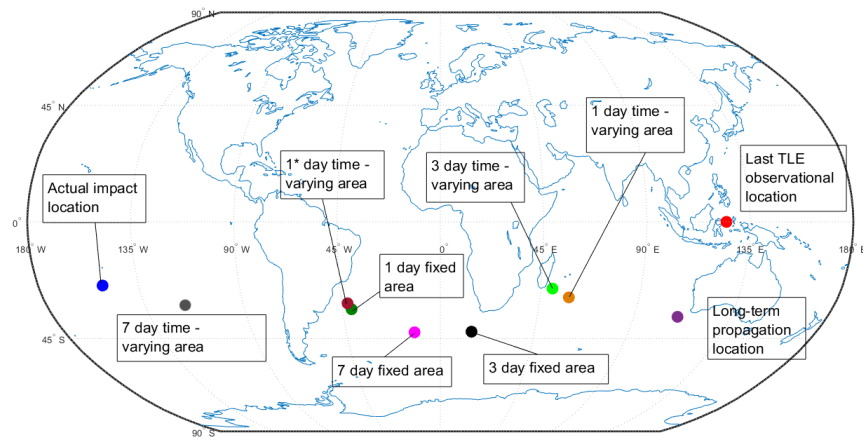
(a) Tiangong-1 position after propagation using D-SPOSE (~125 km altitude)
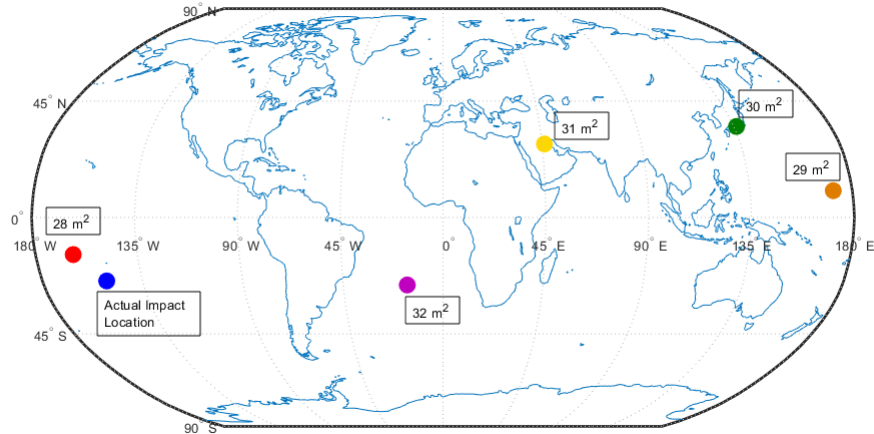
(b) Tiangong-1 impact location predicted using DRAMA

Figure 5.18: Tiangong-1 locations after simulation

132

5.5   Chapter Summary

The impact location and hence the risk factor are shown to be influenced by the initial parameters of the orbit in which the debris is released. These effects are analyzed using two pieces of software, namely, DRAMA and DAS. DRAMA provides a higher-fidelity analysis, and when the results are compared, DAS is shown to produce a slightly more conservative risk factor estimation. Using DAS and using the circular re-entry setting in DRAMA, it was found that the initial orbit inclination is the parameter which affects the risk factor the most. Using the latitude band limited re-entry setting in DRAMA shows that other orbital elements (eccentricity, RAAN, and true anomaly) also affect the risk factor. Further analysis using DRAMA demonstrates the effect of introducing an impulse onto the debris, specified by magnitude and direction, when released. The risk factor can be changed by varying degrees by applying such an impulse, depending on the specified direction, and the magnitude of the impulse. Additionally, the risk factor is a function of the average geometric cross-sectional area of the debris during re-entry, and DRAMA is employed to show the effects of varying this area on the resultant re-entry risk factor. The average geometric cross-sectional area is altered by defining the attitude state using one of DRAMA's two options: randomly tumbling or fixed attitude. A general trend is identified with the circular re-entry setting, showing the lower the average geometric cross-sectional area, the lower the casualty risk factor. Overall, it is difficult to identify correlations between the various influencing factors and the calculated risk factor, primarily due to the high sensitivity of the impact location to the initial conditions of the debris at release. However, it is shown, through the careful consideration and design of the debris release conditions, the casualty risk as a result of re-entry of large debris can be mitigated to an extent where casualty risk factor standards are met.

Last, the D-SPOSE software is employed as a tool to investigate the effect of rotational motion on the orbital motion during descent, with the view to understanding the implications on the accuracy of the re-entry analysis performed using DRAMA. D-SPOSE is used as a coupled position-attitude propagator to account for the more nuanced attitude effects on re-entry, not captured by DRAMA. As such, it is concluded that the initial attitude of the debris affects the ensuing rotational motion of the debris during decent, sufficiently so

as to modify the trajectory of the debris and the time of descent. Therefore, each initial orientation results in a different impact location and correspondingly, a different risk factor. When interpreting the propagation results obtained with D-SPOSE in the context of DRAMA re-entry analysis, it can be concluded that the fixed attitude setting in DRAMA is not a realistic option for re-entry analysis, due to the development of a slow tumbling attitude motion, regardless of initial attitude. Furthermore, the randomly tumbling re-entry setting in DRAMA only captures the effects of a 'generic' tumbling state and not the particular evolution from a specific initial attitude of the debris when released. Tiangong-1 is used as a case study to analyze the effect of the orientation of large debris during re-entry and its influence on re-entry predictions such as time and location of impact.

6

Conclusions & Future Work

6.1 Summary of Results and Contributions

Given the effects on the space environment of numerous collision events, in combination with large defunct spacecraft re-entering Earth's atmosphere, it is safe to say space debris is a growing cause for concern. As such, the aim of this thesis is to expand the boundaries of how active debris removal missions can be planned, designed, and carried out effectively and efficiently in the future. In particular, the research for this dissertation focuses on planning a multiple debris removal mission since there is a strong consensus that removal of five large pieces of debris per year is a necessity to remediate the threat of space debris on the near Earth environment.

In this context, we identified and explored two mainstream approaches for multi-debris removal missions: recursive, where a chaser de-orbits the targeted piece of debris to a disposal orbit and then returns to another debris orbit in order to de-orbit the next piece of debris in a sequential or recursive fashion, and a mothership approach, where a chaser travels from one piece of debris to the next, deploying smaller thruster modules (packets) which attach to- and de-orbit the debris to a disposal orbit. To our knowledge, the recursive mission scenario has not been extensively studied; we believe, however, it is particularly suited to ADR missions that do not provide a rigid or close connection between the chaser and the debris, such as those employing capture methods like tethered nets, and it is the approach of choice for our investigation. In our investigation, we first employed the well-

known Edelbaum's analysis for low thrust transfers. This analysis was incorporated into a novel framework, designed to minimize the time and fuel cost of rendezvous and de-orbit, for a recursive style multiple ADR mission with drift orbits included as a measure of reducing fuel cost. As a comparative measure, a formulation for removing multiple pieces of debris in a "travelling salesman" fashion is presented in the form of a mothership approach to multiple ADR. Lambert's theorem is applied for the basis of further analysis, in order to find optimized impulsive transfers between consecutive pieces of space debris for the mothership approach. The resulting fuel cost and time of transfers for a five debris mission using the mothership approach are compared to those of carrying out the same mission, using the recursive approach. Our main contribution to planning the multiple debris removal mission is the formulation and solution of an optimal control problem which we solve to minimize the fuel and time cost of point-to-point rendezvous and de-orbiting of multiple pieces of space debris. As part of this third formulation considered, each manoeuvre is defined as a minimum-time orbital transfer, using low-thrust propulsion, and the transfer is posed as a constrained non-linear optimal control problem.

Given the necessity for high accuracy rendezvous when carrying out ADR, a new approach to defining the aforementioned constrained non-linear optimal control problem is presented. This formulation considers the true anomaly as a boundary condition. Furthermore, a good initial guess for the transfer time is also required to solve each orbital transfer problem in this formulation. To this end, a simplified, debris-specific, optimal control problem is presented and solved to generate an initial guess, at an accuracy that is adequate enough to find the minimum-time orbital transfer for rendezvous with a given piece of debris. A novel approach to generating this initial guess for each debris is formulated based on attributing different weights to those orbital parameters that are more costly to match for a specific piece of debris. A further complication addressed in this thesis is the fact that the long time taken for low-thrust transfers results in the debris location changing significantly between the transfer initiation and the arrival of the chaser in the desired orbit. As such, the initial guess for the transfer time constitutes the period over which the given piece of debris is propagated to find the location of the debris after transfer. The location of the debris is then used as an initial guess for the final boundary constraint of the chaser's high-accuracy transfer. This procedure is iterated until the post-propagation location of the debris matches

the location of the chaser following the high-accuracy transfer, within certain error bounds, to achieve efficient accurate low-thrust rendezvous for multiple ADR. The main outcome of this optimal solution procedure is an estimate of the time and fuel costs of a multiple debris removal mission, which is a key novel contribution to multiple ADR mission design and development.

One drawback to elaborate missions in space, such as multiple ADR, is the increased fuel requirement. In addition to using low thrust as a means of carrying out orbital manoeuvres, another way in which ADR missions can be made efficient is by introducing drift orbits to match the RAAN of the chaser to that of the debris at the cost of time as opposed to fuel. Presented in this thesis is a novel way of introducing drift orbits as part of an optimized orbital transfer. The drift orbits are selected based on their altitude and inclination, as these are the key parameters affecting RAAN drift rate. The drift orbit selection process is formulated as an optimization problem, minimizing the overall time and fuel cost of the given orbital transfer. Given that, in the drift orbit selection process, time and fuel cost are conflicting objectives, upper boundaries on these costs are introduced, and various results are found, depending on how each of these objectives are weighted.

In order to compare and validate the recursive and mothership approach to multi-ADR, four sets of debris in LEO are used as input for the investigations presented in Chapter 4. The first set of debris (set 1) consists of five high risk pieces of debris including Envisat, orbiting in similar inclination bands, but with large RAAN differences. Sets 2, 3, and 4 consist of SL-8 rocket bodies with similar physical properties but have varying orbital parameters. Debris set 2 in particular is a selection of five SL-8 rocket bodies in similar inclination bands, with small RAAN differences. Using debris sets 1 and 2 as inputs to the mothership approach and to the Edelbaum-based formulation for the recursive approach, we calculate the time and fuel costs of removing each set using both approaches. The results of each approach for the first set of debris show that missions involving high RAAN differences between the debris are much better suited for the recursive approach. For debris in the second set, the cost of the mothership approach is significantly lower both in terms of time and ΔV than in the recursive approach. The rendezvous transfer in the mothership approach is performed directly from one debris location to the next, which requires a lower ΔV cost when the RAAN and inclination differences are small, as the changes in

semi-major axis are much smaller. The fuel mass requirements are, in general, lower for the recursive approach, as thrusters supplying low continuous thrust have a much higher specific impulse than high thrust systems.

The optimal control approach to the recursive mission takes into account the changing orbital state of the debris as the mission is carried out/simulated. Therefore, time-stamped debris data (in the form of TLEs) is required. Due to perturbations affecting the debris in LEO, the exact debris parameters used are not the same as those used previously. Hence, debris set 3, like set 2, is a selection of five SL-8 rocket bodies with similar inclinations; however, set 3 debris have completely different RAAN from those in set 2, as it is time-stamped on the 1st of January 2016. Debris set 4 is selected purely to demonstrate the option of analysing debris with large inclination differences using the optimal control approach to multiple debris removal. As such, it consists of two pieces of debris with a large inclination difference. De-orbiting the five pieces of debris in the set 3 is deemed achievable within the one-year time frame, with the main contributor to the time of transfer being the altitude change. The total estimated fuel requirement for de-orbiting the five pieces of debris in this set is approximately 58% of the chaser mass, which is deemed reasonable for this type of mission. For set 4, the large change in inclination results in an increased transfer time and fuel mass requirements; it would neither be practical, nor achievable, to remove five pieces of debris with large inclination differences within a one-year time limit. It is worth noting that this does not mean that two of the five debris cannot have large inclination differences for the mission to be carried out in a timely manner. As previously established, the recursive approach is better suited for debris set 1 and this set is therefore used again to test the optimal control problem formulation, given the possibility of drift orbit inclusion. De-orbiting this set is deemed achievable within 2.23 years, with the main contributor to the time of transfer being the RAAN drift requirement and the long de-orbiting time due to the large mass of the debris. This gives a more realistic estimation of the costs associated with removing debris in set 1 using a recursive approach than the results calculated using the low fidelity formulation,

The second major contribution of this thesis is the detailed analysis of certain factors affecting the large space debris re-entry resulting from a recursive orbital debris removal mission. The risk factor calculated for uncontrolled re-entry of the large debris (SL-8 rocket

bodies) in this research is predominantly too high, and as such, this type of debris is not suitable for conventional uncontrolled re-entry. Active space debris removal allows for controlled de-orbiting of the debris, and multiple debris removal missions provide an option for removing multiple pieces of debris efficiently. During such missions, the debris is de-orbited to a disposal orbit which in the context of re-entry analysis, becomes the initial orbit. From here, the debris is either allowed to re-enter on its own accord (uncontrolled re-entry) or the chaser spacecraft re-enters with the debris providing means of controlled re-entry. Given that conventional uncontrolled re-entry is too high-risk, and that controlled re-entry requires the chaser to re-enter, thus making removal of other debris impossible, we explored potential options for lowering the risk of uncontrolled re-entry. A novel consideration unique to re-entry as a result of ADR is having the knowledge and some degree of control on the debris state upon release into a low altitude disposal orbit. Re-entry analysis and prediction can therefore be augmented, as a result of knowing the exact characteristics, location, and attitude state of the debris when released.

To this end, two existing re-entry models, the Debris Risk Assessment and Mitigation Analysis (DRAMA) model, and the Debris Assessment Software (DAS), are used to study the influences of varying the parameters of the disposal orbit and the release conditions on the resultant casualty risk factor. With this perspective, the de-orbiting stage of an active debris removal mission can be designed such that the parameters of the disposal orbit minimize the casualty risk of large debris re-entry, while maintaining feasible fuel and time constraints on the de-orbit manoeuvre. With respect to release conditions, the effect of introducing a small-magnitude impulse onto the debris at the release is studied, consequently showing that the casualty risk factor can be lowered in addition to it being lowered as a result of release orbit parameters. It is also shown that, the change in the risk factor that results from an impulse is highly dependent on both the magnitude and the direction of the impulse with respect to the debris flight path. Furthermore, it has previously been demonstrated that the orientation and surface area of a piece of debris at the onset of re-entry have a significant impact on the characteristics of the re-entry. Hence, the coupled orbit-attitude propagator D-SPOSE, is used to analyze the rotational state evolution of the debris between its release at $\sim$200 km and the onset of re-entry assumed at $\sim$125 km altitude, highlighting the importance of considering attitude dynamics for re-entry analysis. Last, a case study

of the Tiangong-1 re-entry is presented, showcasing the difference in re-entry predictions made depending on the cross-sectional area estimation of Tiangong-1 used during descent. From these results, we can conclude that the debris rotational dynamics significantly affects the re-entry and therefore play an important role when making re-entry predictions.

6.2   Recommendations for Future Work

The approach to analyzing multiple debris removal missions presented in this thesis addresses certain key aspects of multiple debris removal missions, namely rendezvous, deorbit, release, and re-entry. Costs incurred during the capture and potential rigidizing stages of the mission are highly dependent on the given capture method and have therefore not yet been considered.

As a topic of future work, a procedure can be developed for selecting viable capture methods based on the costs of removing certain sets of debris, using different approaches to multiple debris removal. Once the capture method has been selected, the costs and time of the mission can be predicted more accurately and the whole process can be iterated to find an optimal capture method or removal approach, if necessary. Adding to this, more detailed analysis can be carried out on the coupled chaser-debris system in terms of defining the dynamics for orbital transfers, once the capture method has been selected. When solving the minimum-time optimal control problem, low-continuous thrust is assumed. As part of furthering the analysis carried out here, this assumption can be relaxed by introducing a throttle capacity allowing for variable thrust within each orbital transfer. In a similar fashion, the notion of thrust arcing, where chaser acceleration due to thrust is considered as a binary function (on/off) that can be changed during an orbital transfer can also be considered. Introducing more complex thruster capabilities will likely reduce the estimated fuel cost for a given orbital transfer and is therefore a worthy consideration despite the added complexity and component cost. Adding to the notion of more advanced thruster capabilities, considering a hybrid system where both low thrust and impulsive transfers are possible within the same mission is also of interest. In this case, the type of propulsion method for a given transfer can be selected based on fuel cost and time constraints allowing for a higher degree of optimization on the mission as a whole and an increased scope in terms of the combinations of debris that can be removed within a single mission.

It has been demonstrated that the selection of specific pieces of debris for a multiple debris removal mission contributes to the cost and even the feasibility of the mission. As such, future work should consider the cost of removing a set of debris as opposed to just considering each piece of debris individually, as part of the selection procedure, i.e., integrating the debris removal optimization procedure into the debris selection process. This is no simple feat, as, for example, the RAAN of the debris changes significantly over the course of an ADR mission, and as RAAN is an important factor when calculating mission cost, all pieces of potential debris to be removed need to be propagated over the course of the mission to account for and predict the location of the debris at the appropriate time — at the capture stage of the mission.

The findings from the re-entry analysis suggest that the current approach to re-entry predictions is not tailored to re-entries as a result of ADR. Future work in this area includes incorporating more accurate attitude dynamics into existing models for re-entry. Furthermore, some considerations can be made for using risk factor as a determining metric for re-entry, as the risk factor calculation is shown to be volatile, and subject to large uncertainties. Last, the desired conditions of the disposal orbit to minimise the risk factor can be coupled with the analysis of the de-orbiting manoeuvre such that the exact disposal orbit desired for release is factored into the mission cost calculations. Consequently, the hopes and intentions for the contributions presented in this thesis are to provide some groundwork for future investigations and analyses in this relatively new field, by establishing the basis from which actual multiple debris removal missions can be designed and carried out. In all, the author suggests that considerations should be made when designing ADR missions for the trade-off between designing a chaser spacecraft for demise, and achieving controlled re-entry, vs. designing the release of the debris such that the risk of uncontrolled re-entry can be reduced and a more efficient multiple debris removal mission for large debris can be achieved.

A

Appendix

The following appendix contains the full iterative results of the case studies presented in Sections 4.3.1, 4.3.2, and 4.3.3. Tables A.1 and A.2 show the full iteration results for debris sets 3 and 4 respectively. In addition, the full iteration results for rendezvous using a drift orbit are presented in Table A.3.

Appendix

Transfer Description	a (km)	e	I (deg)	Ω (deg)	ω (deg)	θ (deg)	Time (days)
Debris 1 initial	7363.6	0.0021	82.94	3.078	184.1	239.0	N/A
Chaser to Deb.1 initial	7363.5	0.0017	82.93	2.981	193.5	240.0	19.67
Deb.1 P_1	7366.1	0.0030	82.94	348.6	126.5	179.1	19.67
Chaser to Deb.1 P_1	7366.6	0.0025	82.95	348.5	136.5	180.1	19.85
Deb.1 P_2	7368.5	0.0018	82.95	348.5	97.25	36.75	19.85
Chaser to Deb.1 P_2	7368.0	0.0024	82.94	348.6	107.2	37.75	19.64
Deb.1 P_3	7373.9	0.0023	82.95	348.6	110.0	42.76	19.64
Chaser to Deb.1 P_3	7373.4	0.0019	82.94	348.5	120.0	43.79	19.83
Deb.1 P_4	7376.6	0.0023	82.95	348.5	107.7	266.6	19.83
Chaser to Deb.1 P_4	7376.1	0.0013	82.94	348.4	97.74	265.6	20.05
Deb.1 P_5	7373.5	0.0025	82.95	348.3	117.9	270.9	20.05
Chaser to Deb.1 P_5	7373.0	0.0015	82.94	348.2	107.9	269.9	19.82
Deb.1 P_6	7374.4	0.0019	82.95	348.5	122.3	212.7	19.82
Chaser to Deb.1 P_6	7373.9	0.0009	82.96	348.4	132.3	213.7	19.82
Chaser and Deb.1 de-orbit	6579.0	0.0006	82.95	318.8	149.8	287.4	32.90
Debris 2 initial	7349.0	0.0049	82.94	354.1	283.1	86.03	N/A
Chaser to Deb.2 initial	7348.5	0.0039	82.95	301.2	288.5	87.03	19.23
Deb.2 P_1	7345.9	0.0055	82.94	300.8	76.23	76.54	71.96
Chaser to Deb.2 P_1	7345.4	0.0045	82.93	300.7	86.23	77.54	19.24
Deb.2 P_2	7348.3	0.0053	82.94	300.8	79.71	89.17	71.96
Chaser to Deb.2 P_2	7348.4	0.0043	82.93	300.9	85.03	90.17	19.24
Chaser and Deb.2 de-orbit	6579.0	0.0026	82.99	271.5	348.0	41.46	32.51
Debris 3 initial	7342.6	0.0029	82.91	347.3	60.47	348.6	N/A
Chaser to Deb.3 initial	7342.1	0.0035	82.92	254.3	70.47	349.6	19.27
Deb.3 P_1	7349.5	0.0030	82.91	253.9	35.22	310.7	123.7
Chaser to Deb.3 P_1	7349.0	0.0020	82.92	253.9	44.15	311.7	19.34
Deb.3 P_2	7337.9	0.0019	82.90	254.4	44.18	13.30	124.0
Chaser to Deb.3 P_2	7337.4	0.0009	82.91	254.3	34.18	12.30	19.15
Deb.3 P_3	7340.8	0.0037	82.91	254.5	37.22	190.9	123.8
Chaser to Deb.3 P_3	7340.3	0.0027	82.92	254.4	27.22	189.9	16.97
Deb.3 P_4	7343.3	0.0025	82.91	254.4	49.73	270.7	123.9
Chaser to Deb.3 P_4	7342.8	0.0015	82.92	254.3	59.7	271.7	19.39
Deb.3 P_5	7340.0	0.0027	82.91	254.3	58.64	250.6	124.0
Chaser to Deb.3 P_5	7339.5	0.0017	82.92	254.2	68.64	251.6	19.58
Deb.3 P_6	7346.9	0.0033	82.91	254.2	43.34	109.5	124.2
Chaser to Deb.3 P_6	7346.3	0.0023	82.92	254.1	53.34	110.5	19.24
Deb.3 P_7	7335.1	0.0035	82.91	254.4	64.84	225.7	123.9
Chaser to Deb.3 P_7	7334.6	0.0025	82.92	254.3	74.84	226.7	19.39
Deb.3 P_8	7339.1.0	0.0028	82.91	254.3	60.47	245.9	124.0
Chaser to Deb.3 P_8	7338.6	0.0018	82.92	254.2	70.47	246.9	19.39
Chaser and Deb.3 de-orbit	6579.0	0.0012	82.91	225.2	6.912	224.2	31.90
Debris 4 initial	7349.0	0.0043	82.94	339.8	120.0	259.4	N/A
Chaser to Deb.4 initial	7348.5	0.0033	82.93	207.0	110.0	258.4	19.74
Deb.4 P_1	7336.7	0.0041	82.93	208.6	0.505	115.2	175.7
Chaser to Deb.4 P_1	7336.2	0.0031	82.94	208.5	10.51	116.2	19.28
Deb.4 P_2	7346.3	0.0033	82.93	209.0	23.65	7.312	175.2
Chaser to Deb.4 P_2	7345.8	0.0023	82.94	208.9	13.65	6.312	19.19
Deb.4 P_3	7340.6	0.0029	82.93	209.0	29.36	280.6	175.1
Chaser to Deb.4 P_3	7340.1	0.0019	82.94	208.9	39.36	281.6	19.19
Chaser and Deb.4 de-orbit	6579.0	0.0007	82.95	179.5	357.7	152.4	32.36
Debris 5 initial	7352.8	0.0027	82.95	331.0	227.9	85.10	N/A
Chaser to Deb.5 initial	7352.3	0.0017	82.94	163.2	237.9	84.10	19.19
Deb.5 P_1	7348.6	0.0021	82.95	163.2	325.6	103.6	226.7
Chaser to Deb.5 P_1	7348.1	0.0011	82.94	163.1	315.6	104.6	19.13
Deb.5 P_2	7358.2	0.0029	82.95	163.3	1.915	143.1	226.6
Chaser to Deb.5 P_2	7357.7	0.0019	82.94	163.2	11.92	142.1	19.15
Deb.5 P_3	7355.0	0.0032	82.95	163.3	1.435	224.0	226.6
Chaser to Deb.5 P_3	7354.6	0.0022	82.94	163.4	11.44	223.0	19.19
Deb.5 P_4	7347.8	0.0023	82.95	163.2	324.1	109.2	226.7
Chaser to Deb.5 P_4	7347.3	0.0013	82.94	163.1	314.1	110.2	19.13
Deb.5 P_5	7352.8	0.0033	82.95	163.3	351.2	136.1	226.6
Chaser to Deb.5 P_5	7352.3	0.0023	82.94	163.4	341.2	135.1	19.13
Chaser and Deb.5 de-orbit	6579.0	0.0026	82.94	133.8	199.7	219.7	32.76
Total Time:	N/A	N/A	N/A	N/A	N/A	N/A	259.4

Table A.1: Transfer iteration results set 1

Transfer Description	a (km)	e	I (deg)	Ω (deg)	ω (deg)	θ (deg)	Time (days)
Debris 1 initial	7145.9	0.0012	74.01	176.6	168.5	2.414	N/A
Chaser to Deb.1 initial	7146.0	0.0016	74.00	151.1	158.5	22.44	14.63
Deb.1 P_1	7141.1	0.0015	74.00	149.6	167.4	159.1	14.63
Chaser to Deb.1 P_1	7140.6	0.0005	73.99	149.6	177.4	158.1	14.59
Deb.1 P_2	7129.5	0.0013	73.99	149.6	224.1	230.9	14.59
Chaser to Deb.1 P_2	7129.0	0.0023	73.98	149.5	214.1	229.9	14.61
Deb.1 P_3	7144.1	0.0013	74.01	149.6	169.6	31.71	14.61
Chaser to Deb.1 P_3	7143.6	0.0009	74.00	149.6	167.5	30.71	14.61
Chaser and Deb.1 de-orbit	6579.0	0.0009	73.99	100.8	150.9	142.3	23.63
Debris 2 initial	7365.1	0.0029	82.94	65.92	2.661	13.79	N/A
Chaser to Deb.2 initial	7365.6	0.0011	82.94	338.9	91.86	13.69	80.12
Deb.2 P_1	7349.8	0.0034	82.93	338.2	359.1	104.2	118.4
Chaser to Deb.2 P_1	7349.3	0.0024	82.94	338.1	349.1	103.2	78.97
Deb.2 P_2	7364.2	0.0035	82.94	339.0	35.27	225.1	117.2
Chaser to Deb.2 P_2	7363.7	0.0025	82.93	339.1	25.27	224.1	79.07
Deb.2 P_3	7363.0	0.0030	82.94	339.0	23.62	309.8	117.3
Chaser to Deb.2 P_3	7362.5	0.0023	82.94	339.1	33.60	308.8	79.07
Chaser and Deb.2 de-orbit	6579.1	0.0026	82.93	308.6	349.2	46.35	32.40
Total Time:	N/A	N/A	N/A	N/A	N/A	N/A	149.7

Table A.2: Transfer iteration results set 2

Transfer Description	a (km)	e	i (deg)	Ω (deg)	ω (deg)	θ (deg)	Time (days)	Fuel Mass (kg)
Chaser to drift 1	6877.6	0.0006	98.64	331.7	144.6	355.9	9.762	42.99
Drift 1	6885.2	0.0016	98.63	332.4	172.7	12.67	0.600	0.000
Deb. 1 P_1	7169.2	0.0008	98.43	341.0	39.54	140.3	18.39	N/A
Drift 1 to Deb. 1 P_1	7168.8	0.0003	98.44	341.0	29.54	139.3	8.030	35.60
Chaser and deb.1 de-orbit	6578.5	0.0002	98.42	61.60	123.8	46.27	77.74	344.6
Deb 1 Total	N/A	N/A	N/A	N/A	N/A	N/A	96.13	423.2
Chaser to drift 2	6878.5	0.0033	102.8	129.1	118.8	170.0	42.87	188.8
Drift 2	6883.7	0.0007	102.8	246.8	112.7	196.1	70.12	0.000
Deb. 2 P_1	7038.5	0.0018	97.88	250.4	300.7	45.08	209.1	N/A
Drift 2 to Deb.2 P_1	7038.0	0.0010	97.88	250.3	190.7	44.08	44.5	199.9
Deb. 2 P_2	7045.3	0.0014	97.89	290.8	130.0	134.6	253.6	N/A
Drift 2 to Deb.2 P_2	7045.8	0.0020	97.89	290.9	139.3	135.6	45.56	201.0
Deb. 2 P_3	7058.8	0.0022	97.91	292.4	220.1	264.6	254.7	N/A
Drift 2 to Deb.2 P_3	7058.4	0.0030	97.90	292.3	214.4	263.6	45.55	200.6
Chaser and deb.2 de-orbit	6574.8	0.0038	97.92	331.7	71.95	267.0	36.17	159.3
Deb.2 Total	N/A	N/A	N/A	N/A	N/A	N/A	194.7	548.7
Chaser to drift 3	6878.2	0.0040	99.74	0.004	14.32	162.4	21.36	94.04
Drift 3	6850.0	0.0059	99.74	10.62	53.92	161.8	8.043	0.000
Deb. 3 P_1	7124.8	0.0064	98.30	35.75	34.70	211.1	320.2	N/A
Drift 3 to Deb.3 P_1	7124.3	0.0075	98.31	35.65	24.70	210.1	20.40	88.04
Deb. 3 P_2	7133.8	0.0084	98.31	30.75	16.54	211.3	340.7	N/A
Drift 3 to Deb.3 P_2	7133.5	0.0082	98.31	30.76	11.08	241.7	20.42	89.93
Chaser and deb.3 de-orbit	6578.5	0.0029	98.32	142.6	34.58	234.7	114.1	502.3
Deb.3 Total	N/A	N/A	N/A	N/A	N/A	N/A	163.9	686.3
Chaser to drift 4	6879.1	0.0022	99.18	159.3	327.5	258.8	13.95	61.43
Drift 4	6871.0	0.0028	99.19	218.9	146.4	291.1	49.00	0.000
Deb. 4 P_1	7170.5	0.0049	98.44	220.9	123.8	89.65	517.7	N/A
Drift 4 to Deb.4 P_1	7171.0	0.0051	98.45	230.0	133.8	90.40	14.92	56.98
Deb. 4 P_2	7169.7	0.0052	98.46	232.5	80.18	120.3	532.6	N/A
Drift 4 to Deb.4 P_2	7169.4	0.0043	98.46	232.4	72.60	119.3	12.58	55.40
Chaser and deb.4 de-orbit	6578.5	0.0041	98.46	275.7	167.5	310.7	43.40	191.1
Deb.4 Total	N/A	N/A	N/A	N/A	N/A	N/A	118.9	307.9
Chaser to drift 5	6880.0	0.0051	102.6	339.8	33.63	78.15	45.64	201.0
Drift 5	6886.4	0.0032	102.6	59.32	271.6	314.6	48.10	0.000
Deb. 5 P_1	7390.9	0.0039	100.3	110.6	75.4	93.00	667.4	N/A
Drift 5 to Deb.5 P_1	7390.4	0.0029	100.3	110.7	81.38	93.42	39.34	170.2
Deb. 5 P_2	7384.4	0.0029	99.23	112.0	267.4	127.7	706.7	N/A
Drift 5 to Deb.5 P_2	7383.9	0.0019	99.23	111.9	259.3	126.9	36.35	165.8
Deb. 5 P_3	7385.1	0.0024	99.23	112.7	27.89	12.45	707.6	N/A
Drift 5 to Deb.5 P_3	7384.7	0.0018	99.24	112.5	21.98	12.38	37.24	166.6
Chaser and deb.5 de-orbit	6578.9	0.0016	99.24	215.0	236.3	74.35	106.0	466.9
Deb.5 Total	N/A	N/A	N/A	N/A	N/A	N/A	237.0	834.4
Mission Total:	N/A	N/A	N/A	N/A	N/A	N/A	813.6	2800.5

Table A.3: Rendezvous transfer with drift orbit results — all iteration results

Bibliography

[1] T. N. Edelbaum, "Optimum low-thrust rendezvous and station keeping," *AIAA Journal*, vol. 2, no. 7, pp. 1196–1201, 1964.

[2] R. H. Battin, "Solving Lambert's problem," in *An introduction to the mathematics and methods of astrodynamics* (AIAA, ed.), AIAA, 1999.

[3] R. A. Broucke and P. J. Cefola, "On the equinoctial orbit elements," *Celestial Mechanics*, vol. 5, no. 3, pp. 303–310, 1972.

[4] M. A. Patterson and A. V. Rao, "GPOPS-II: A MATLAB software for solving multiple-phase optimal control problems using hp-adaptive Gaussian quadrature collocation methods and sparse nonlinear programming," *ACM Transactions on Mathematical Software (TOMS)*, vol. 41, no. 1, p. 1, 2014.

[5] N. Pavlis, S. Kenyon, J. Factor, and S. Holmes, "Earth gravitational model 2008," in *SEG Technical Program Expanded Abstracts 2008*, pp. 761–763, Society of Exploration Geophysicists, 2008.

[6] P. R. Bond, ed., *Janes Space Systems & Industry Yearbook 18/19*. IHS Markit, 2019.

[7] J. N. Pelton, S. Madry, and S. Camacho-Lara, *Handbook of satellite applications*. Springer, 2017.

[8] B. Lal, A. Balakrishnan, B. M. Caldwell, R. S. Buenconsejo, and S. A. Carioscia, "Global trends in space situational awareness (ssa) and space traffic management (stm)," *IDA Science & Technology Policy Institute, Available online at https://www. ida. org/idamedia/Corporate/Files/Publications/STPIPubs/2018/D-9074. pdf*, 2018.

[9] UCS, "Union of concerned scientists satellite database." Website: http://www.ucsusa.org/nuclear-weapons/space-weapons/satellite-database, Apr. 2020. Accessed: [Sept, 2020].

BIBLIOGRAPHY

[10] NASA, "NASA space science data coordinated achive." Website: `https://nssdc.gsfc.nasa.gov/nmc/spacecraft/display.action?id=1957-001B`, May 2020. Accessed: [Sept, 2020].

[11] D. J. Kessler and B. G. Cour-Palais, "Collision frequency of artificial satellites: the creation of a debris belt," *Journal of Geophysical Research: Space Physics*, vol. 83, no. A6, pp. 2637–2646, 1978.

[12] JSpOC, "Two-line elements." Website: `https://www.space-track.org/auth/login`, September 2020. Accessed: [Sept., 2020].

[13] L. Hall, "The history of space debris," *Space Traffic Management Conference*, 2014.

[14] European Space Agency, "Position paper on space debris mitigation: Implementing zero debris creation zones," tech. rep., ESA, 2005.

[15] C. Pardini and L. Anselmo, "Review of past on-orbit collisions among cataloged objects and examination of the catastrophic fragmentation concept," *Acta Astronautica*, vol. 100, pp. 30–39, 2014.

[16] T. Kelso *et al.*, "Analysis of the Iridium 33 Cosmos 2251 collision," in *Advanced Maui Optical and Space Surveilance Technologies Conference (AMOS)*, (Hawaii, USA), 2009.

[17] N. L. Johnson, "Orbital debris: the growing threat to space operations," *NASA*, 2010.

[18] D. S. Portree, *Orbital debris: A chronology*. NASA, 1999.

[19] ESA, "Space debris by the numbers." Website: `https://www.esa.int/Safety_Security/Space_Debris/Space_debris_by_the_numbers`, Feb. 2020. Accessed: [March. 11,2020].

[20] ESA, "How many space debris objects are currently in orbit." Website: `http://www.esa.int/Our_Activities/Space_Engineering_Technology/Clean_Space/How_many_space_debris_objects_are_currently_in_orbit`, July 2013. Accessed: [Oct. 11, 2016].

BIBLIOGRAPHY

[21] NASA, "Space debris and human spacecraft." Website: http://www.nasa.gov/mission_pages/station/news/orbital_debris.html, September 2013. Accessed: [Oct. 11, 2016].

[22] CSA, "National research on space debris, safety of space objects with nuclear power sources on board and problems relating to their collision with space debris," in *Committee on the Peaceful Uses of Outer Space Scientific and Technical Subcommittee Fifty-second session*, 2015.

[23] ISO-24113:2019, *Space systems - Space debris mitigation requirements*. pub-ISO ISO/TC 20/SC 14 Space systems and operations, 2019.

[24] J. Liou and N. L. Johnson, "Risks in space from orbiting debris," *SCIENCE-NEW YORK THEN WASHINGTON*-, vol. 311, no. 5759, p. 340, 2006.

[25] D. S. McKnight, F. Di Pentino, A. Kaczmarek, and P. Dingman, "System engineering analysis of derelict collision prevention options," *Acta Astronautica*, vol. 89, pp. 248–253, 2013.

[26] J. Liou, "A parametric study on using active debris removal for LEO environment remediation," *Adv Space Res*, vol. 47, no. 11, pp. 1865–1876, 2011.

[27] L. Vance and A. Mense, "Value analysis for orbital debris removal," *Advances in Space Research*, vol. 52, no. 4, pp. 685–695, 2013.

[28] D. S. McKnight and F. R. Di Pentino, "New insights on the orbital debris collision hazard at GEO," *Acta Astronautica*, vol. 85, pp. 73–82, 2013.

[29] E. Alessi, A. Rossi, G. Valsecchi, L. Anselmo, C. Pardini, C. Colombo, H. Lewis, J. Daquin, F. Deleflie, M. Vasile, *et al.*, "Effectiveness of GNSS disposal strategies," *Acta Astronautica*, vol. 99, pp. 292–302, 2014.

[30] A. Rossi, E. Alessi, G. Valsecchi, H. Lewis, C. Colombo, L. Anselmo, C. Pardini, F. Deleflie, and K. Merz, "The effect of the GNSS disposal strategies on the long term evolution of the MEO region," in *67 th International Astronautical Congress (IAC)*, (Guadalajara, Mexico), 2016.

BIBLIOGRAPHY

[31] C. Colombo, F. Letizia, H. G. Lewis, *et al.*, "Spatial density approach for modelling the space debris population," *26th AAS/AIAA Sp. Flight Mech. Meet., AAS*, pp. 16–465, 2016.

[32] J. Liou, "USA space debris environment, operations, and research updates," *55th Session of the Scientific and Technical Subcommittee Committee on the Peaceful Uses of Outer Space, UN*, 2018.

[33] C. Wiedemann, S. Flegel, M. Möckel, J. Gelhaus, V. Braun, C. Kebschull, J. Kreisel, M. Metz, and P. Vörsmann, "Cost estimation of active debris removal," in *63rd International Astronautical Congress*, (Naples, Italy), 2012.

[34] M. Sansegundo and M. A. Molina, "Space debris in routine satellite operations: Risk mitigation for collision avoidance," *SpaceOps 2010 Conference,* (Huntsville, Alabama), 2010.

[35] ESA, "Copernicus Sentinel-1A satellite hit by space particle." Website: http://www.esa.int/Our_Activities/Observing_the_Earth/ Copernicus/Sentinel-1/Copernicus_Sentinel-1A_satellite_ hit_by_space_particle, August 2016. Accessed: [Oct. 11, 2016].

[36] H. Klinkrad, J. Alarcon, and N. Sanchez, "Collision avoidance for operational ESA satellites," in *4th European Conference on Space Debris*, vol. 587, p. 509, 2005.

[37] M. Emanuelli, G. Federico, J. Loughman, D. Prasad, T. Chow, and M. Rathnasabapathy, "Conceptualizing an economically, legally, and politically viable active debris removal option," *Acta Astronautica*, vol. 104, no. 1, pp. 197–205, 2014.

[38] M. Ansdell, "Active space debris removal: Needs, implications, and recommendations for today's geopolitical environment," *Journal of Public and International Affairs*, vol. 21, pp. 7–22, 2010.

[39] T. Martin, E. Pérot, M.-C. Desjean, and L. Bitetti, "Active debris removal mission design in low earth orbit," in *Progress in Propulsion Physics*, vol. 4, pp. 763–788, EDP Sciences, 2013.

[40] N. L. Johnson and H. Klinkrad, "Space debris environment remediation concepts," *5th European Conference on Space Debris,* (Darmstadt, Germany), 2009.

[41] M. Shan, J. Guo, and E. Gill, "Review and comparison of active space debris capturing and removal methods," *Progress in Aerospace Sciences*, vol. 80, pp. 18–32, 2016.

[42] C. P. Mark and S. Kamath, "Review of active space debris removal methods," *Space Policy*, vol. 47, pp. 194–206, 2019.

[43] M. Andrenucci, P. Pergola, and A. Ruggiero, "Active removal of space debris-expanding foam application for active debris removal," *ESA Report*, 2011.

[44] L. Visagie, V. Lappas, and S. Erb, "Drag sails for space debris mitigation," *Acta Astronautica*, vol. 109, pp. 65–75, 2015.

[45] G. Bonin, J. Hiemstra, T. Sears, and R. Zee, "The canx-7 drag sail demonstration mission: enabling environmental stewardship for nano-and microsatellites," *27 th Annual AIAA/USU Conference on Small Satellites*, 2013.

[46] C. Underwood, A. Viquerat, M. Schenk, B. Taylor, C. Massimiani, R. Duke, B. Stewart, S. Fellowes, C. Bridges, G. Aglietti, *et al.*, "Inflatesail de-orbit flight demonstration results and follow-on drag-sail applications," *Acta Astronautica*, vol. 162, pp. 344–358, 2019.

[47] M. Cartmell and D. McKenzie, "A review of space tether research," *Progress in Aerospace Sciences*, vol. 44, no. 1, pp. 1–21, 2008.

[48] Y. Yamaigiwa, E. Hiragi, and T. Kishimoto, "Dynamic behavior of electrodynamic tether deorbit system on elliptical orbit and its control by Lorentz force," *Aerospace science and technology*, vol. 9, no. 4, pp. 366–373, 2005.

[49] L. Savioli, A. Francesconi, F. Maggi, L. Olivieri, E. Lorenzini, and C. Pardini, "Space debris removal using multi-mission modular spacecraft," *Navigation*, vol. 12, pp. 7–5, 2013.

[50] H. Wen, D. Jin, and H. Hu, "Three-dimensional deployment of electro-dynamic tether via tension and current control with constraints," *Acta Astronautica*, vol. 129, pp. 253–259, 2016.

[51] S. Chen, A. Li, C. Wang, and C. Liu, "Adaptive sliding mode control for deployment of electro-dynamic tether via limited tension and current," *Acta Astronautica*, 2019.

[52] C. Bombardelli and J. Pelaez, "Ion beam shepherd for contactless space debris removal," *Journal of Guidance, Control, and Dynamics*, vol. 34, no. 3, pp. 916–920, 2011.

[53] S. Kitamura, Y. Hayakawa, and S. Kawamoto, "A reorbiter for large GEO space debris using ion beam irradiation," *Proc. 32nd IEPC, Wiesbaden, Germany*, vol. 23, 2011.

[54] C. R. Phipps, "L'adroit–a spaceborne ultraviolet laser system for space debris clearing," *Acta Astronautica*, vol. 104, no. 1, pp. 243–255, 2014.

[55] M. Schmitz, S. Fasoulas, and J. Utzmann, "Performance model for space-based laser debris sweepers," *Acta Astronautica*, vol. 115, pp. 376–383, 2015.

[56] S. Tragesser, L. Sandager, and S. Harder, "Laboratory demonstration of a tether sling for space transportation," in *AIAA SPACE 2009 Conference & Exposition*, p. 6660, 2009.

[57] P. Williams, "Dynamics and control of spinning tethers for rendezvous in elliptic orbits," *Journal of Vibration and Control*, vol. 12, no. 7, pp. 737–771, 2006.

[58] S. G. Tragesser and B. Gorjidooz, "Open-loop spinup and deployment control of a tether sling," *Journal of Spacecraft and Rockets*, vol. 47, no. 2, pp. 345–352, 2010.

[59] J. Missel and D. Mortari, "Removing space debris through sequential captures and ejections," *Journal of Guidance, Control, and Dynamics*, vol. 36, no. 3, pp. 743–752, 2013.

[60] J. Missel and D. Mortari, "Path optimization for space sweeper with sling-sat: A method of active space debris removal," *Advances in Space Research*, vol. 52, no. 7, pp. 1339–1348, 2013.

[61] H. Schaub and D. F. Moorer Jr, "Geosynchronous large debris reorbiter: challenges and prospects," *The Journal of the Astronautical Sciences*, vol. 59, no. 1-2, pp. 161–176, 2012.

[62] H. Schaub and Z. Sternovsky, "Active space debris charging for contactless electrostatic disposal maneuvers," *Advances in Space Research*, vol. 53, no. 1, pp. 110–118, 2014.

[63] C. Foster, J. Bellerose, D. Mauro, and B. Jaroux, "Mission concepts and operations for asteroid mitigation involving multiple gravity tractors," *Acta Astronautica*, vol. 90, no. 1, pp. 112–118, 2013.

[64] H. Nakanishi and K. Yoshida, "The tako (target collaborativize) flyer: a new concept for future satellite servicing," in *Smaller Satellites: Bigger Business?*, pp. 397–399, Springer, 2002.

[65] M. J.-C. Meyer, M. M. Scheper, R. Janovsky, M. J. V. Mato, M. G. Taubmann, M. J. C. Eguen, and M. R. Le Letty, "Clamping mechanism–a tentacles based capture mechanism for active debris removal," *65th International Astronautical Congress (IAC),* (Toronto, Canada), 2014.

[66] A. Chiesa, F. Fossati, G. Gambacciani, and E. Pensavalle, "Enabling technologies for active space debris removal: the cadet project," in *Space Safety is No Accident*, pp. 29–38, Springer, 2015.

[67] S. Ferraris, S. Perero, G. G. di Confiengo, A. Chiesa, A. Messidoro, and M. Ferraris, "Friction, mechanical and ageing properties of surface modified materials for space debris capture," *Advances in Space Research*, vol. 57, no. 5, pp. 1177–1188, 2016.

[68] M. M. Castronuovo, "Active space debris removal–a preliminary mission analysis and design," *Acta Astronautica*, vol. 69, no. 9–10, pp. 848 – 859, 2011.

[69] M. Wilde, J. T. Harder, and E. Stoll, "On-orbit servicing and active debris removal: Enabling a paradigm shift in spaceflight," *Frontiers in Robotics and AI*, vol. 6, p. 136, 2019.

[70] P. Gasbarri and A. Pisculli, "Dynamic/control interactions between flexible orbiting space-robot during grasping, docking and post-docking manoeuvres," *Acta Astronautica*, vol. 110, pp. 225–238, 2015.

[71] T. C. Nguyen-Huynh and I. Sharf, "Adaptive reactionless motion and parameter identification in postcapture of space debris," *Journal of Guidance, Control, and Dynamics*, vol. 36, no. 2, pp. 404–414, 2013.

[72] S. Xu, H. Wang, D. Zhang, and B. Yang, "Adaptive zero reaction motion control for free-floating space manipulators," *arXiv preprint arXiv:1402.5586*, 2014.

[73] L. Felicetti, P. Gasbarri, A. Pisculli, M. Sabatini, and G. B. Palmerini, "Design of robotic manipulators for orbit removal of spent launchers' stages," *Acta Astronautica*, vol. 119, pp. 118 – 130, 2016.

[74] B. P. McCarthy, *Flight hardware development for a space-based robotic assembly and servicing testbed*. PhD thesis, Massachusetts Institute of Technology, 2014.

[75] K. Yoshida, R. Kurazume, and Y. Umetani, "Dual arm coordination in space free-flying robot," in *Robotics and Automation, 1991. Proceedings., 1991 IEEE International Conference on*, pp. 2516–2521, IEEE, 1991.

[76] S. V. Shah, I. Sharf, and A. K. Misra, "Reactionless path planning strategies for capture of tumbling objects in space using a dualarm robotic system," in *AIAA Guidance, Navigation and Control Conference*, vol. 2013, 2005.

[77] K. Yoshida, "Achievements in space robotics.," *IEEE Robot. Automat. Mag.*, vol. 16, no. 4, pp. 20–28, 2009.

[78] R. Biesbroek, L. Innocenti, A. Wolahan, and S. M. Serrano, "e.Deorbit–ESA's active debris removal mission," in *Proceedings of the 7th European Conference on Space Debris*, p. 10, ESA Space Debris Office, 2017.

[79] K. Wormnes, R. Le Letty, L. Summerer, R. Schonenborg, O. Dubois-Matra, E. Luraschi, A. Cropp, H. Krag, and J. Delaval, "ESA technologies for space debris remediation," in *6th European Conference on Space Debris,*, (Darmstadt, Germany), pp. 22–25, 2013.

[80] J. Reed and S. Barraclough, "Development of harpoon system for capturing space debris," in *ESA Special Publication*, vol. 723, p. 174, 2013.

[81] R. Dudziak, S. Tuttle, and S. Barraclough, "Harpoon technology development for the active removal of space debris," *Advances in Space Research*, vol. 56, no. 3, pp. 509–527, 2015.

[82] A. Medina, L. Cercos, R. Stefanescu, R. Benvenuto, M. Lavagna, I. Gonzalez, N. Rodriguez, and K. Ormnes, "Capturing nets for active debris removal: a follow-up microgravity experiment design to validate flexible dynamic models," in *13th Symposium on Advanced Space Technologies in Automation and Robotics*, (Noordwijk, Netherlands), pp. 1–8, 2015.

[83] E. M. Botta, I. Sharf, A. K. Misra, and M. Teichmann, "On the simulation of tether-nets for space debris capture with vortex dynamics," *Acta Astronautica*, vol. 123, pp. 91–102, 2016.

[84] Z. Guang and Z. Jing-rui, "Space tether net system for debris capture and removal," in *2012 4th International Conference on Intelligent Human-Machine Systems and Cybernetics*, vol. 1, pp. 257–261, IEEE, 2012.

[85] H. Liu, Q. Zhang, L. Yang, Y. Zhu, and Y. Zhang, "Dynamics of tether-tugging reorbiting with net capture," *Science China Technological Sciences*, vol. 57, no. 12, pp. 2407–2417, 2014.

[86] J. L. Forshaw, G. S. Aglietti, S. Fellowes, T. Salmon, I. Retat, A. Hall, T. Chabot, A. Pisseloup, D. Tye, C. Bernal, *et al.*, "The active space debris removal mission RemoveDebris. Part 1: from concept to launch," *Acta Astronautica*, vol. 168, pp. 293–309, 2020.

154

[87] G. S. Aglietti, B. Taylor, S. Fellowes, T. Salmon, I. Retat, A. Hall, T. Chabot, A. Pis-seloup, C. Cox, A. Mafficini, *et al.*, "The active space debris removal mission RemoveDebris. Part 2: in orbit operations," *Acta Astronautica*, vol. 168, pp. 310–322, 2020.

[88] V. Aslanov and V. Yudintsev, "Dynamics of large space debris removal using tethered space tug," *Acta Astronautica*, vol. 91, pp. 149–156, 2013.

[89] S. E. Becker M. and R. I., "Tether force transmission capabilities for applications at active debris removal missions," in *67 th International Astronautical Congress*, (Guadalajara, Mexico), 2016.

[90] V. S. Aslanov and V. V. Yudintsev, "Dynamics, analytical solutions and choice of parameters for towed space debris with flexible appendages," *Advances in Space Research*, vol. 55, no. 2, pp. 660–667, 2015.

[91] V. S. Aslanov, "Chaos behavior of space debris during tethered tow," *Journal of Guidance, Control, and Dynamics*, pp. 1–7, 2015.

[92] H. Linskens and E. Mooij, "Tether dynamics analysis and guidance and control design for active space-debris removal," *Journal of Guidance, Control, and Dynamics*, vol. 39, pp. 1232–1243, 2016.

[93] K. Hovell and S. Ulrich, "Attitude stabilization of an uncooperative spacecraft in an orbital environment using visco-elastic tethers," in *AIAA Guidance, Navigation, and Control Conference*, p. 0641, 2016.

[94] S. Cleary and W. J. O'Connor, "Control of space debris using an elastic tether and wave-based control," *Journal of Guidance, Control, and Dynamics*, vol. 39, pp. 1392–1406, Apr. 2016.

[95] L. Jasper and H. Schaub, "Input shaped large thrust maneuver with a tethered debris object," *Acta Astronautica*, vol. 96, pp. 128–137, 2014.

[96] L. Jasper and H. Schaub, "Tethered towing using open-loop input-shaping and discrete thrust levels," *Acta Astronautica*, vol. 105, no. 1, pp. 373–384, 2014.

[97] M. O'Connor, S. Clearly, and D. Hayden, "Debris de-tumbling and de-orbiting by elastic tether and wave-based control," in *6th International Conference on Astrodynamics Tools and Techniques.*, (Darmstadt, Germany), pp. 14–17, 2016.

[98] N. Van der Pas, J. Lousada, C. Terhes, M. Bernabeu, and W. Bauer, "Target selection and comparison of mission design for space debris removal by DLR's advanced study group," *Acta Astronautica*, vol. 102, pp. 241–248, 2014.

[99] S. Kawamoto, N. Nagaoka, T. Sato, and T. Hanada, "Impact on collision probability by post mission disposal and active debris removal," *Journal of Space Safety Engineering*, 2020.

[100] M. Jankovic and F. Kirchner, "Taxonomy of LEO space debris population for ADR selection," in *67 th International Astronautical Congress*, (Guadalajara, Mexico), 2016.

[101] T. Yamamoto, H. Okamoto, and S. Kawamoto, "Cost analysis of active debris removal scenarios and system architectures," in *7th European Conference on Space Debris*, vol. 7, 2017.

[102] S. Tonetti, S. Cornara, M. Faenza, O. Verberne, T. Langener, and G. V. de Miguel, "Active debris removal and space debris mitigation using hybrid propulsion solutions," in *Stardust final conference*, pp. 163–180, Springer, 2018.

[103] J. T. Betts, "Very low-thrust trajectory optimization using a direct SQP method," *Journal of Computational and Applied Mathematics*, vol. 120, no. 1, pp. 27–40, 2000.

[104] J. T. Betts, *Practical methods for optimal control and estimation using nonlinear programming*, vol. 19. Siam, 2010.

[105] S. Hernandez and M. R. Akella, "Energy preserving low-thrust guidance for orbit transfers in KS variables," *Celestial Mechanics and Dynamical Astronomy*, vol. 125, no. 1, pp. 107–132, 2016.

[106] Airbus, "Ion propulsion systems." Website: http://www.space-propulsion.com/spacecraft-propulsion/ion-propulsion/index.html, 2003. Accessed: [March. 18, 2017].

[107] J. L. Shannon, M. T. Ozimek, J. A. Atchison, and C. M. Hartzell, "Q-Law aided direct trajectory optimization of many-revolution low-thrust transfers," *Journal of Spacecraft and Rockets*, pp. 1–11, 2020.

[108] A. A. Lidtke, H. G. Lewis, R. Armellin, and H. Urrutxua, "Considering the collision probability of active debris removal missions," *Acta Astronautica*, vol. 131, pp. 10–17, 2017.

[109] B. Larbi, M. Grzesik, B. Radtke, C. Trentlage, and E. Stoll, "Active debris removal for mega constellations: Cubesat possible," in *Proceedings of the 9th International Workshop on Satellite Constellations and Formation Flying IWSCFF2017, Boulder, Colorado*, 2017.

[110] B. Chamot, "Mission and system architecture design for active removal of rocket bodies in low earth orbit," *Master's thesis, Massachusetts Institute of Technology, US*, 2012.

[111] J. Peyrard, M. Graziano, L. Strippoli, J. Olson, and K. Benzin, "ADR GNC concept for the Dream Chaser ® spacecraft: The Envisat deorbiting case," in *67th International Astronautical Congress (IAC)*, 2016.

[112] L. Anselmo and C. Pardini, "An index for ranking active debris removal targets in LEO," in *7th European Conference on Space Debris. ESA Space Debris Office, Darmstadt-ESOC*, pp. 18–21, 2017.

[113] L. Anselmo and C. Pardini, "Ranking upper stages in low earth orbit for active removal," *Acta Astronautica*, vol. 122, pp. 19–27, 2016.

[114] L. Jasper, P. Anderson, H. Schaub, and D. S. McKnight, "Economic and risk challenges of operating in the current space debris environment," in *Third European Workshop on Space Debris Modeling and Remediation, Paris, France*, 2014.

BIBLIOGRAPHY

[115] B. W. Barbee, S. Alfano, E. Pinon, K. Gold, and D. Gaylor, "Design of spacecraft missions to remove multiple orbital debris objects," in *Aerospace Conference, 2011 IEEE*, pp. 1–14, IEEE, 2011.

[116] M. Kanazaki, Y. Yamada, and M. Nakamiya, "Trajectory optimization of a satellite for multiple active space debris removal based on a method for the traveling service-man problem," in *2017 21st Asia Pacific Symposium on Intelligent and Evolutionary Systems (IES)*, pp. 61–66, IEEE, 2017.

[117] H.-X. Shen, T.-J. Zhang, L. Casalino, and D. Pastrone, "Optimization of active debris removal missions with multiple targets," *Journal of Spacecraft and Rockets*, vol. 55, no. 1, pp. 181–189, 2018.

[118] D. Grishko, A. Baranov, and N. Chernov, "Refinement of parameters of a space vehicle destined for large-size space debris flyby in LEO using detachable thruster de-orbiting kits," in *67th International Astronautical Congress, Guadalajara, Mexico.*, 2016.

[119] M. Cerf, "Multiple space debris collecting mission: Optimal mission planning," *Journal of Optimization Theory and Applications*, vol. 167, no. 1, pp. 195–218, 2015.

[120] S. Zhao, J. Zhang, K. Xiang, and R. Qi, "Target sequence optimization for multiple debris rendezvous using low thrust based on characteristics of SSO," *Astrodynamics*, vol. 1, no. 1, pp. 85–99, 2017.

[121] J. Bang and J. Ahn, "Multitarget rendezvous for active debris removal using multiple spacecraft," *Journal of Spacecraft and Rockets*, vol. 56, no. 4, pp. 1237–1247, 2019.

[122] A. Froehlich, *Space Security and Legal Aspects of Active Debris Removal*. Springer, 2019.

[123] R. S. Jakhu, Y. O. M. Nyampong, and T. Sgobba, "Regulatory framework and organization for space debris removal and on orbit servicing of satellites," *Journal of Space Safety Engineering*, vol. 4, no. 3-4, pp. 129–137, 2017.

[124] M. R. Migaud, "Protecting earth's orbital environment: Policy tools for combating space debris," *Space Policy*, p. 101361, 2020.

[125] C. R. Rajapaksa and J. K. Wijerathna, "Adaptation to space debris mitigation guidelines and space law," *Astropolitics*, vol. 15, no. 1, pp. 65–76, 2017.

[126] R. P. Patera and W. H. Ailor, "The realities of reentry disposal," in *Proceedings of the AAS/AIAA Space Flight Mechanics Meeting*, pp. 9–11, American Astronautical Society/AIAA Monterey, California, 1998.

[127] W. Ailor and R. Patera, "Spacecraft re-entry strategies: meeting debris mitigation and ground safety requirements," *Proceedings of the Institution of Mechanical Engineers, Part G: Journal of Aerospace Engineering*, vol. 221, no. 6, pp. 947–953, 2007.

[128] W. Ailor, "Space debris reentry hazards," *UNOOSA*, Feb. 2012.

[129] IADC, *IADC Space Debris Mitigation Guidelines*. IADC, 2007.

[130] UN, *Space Debris Mitigation Guidelines of the Committee on the Peaceful Uses of Outer Space*, 2010.

[131] R. R. Bate, D. D. Mueller, J. E. White, and W. W. Saylor, *Fundamentals of astrodynamics*. Courier Dover Publications, 2020.

[132] M. Walker, B. Ireland, and J. Owens, "A set modified equinoctial orbit elements," *Celestial mechanics*, vol. 36, no. 4, pp. 409–419, 1985.

[133] K. F. Graham and A. V. Rao, "Minimum-time trajectory optimization of multiple revolution low-thrust earth-orbit transfers," *Journal of Spacecraft and Rockets*, vol. 52, no. 3, pp. 711–727, 2015.

[134] J. A. Kechichian, "Equinoctial orbit elements-application to optimal transfer problems," in *Astrodynamics 1989*, pp. 933–949, 1990.

[135] S. Bruinsma, "The DTM-2013 thermosphere model," *Journal of Space Weather and Space Climate*, vol. 5, p. A1, 2015.

BIBLIOGRAPHY

[136] J. Picone, A. Hedin, D. P. Drob, and A. Aikin, "NRLMSISE-00 empirical model of the atmosphere: Statistical comparisons and scientific issues," *Journal of Geophysical Research: Space Physics*, vol. 107, no. A12, pp. SIA–15, 2002.

[137] B. Bowman, W. K. Tobiska, F. Marcos, C. Huang, C. Lin, and W. Burke, "A new empirical thermospheric density model JB2008 using new solar and geomagnetic indices," in *AIAA/AAS Astrodynamics specialist conference and exhibit*, p. 6438, 2008.

[138] L. Sagnières, "Modeling and simulation of long-term rotational dynamics of large space debris". PhD thesis, McGill University, 2018.

[139] P. Gurfil, "Control-theoretic analysis of low-thrust orbital transfer using orbital elements," *Journal of Guidance, Control, and Dynamics*, vol. 26, no. 6, pp. 979–983, 2003.

[140] "Mathematica, Version 12.1." Wolfram Research, Inc. Champaign, IL, 2020.

[141] D. Garg, M. Patterson, W. W. Hager, A. V. Rao, D. A. Benson, and G. T. Huntington, "A unified framework for the numerical solution of optimal control problems using pseudospectral methods," *Automatica*, vol. 46, no. 11, pp. 1843–1851, 2010.

[142] C. L. Darby, W. W. Hager, and A. V. Rao, "An hp-adaptive pseudospectral method for solving optimal control problems," *Optimal Control Applications and Methods*, vol. 32, no. 4, pp. 476–502, 2011.

[143] A. Waechter, C. Laird, F. Margot, and Y. Kawajir, "Introduction to IPOPT: A tutorial for downloading, installing, and using IPOPT," *Revision*, 2009.

[144] R. Fletcher, S. Leyffer, P. L. Toint, *et al.*, "A brief history of filter methods," *Preprint ANL/MCS-P1372-0906, Argonne National Laboratory, Mathematics and Computer Science Division*, p. 36, 2006.

[145] M. J. Weinstein and A. V. Rao, "Algorithm 984: ADiGator, a toolbox for the algorithmic differentiation of mathematical functions in MATLAB using source transformation via operator overloading," *ACM Transactions on Mathematical Software (TOMS)*, vol. 44, no. 2, p. 21, 2017.

[146] L. Sagnières, "McGill-AML / D-SPOSE github." Website: `https://github.com/McGill-AML/D-SPOSE`, August 2018. Accessed: [Jul. 16, 2020].

[147] L. B. Sagnières and I. Sharf, "Long-term rotational motion analysis and comparison to observations of the inoperative envisat," *Journal of Guidance, Control, and Dynamics*, vol. 42, no. 2, pp. 364–376, 2019.

[148] L. Sagnières, I. Sharf, and F. Deleflie, "Simulation of long-term rotational dynamics of large space debris: A TOPEX/Poseidon case study," *Advances in Space Research*, vol. 65, no. 4, pp. 1182–1195, 2020.

[149] Institut de Mécanique Céleste et de Calcul des Éphémérides., "Miriade - the virtual observatory solar system object ephemeris generator." Website: `http://vo.imcce.fr/webservices/miriade/`, 2018.

[150] ESA, *DRAMA Final Report - Upgrade of ESA's Space Debris Mitigation Analysis Tool Suite*, 2014.

[151] HTG, *DRAMA Final Report - Upgrade of DRAMA's Spacecraft Entry Survival Analysis Codes*. HTG,ESA, Am Handweisergraben 13, 37120 Bovenden, Germany, 1.0.2 ed., 2019.

[152] NASA, "Debris assessment software." Website: `https://orbitaldebris.jsc.nasa.gov/mitigation/debris-assessment-software.html`, June 2010. Accessed: [March. 11,2020].

[153] ESA, "DRAMA software download." Website: `https://sdup.esoc.esa.int/drama/downloads`, 2020. Accessed: [April 21, 2020].

[154] NASA, "DAS software download." Website: `https://orbitaldebris.jsc.nasa.gov/mitigation/debris-assessment-software.html`, 2020. Accessed: [March. 04, 2020].

[155] J. Yu, X.-q. Chen, and L.-h. Chen, "Optimal planning of LEO active debris removal based on hybrid optimal control theory," *Advances in Space Research*, vol. 55, no. 11, pp. 2628–2640, 2015.

[156] V. Braun, A. Lüpken, S. Flegel, J. Gelhaus, M. Möckel, C. Kebschull, C. Wiedemann, and P. Vörsmann, "Active debris removal of multiple priority targets," *Advances in Space Research*, vol. 51, no. 9, pp. 1638–1648, 2013.

[157] D. Izzo, I. Getzner, D. Hennes, and L. F. Simões, "Evolving solutions to TSP variants for active space debris removal," in *Proceedings of the 2015 Annual Conference on Genetic and Evolutionary Computation*, pp. 1207–1214, ACM, 2015.

[158] M. Shan, J. Guo, and E. Gill, "Deployment dynamics of tethered-net for space debris removal," *Acta Astronautica*, vol. 132, pp. 293–302, 2017.

[159] J. L. Forshaw, G. S. Aglietti, N. Navarathinam, H. Kadhem, T. Salmon, A. Pisseloup, E. Joffre, T. Chabot, I. Retat, R. Axthelm, *et al.*, "RemoveDEBRIS: An in-orbit active debris removal demonstration mission," *Acta Astronautica*, vol. 127, pp. 448–463, 2016.

[160] A. E. Petropoulos, "Simple control laws for low-thrust orbit transfers," in *AIAA/AAS Astrodynamics Specialist Conference and Exhibit*, 2003.

[161] J. Pollard, "Evaluation of low-thrust orbital maneuvers," in *34th AIAA/ASME/SAE/ASEE Joint Propulsion Conference and Exhibit*, p. 3486, 1998.

[162] M. J. Turner, "Rocket and spacecraft propulsion: principles, practice and new developments". Springer Science & Business Media, 2008.

[163] K. Tsiolkovsky and W. Moore, "Academy, rm: Tsiolkovsky rocket equation," *Energy*, pp. 1–8, 1903.

[164] F. Covello, "Application of electrical propulsion for an active debris removal system: a system engineering approach," *Advances in Space Research*, vol. 50, no. 7, pp. 918–931, 2012.

[165] L. Singh, S. Bortolami, and L. Page, "Optimal guidance and thruster control in orbital approach and rendezvous for docking using model predictive control," in *AIAA Guidance, Navigation, and Control Conference*, p. 7754, 2010.

[166] J. E. Graf, R. W. Zurek, H. J. Eisen, B. Jai, M. Johnston, and R. Depaula, "The Mars reconnaissance orbiter mission," *Acta Astronautica*, vol. 57, no. 2-8, pp. 566–578, 2005.

[167] ESA, "ESA space debris mitigation compliance verification guidelines," tech. rep., ESSB-HBU-002-Issue1, from Inter-Agency Space Debris Coordination Committee, 2015.

[168] B. Fritsche, H. Klinkrad, A. Kashkovsky, and E. Grinberg, "Spacecraft disintegration during uncontrolled atmospheric re-entry," *Acta Astronautica*, vol. 47, no. 2-9, pp. 513–522, 2000.

[169] G. Palmer and D. Mitchell, "Analysis and simulation of a high accuracy spacecraft separation system.," *Journal of Spacecraft and Rockets*, vol. 3, no. 4, pp. 458–463, 1966.

[170] NASA, "Flight separation mechanisms - space vehicle design criteria," tech. rep., NASA STI, 1970.

[171] S. Sommer, V. Karamanavis, F. Schlichthaber, T. Patzelt, J. Rosebrock, D. Cerutti-Maori, and L. Leushacke, "Analysis of the attitude motion and cross-sectional area of Tiangong-1 during its uncontrolled re-entry," in *Proceedings of the 1st NEO and Debris Detection Conference*, ESA Space Safety Programme Office Darmstadt, Germany, 2019.

[172] H.-Y. Lin, T.-L. Zhu, Z.-P. Liang, C.-Y. Zhao, D. Wei, W. Zhang, X.-W. Han, H.-F. Zhang, Z.-B. Wei, Y.-Q. Li, *et al.*, "Tiangong-1's accelerated self-spin before reentry," *Earth, Planets and Space*, vol. 71, no. 1, pp. 1–9, 2019.

[173] J. Diebel, "Representing attitude: Euler angles, unit quaternions, and rotation vectors," *Matrix*, vol. 58, no. 15-16, pp. 1–35, 2006.